THE NATURE AND DYNAMICS OF RAPID SPRING ONSET IN THE ARCTIC

A Dissertation
Presented to
The Academic Faculty

by

Jia He

In Partial Fulfillment
of the Requirements for the Degree
Doctor of Philosophy in the
School of Earth and Atmospheric Sciences

Georgia Institute of Technology
May 2017

THE NATURE AND DYANMICS OF RAPID SPRING ONSET IN THE ARCTIC

Approved by:

Dr. Robert X. Black, Advisor
School of Earth and Atmospheric Sciences
Georgia Institute of Technology

Dr. Emanuele Di Lorenzo
School of Earth and Atmospheric Sciences
Georgia Institute of Technology

Dr. Yi Deng
School of Earth and Atmospheric Sciences
Georgia Institute of Technology

Dr. Walter A. Robinson
Department of Marine, Earth, and Atmospheric Sciences
North Carolina State University

Dr. James Belanger
School of Earth and Atmospheric Sciences
Georgia Institute of Technology

Date Approved: August 8th, 2016

To my family

ACKNOWLEDGEMENTS

This research work couldn't have been possible without the support of many people. First of all, I would like to express my deep gratitude to my advisor, Dr. Robert Black, for his continuous support. He gives me every freedom in pursuing the research goal from my own interested path. Whenever I run into difficulties, he is always there providing insightful suggestions. I wouldn't have enjoyed my doctoral research so much without his encouragement and guidance.

I would also like to thank Dr. Yi Deng and Dr. Walter Robinson for their constructive comments and suggestions on the research topic throughout my Ph.D. study. I would also like to recognize the efforts of Dr. James Belanger and Dr. Emanuele Di Lorenzo for their valuable input to my dissertation.

I would like to acknowledge my officemates for their suggestions on my research and their accompanying my graduate life. Rebecca Westby and Bradley Hegyi gave me helpful suggestions in preparing for the comprehensive exam. Yi Lu provided me with plenty resources and hands-on help for the model experiments. They all have helped me integrate into a fun life in a completely different culture.

Finally, I would like to thank my family and friends for their unconditional love and support. I would like to express my particular gratitude to my parents for their understanding and support of me pursuing my education and career in a far-away country. I would also like to thank my husband, Lu, for accompanying me through every difficulty in study and life.

TABLE OF CONTENTS

LIST OF TABLES

LIST OF FIGURES

LIST OF SYMBOLS AND ABBREVIATIONS

AD	adiabatic heating
AL	Alaska
AO	Arctic Oscillation
ASO	Arctic Spring Onset
CASE2000	CR event in 2000
CR	critical region over North Siberia
DA	Arctic Dipole Anomaly
dT	time derivative of temperature
d2T	second order time derivative of temperature
EA	East Asia
G-NA	Greenland-North America
hEHF	eddy heat flux convergence
hEHF_c	climatological eddy heat flux convergence
hgt500	geopotential height at 500 hPa
HL1	horizontal linear advection of anomalous air temperature by the climatological circulation
HL2	horizontal linear advection of climatological-mean temperature by wind anomaly
LTT	local tendency of temperature anomaly
LTT_c	local tendency of climatological temperature
NAO	North Atlantic Oscillation
RMS	root mean square
RoC	radius of curvature
SFW	stratospheric final warming

SLP	sea level pressure
T2m	2-meter air temperature
vEHF	vertical eddy heat transport
vEHF	climatological effects of vertical eddy heat transport
VL1	vertical heat transport of anomalous temperature by climatological vertical motion
VL2	vertical heat transport of climatological temperature by anomalous vertical motion
WRF	Weather Research and Forecasting model

SUMMARY

The Arctic atmospheric circulation undergoes a systematic rapid seasonal transition each year from late winter to early spring. At stratospheric and upper-tropospheric levels, this transition is dominated by an abrupt break down of the circumpolar vortex, which is related to upward planetary wave propagation. At the surface, this rapid spring onset transition is manifested by a dramatic increase in air temperature within a short time period. Very limited prior research efforts exist on the nature and physics of the rapid near-surface warming during Arctic spring onset (ASO). The current dissertation provides a thorough investigation of the abrupt transition of ASO events from the perspective of near-surface air temperature increase.

In contrast to conventional measures of spring onset timing (often defined in terms of temperature thresholds related to regional phenology), our investigation views the abrupt transition as either an acceleration of air temperature increase or a transition from a steady winter state into a warming spring state. Thus, the first part of this dissertation provides a comprehensive exploration of three novel techniques for identifying ASO via the rapid increase in the 2-meter temperature (T2m). A 2-phase linear regression model is first employed to identify a transition from an approximately steady winter state to a warming spring state. The other two methods, the time derivative (d2T/dT) and radius of curvature (RoC) techniques, isolate periods of large T2m *acceleration*. Although all three approaches are largely successful in isolating the state transition associated with ASO, the RoC method is most effective in capturing the most rapid temperature increases and is this adopted in the remainder of the dissertation. It is determined that ASO timing exhibits strong interannual variability but with no significant long-term trend. The Arctic-mean

composite evolution reveals T2m increases notably faster than the climatological seasonal trends, which indicates the likelihood of a dynamical driving mechanism.

Spatial patterns of T2m changes occurring during ASO events are shown via a composite analysis. The rapid warming observed over Polar latitudes during ASO is roughly zonally symmetric while concomitant warming patterns observed further south distinguish North Siberia as the critical region (CR) in which robust warming occurs during most ASO events. Besides such common structures isolated in the composite, individual events demonstrate distinct primary warming structures that may occur outside the CR region. A hierarchical cluster analysis and a synoptic classification technique are applied to the individual ASO T2m change maps leading to the identification of four subsets of events distinguished by their primary regional warming signature. The synoptic behavior of ASO events is studied via a parallel composite analysis of sea level pressure (SLP) anomalies. This analysis reveals that, during ASO events, changes in the regional semi-permanent surface pressure features provide favorable conditions that promote regional temperature advection and ASO warming. Thus, our synoptic analyses also suggest that ASO events are dynamically driven by large-scale atmospheric processes.

To provide a more quantitative understanding of the physical sources for the rapid temperature increases observed during Arctic spring onset, we divide the temperature tendency in the thermodynamic equation into separate terms related to different physical processes: horizontal linear advection, nonlinear eddy heat flux convergence, heat transport via vertical motions, adiabatic heating and cooling, and diabatic effects. After evaluating the contributions of each term to the temperature tendency, we find that nonlinear heat transport is essential for initiating the rapid temperature increase prior to and during the

early stage of events while linear temperature advection is the leading factor in maintaining rapid warming during the later stages. This notion is further supported by the observed accumulation of eddy heat transport into the primary warming region during the early ASO stages and the formation of a coherent large-scale circulation pattern favorable for warm advection during middle and late ASO stages.

Finally, a case study is performed for the CR event in 2000 (CASE2000) using both observational data and numerical model simulation outputs. During CASE2000, robust T2m increases resembling the composite structure occur over the CR region. A heat budget analysis of CASE2000 identifies nonlinear processes as the primary contributor to the early stages of onset and linear advection as a leading source later on. Model experiments using the Weather Research and Forecasting Model (WRF) are performed for CASE2000 to directly access the role of nonlinear processes due to synoptic eddies. A control experiment is first conducted to simulate CASE2000. Then, two parallel sets of model experiments are performed to simulate conditions in which synoptic eddy activity is suppressed by using a) meteorological variables filtered using a 10-day running mean and b) composite meteorological variables as input for initial and boundary conditions. The timing of CASE2000 is effectively delayed by suppressing synoptic eddy activity at the lateral boundary that also leads to a large reduction on magnitude of T2m increase. The case study provides a ancillary support to the composite phenomenological and mechanistic analysis of ASO events.

CHAPTER 1: INTRODUCTION

1.1 Arctic Climate System

The Arctic represents the northernmost portion of the Earth. The Arctic Circle (66.5°N) is usually taken as the southern boundary as it demarcates the region of continuous daylight/darkness. The latitude of 70°N is another common latitude assigned as a southern boundary since north of 70°N is mostly covered by ocean.

As concluded by Serreze and Barry (2014), the Arctic is a complex system with strong physical coupling among air, seas, and continents. The Arctic system consists of various surface conditions, including open water and sea-ice over the Arctic Ocean, along with mountains, lakes, permafrost regions, and high-latitude tundra over land surface. The Arctic exhibits a robust response to the changing climate, which in turn casts important impacts on the global climate system and human activity.

1.1.1 Energy Budget over the Arctic

The Arctic serves as a heat sink for the global climate system. As shown in many studies of the radiative budget at the top of the atmosphere, the high-latitude regions exhibit net radiative cooling while the low latitude regions exhibit net radiative warming (Fig. 1 in Trenberth and Caron 2001). This imbalance in solar radiation results in an uneven distribution of air temperature and atmospheric pressure, leading to a poleward energy transportation by the atmospheric and oceanic circulations (Fig. 7 in Trenberth and Caron 2001). At higher-latitudes, the meridional transport is primarily due to the atmospheric circulation.

In analyzing the energy budget of an atmospheric column, changes in the heat storage can be divided into three components: the net radiative forcing at the top of

atmosphere, heat flux from the Earth surface, and the convergence of horizontal heat flux in to the column.

During the seasonal transition from late winter to early spring (February-March-April), the Arctic atmosphere undergoes a continuous gain in heat storage. However, the net radiative forcing at the top of the atmosphere remains negative during spring. A large amount of positive heating from the horizontal convergence of meridional heat transport and surface heat flux compensates for the net radiative cooling, and thus leading to the net increase of heat storage. Among the two warming sources, horizontal heat convergence is a dominant contributor with a magnitude at least twice that of surface heating. At high-latitudes, the meridional heat transport is dominated by synoptic eddies associated with weather systems and low frequency disturbances (Table 3.1 in Serreze and Barry 2014).

1.1.2 Atmospheric Systems over the Arctic

Atmospheric systems at high-latitudes are characterized by different circulation patterns in the stratosphere and troposphere with notable seasonal variance.

The near surface circulation is determined by the thermal contrast between continents and oceans. During wintertime, the sea level pressure (SLP) field is dominated by large-scale semi-permanent pressure systems, namely, the Aleutian Low, Icelandic Low, and Siberian High (Fig. 1.1a). Such zonal asymmetry diminishes gradually with respect to altitude (Figs. 1.1a-1.1d). A persistent circumpolar cyclonic system, the polar vortex, extends from the mid-troposphere up through the stratosphere (Figs. 1.1b-1.1d), with the core westerlies located between 60°N-70°N at the stratospheric levels (Fig. 1.2a). The stratospheric polar vortex weakens during springtime and transitions into weak circumpolar easterlies during summer (Fig. 1.2b).

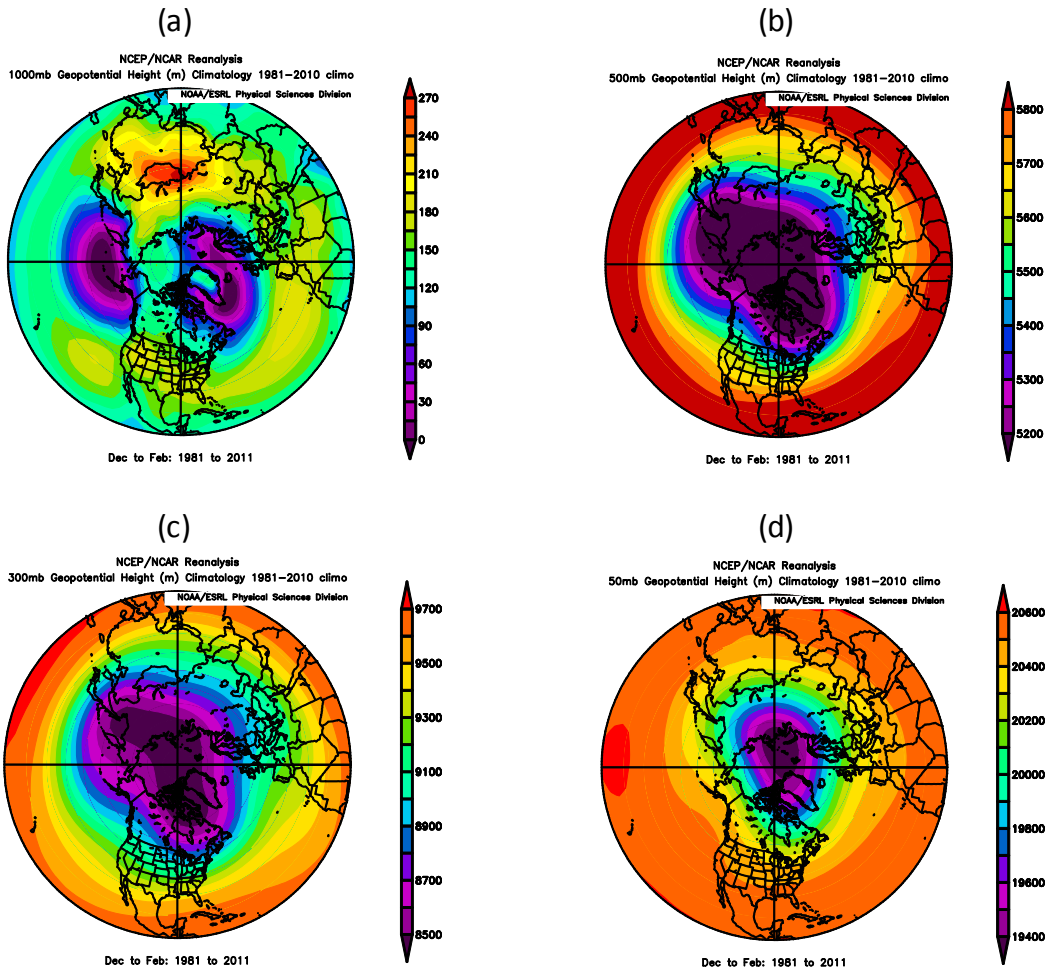

Figure 1.1: Winter mean climatology of geopotential heights at (a) 1000mb, (b) 500mb, (c) 300mb, and (d) 50mb. Created from the NOAA Earth System Research Lab plotting and analysis product.

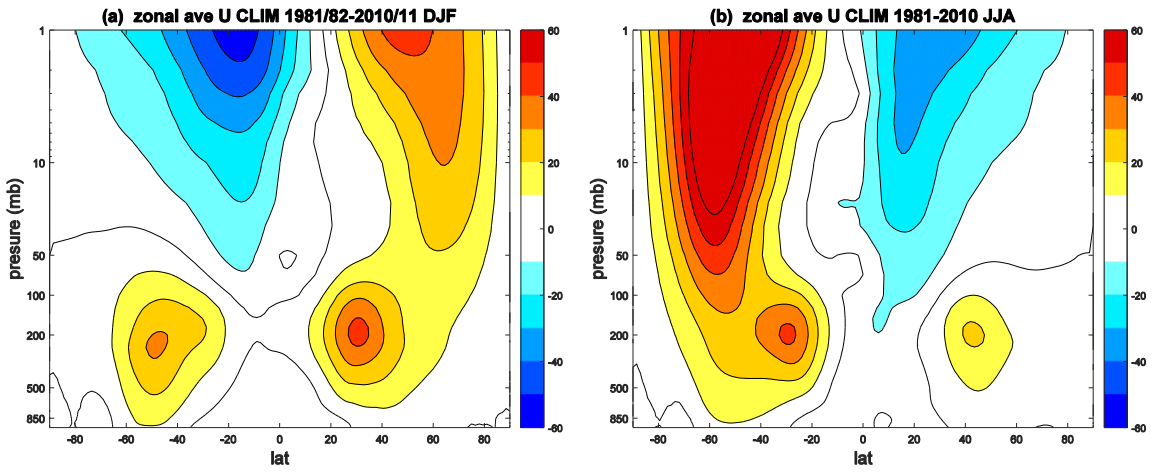

Figure 1.2: (a) Winter climatology and (b) summer climatology of zonal mean zonal wind. Created from the NOAA Earth System Research Lab plotting and analysis product.

The Arctic Oscillation (AO), which represents a see-saw SLP perturbation between high-latitude and mid-latitude regions, is the leading mode of Arctic atmospheric variability (Thompson and Wallace 1998). The North Atlantic Oscillation (NAO), a pressure see-saw between the Icelandic Low and Azores High, represents the North Atlantic reflection of AO (Wallace 2000). The AO/NAO has a broad impact on air temperature (e.g., Frey and Smith 2003; Overland et al. 2004; Rigor et al. 2002), precipitation (e.g., Frey and Smith 2003; Gong and Ho 2003; Gong et al. 2001), large-scale circulations (e.g., Ambaum et al. 2001; Baldwin and Dunkerton 1999; Corti et al. 1999), and sea ice concentration (e.g., Deser et al. 2000; Deser et al. 2010; Rigor et al. 2002). The

AO represents the surface manifestation of the northern annular mode (NAM), which serves to directly couple variability in the stratospheric and tropospheric circulations (Baldwin and Dunkerton 1999).

The Arctic Dipole Anomaly (DA), the second leading mode of local SLP anomaly over the Arctic, reflects a contrast in pressure anomalies between the eastern and western Arctic (Wu et al. 2006). The wind anomaly associated with the positive DA mode provides a favorable condition for sea-ice export through the Fram Strait from the central Arctic, and thus leading to low summer sea ice(Wang et al. 2009; Watanabe et al. 2006; Wu et al. 2006).

On average, polar high pressure dominates the Arctic surface system. Synoptic scale cyclones are generated frequently over the Arctic Ocean during winter. Another source of Arctic cyclone activity is the migration from mid-latitudes, particularly within the Atlantic sector. The Aleutian Low and Icelandic Low regions are active locations for cyclogenesis. The migration of extratropical cyclones into the Arctic provides a large resource for northward transport of heat and moisture.

1.1.3 Arctic in a Changing Climate

Possible long-term observed temperature increases associated with anthropogenic global warming is a scientific topic of great interest. Although air temperature trends demonstrate considerable spatial variability, the strongest warming occurs within the Arctic region in both the observations and model simulations (Serreze and Francis 2006). In addition to increases in air temperature, summertime sea-ice concentrations have decreased dramatically during the past 10 years, with several record-breaking low concentrations occurring recently (Deser and Teng 2008; Parkinson and Comiso 2013;

Screen and Simmonds 2010; Serreze et al. 2003; Serreze et al. 2007; Stroeve et al. 2007; Zhang et al. 2013). The atmospheric circulation over the Arctic has also experienced a radical shift with the action centers of the NAO migrating northeastward, also in relation to the recent changes in Arctic climate system (Zhang et al. 2008).

1.2 Arctic Springtime Seasonal Transition

1.2.1 Phenological Spring Onset

Research within various scientific disciplines shares a common interest in the study of high-latitude spring onset due to its impact on ecosystem productivity (Linderholm 2006). From a phenological perspective, spring onset, or the onset of the growing season, is identified in terms of local phenomena such as flower blossoming (Asaa et al. 2004; D'Odorico et al. 2002) or bug burst (D'Odorico et al. 2002), which are connected to air temperature (Schwartsz and Crawford, 2001). Sparks and Menzel (2002) synthesized data from a wide range of species over a large spatial domain and found that spring onsets defined in terms of phenological events (including ground flora, bird migration, tree flowering, and harvest timing) all demonstrate consistent responses to the warming climate. From a biological viewpoint, previous studies have ascertained an advancing trend in the spring onset timing (e.g., Schwartz et al. 2006; Sparks and Menzel 2002). Corresponding studies based upon the atmospheric observational record also indicate a long-term warming trend in Arctic air temperature during spring (Rigor et al. 2000). As discussed in a number of studies (e.g., Schwartz and Crawford 2001; White et al. 1997), phenological spring onset events result from the preceding cumulative effects of heating, so that an advancing trend is generally attributed to global warming.

Analyzing data from several stations over Western Europe, D'Odorico et al. (2002) attribute the temperature-induced interannual variation of spring onset to the North Atlantic Oscillation (NAO) and concluded that a warmer winter resulting from the positive NAO phase usually leads to an earlier spring onset. Asaa et al. (2004) illustrated a similar relationship for Central and Eastern Europe; they also related spring onset to different atmospheric circulations patterns. Wiltshire and Manly (2004) and Wiltshire et al. (2008) analyzed spring onset in terms of phytoplankton bloom but ascertained no significant trend with a comparable interannual variability. A recent study by Lohmann and Wiltshire (2012) linked the early and late spring onsets with the two major types of large-scale atmospheric regimes over the high-latitudes of the Atlantic-European sector. Their study reinforces the notion that the robust interannual variability of spring onset timing is consistent with a key role for atmospheric dynamical processes in determining the seasonal transition time in individual years.

1.2.2 Atmospheric Transition during Arctic Spring Onset

As introduced previously, the Arctic stratosphere is dominated by a deep circumpolar vortex during the wintertime. The associated wintertime westerlies (Fig. 1.2 a) are replaced by much weaker circumpolar easterlies during summer (Fig. 1.2 b). This transition happens at the onset of spring when a rapid breakdown of the polar vortex occurs along with a concomitant increase in stratospheric polar air temperature during stratospheric final warming (SFW) events (Andrews et al. 1987; Black et al. 2006; Waugh and Rong 2002). Black et al. (2006) showed that the breakdown of polar vortex is a rather abrupt shift of the stratospheric wind direction accompanying a coherent decrease in the upper tropospheric westerly wind. The near-surface response is dominated by an AO-

/NAO-like pattern shift from positive to negative phase, with SLP rising at polar latitudes. Follow-up diagnostic research revealed that SFW events are primarily driven by planetary-scale Rossby waves propagating upward from the troposphere (Black and McDaniel 2007). These studies raised the interesting possibility of a role for the high latitude stratosphere in enacting the tropospheric circulation changes taking place during spring onset. Further, the studies suggested that dynamical processes likely play a critical role in driving Arctic spring onset within the middle atmosphere.

At the surface, the Arctic surface air temperature increases dramatically within a short time period during early spring. By analyzing the Arctic 2-meter temperature (T2m), Martin and Munoz (1997) found a dramatic decrease in the daily root-mean-square (RMS) of T2m during spring, revealing a transition from high winter time variability to relatively weak spring time variability. This high frequency behavior is shown in Figs. 1.3a and 1.3b, which display the same analysis calculated from ERA-interim reanalysis data. Although the high frequency variability decreases during spring, the total air temperature field increases quite rapidly as illustrated in the companion Hovmöller plot in Fig. 1.3c. The rate of T2m increase during spring is much faster than the rate of decrease during fall. In addition, the rapid warming behavior is particularly pronounced in the Arctic, north of 75°N, with less rapid warming observed to the south.

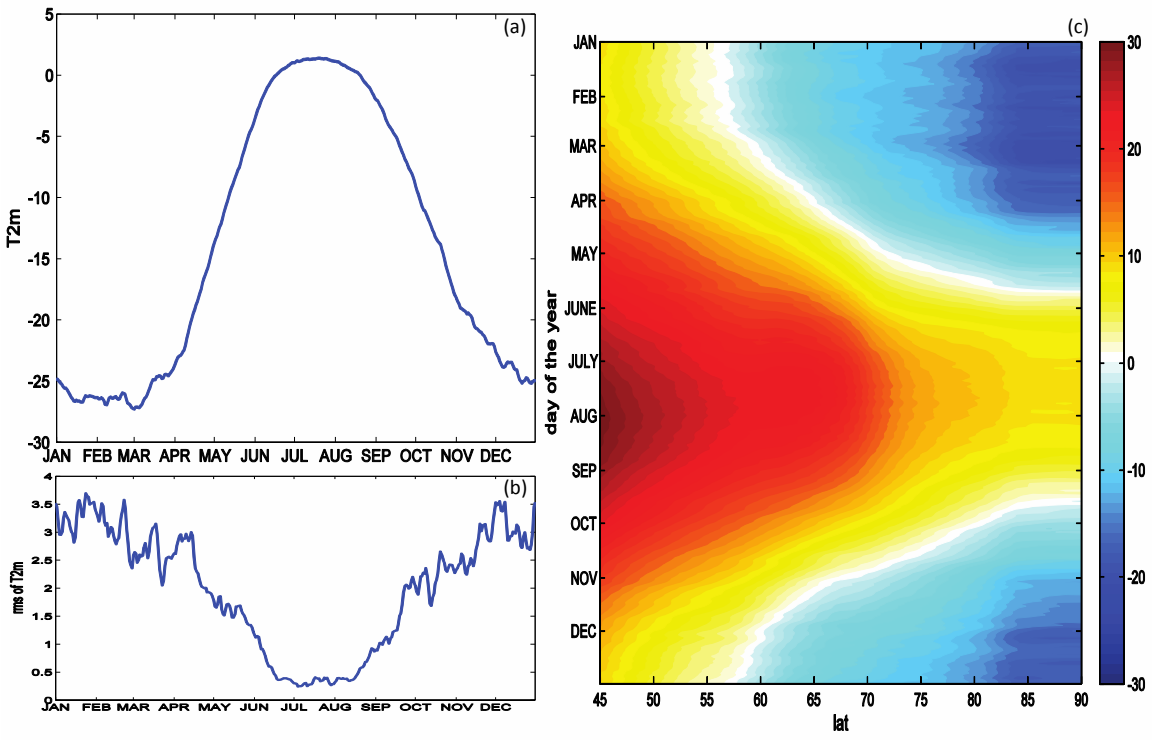

Figure 1.3: (a) Daily average T2m (°C) over the polar cap (north of 75°N) from 1979 to 2010. (b) Daily RMS of Arctic T2m (°C). (c) Hovmöller plot of zonal-mean T2m (°C): latitude vs daily of the year.

1.3 Research Objectives

Although Martin and Munoz (1997) recognized a rapid increase in surface temperature associated with a decrease in its variability, our current understanding of this analogous rapid transition at the surface is still quite limited. Therefore, this work is aimed at providing a thorough investigation of the abrupt Arctic spring onset from the perspective of the rapid increase in surface air temperature. The goals of this current research and the structure of this dissertation are listed below:

- Chapter 2 provides a detailed discussion of the identification of Arctic spring onset events. In contrast to the conventional methods using temperature thresholds, three methods (including the time derivative method, the radius of curvature method, and the 2-phase linear regression model) that define the events in terms of "rapidity" are introduced. The long-term trend and interannual variability of the annual event timing are also investigated to illustrate the potential impact of climate change on the Arctic spring onset events.
- Chapter 3 investigates the spatial structure of air temperature increase during Arctic spring onset events. A hierarchical cluster technique and a synoptic classification method are applied to the changes in air temperature during ASO events to categorize events based on the spatial patterns. SLP time evolution during the events are also analyzed to reveal potential dynamical contributors to ASO events.

- Chapter 4 employs a regional heat budget analysis based on the isobaric thermodynamic equation. Regional ASO events are first identified via the application of the radius of curvature method to the regional-mean air temperature. Then the temperature tendency is divided into multiple terms related to different physical processes, including linear advection, nonlinear heat fllux convergence, vertical transport, adiabatic heating/cooling, and diabatic effects. Contributions from each term are analyzed to isolate the primary driving mechanisms of the rapid temperature increase.
- The CR event in 2000 (CASE2000) is selected to perform a detailed case study. Analysis with observational data shows that CASE2000 exhibits the basic characteristics of the composite results. Numerical model simulations with the Weather Research and Forecasting Model isolate the influential role of synoptic eddy activity on ASO events. Model results indicate that the nonlinear processes associated with synoptic eddy activity is a vital factor in determining the timing and magnitude ASO events.
- Chapter 6 provides a summary and implications for the investigation of Arctic spring onset events.

CHAPTER 2: IDENTIFICAION OF ARCTIC SPRING ONSET EVENTS

2.1 Introduction

Research within various scientific disciplines share a common interest in the study of high-latitude spring onset due to its impact on ecosystem productivity (Linderholm 2006). From a phenological perspective, spring onset, or the onset of the growing season, is identified in terms of local phenomena such as flowering (Asaa et al. 2004; D'Odorico et al. 2002) or bug burst (D'Odorico et al. 2002). The phenological onset of the growing season exhibits strong temporal and spatial variability (D'Odorico et al. 2002), which is believed to be related to the cumulative effect of preceding local variations in temperature (White et al. 1997; Schwartz and Crawford 2001). Sparks and Menzel (2002) synthesized data from a wide range of species over a large spatial domain and found that spring onset defined in terms of phenological events (including ground flora, bird migration, tree flowering, and harvest timing) all demonstrate consistent responses to the warming climate. Analyzing data from several stations over Western Europe, D'Odorico et al. (2002) attribute the temperature-induced interannual variation of spring onset to NAO and concluded that a warmer winter resulting from the positive NAO phase usually leads to an earlier spring onset. Asaa et al. (2004) illustrated a similar relationship for Central and Eastern Europe; they also related spring onset to different atmospheric circulations patterns. These studies established a robust relationship between phenological spring onset and the large-scale atmospheric circulation.

In addition to influences upon phenology, systematic rapid transitions are also observed to occur in the atmospheric circulation itself. During spring, the Arctic

atmosphere undergoes a complicated transition from a statistically steady winter state toward a rapidly evolving warming state that is forced by a combination of increasing solar insolation and internal atmospheric dynamics. During early spring, the Arctic surface air temperature increases dramatically within a short time period. Martin and Munoz (1997) analyzed the Arctic 2-meter temperature (T2m) using a polar region-based gridded dataset from the NASA Earth Observing System Project Polar Exchange at the Sea Surface (POLES). The daily root-mean-square (RMS) of T2m decreases dramatically during spring, revealing a transition from high winter time variability to relatively weak spring time variability. This high frequency behavior is shown in Figs. 1.3a and 1.3b, which display the same analysis calculated from ERA-interim reanalysis data. Although the high frequency intra-seasonal variability decreases during spring, the total air temperature field increases quite rapidly as illustrated in the companion Hovmöller plot in Fig. 1.3c. The rate of T2m increase during spring is much faster than the rate of decrease during fall. In addition, the rapid warming behavior is particularly pronounced in the Arctic, north of 75ºN, with less rapid warming observed to the south.

Studies of the upper level atmosphere also show an abrupt transition of spring onset. Black et al. (2006) examined stratospheric final warming events and discovered that, during the annual spring demise of the westerly stratospheric polar vortex, the zonal-mean zonal wind decreases rapidly over a vertical domain extending from the mid-stratosphere downward through the entire troposphere. The near-surface response is dominated by an NAO-like pattern shift from positive to negative phase, with sea level pressure (SLP) rises at polar latitudes. Follow-up diagnostic research revealed that stratospheric final warming events are primarily driven by planetary-scale Rossby waves propagating upward from the

troposphere (Black and McDaniel 2007). These studies raised the interesting possibility of a role for the high latitude stratosphere in enacting the tropospheric circulation changes taking place during spring onset. Further, the studies suggested that dynamical processes likely play a critical role in driving Arctic spring onset within the middle atmosphere. However, our current understanding of the analogous ASO transition at the surface is limited, at best. Although Martin and Munoz (1997) recognized a rapid increase in surface temperature associated with a decrease in its variability, no previous research efforts have examined the fundamental structures of this rapid seasonal transition. Therefore, this chapter is aimed at introducing a metric to isolate the rapid transition of atmospheric Arctic spring onset. The primary associated circulation structures and the underlying dynamical processes will be investigated in the following chapters.

Atmospheric science encompasses the internal dynamics of the atmospheric circulation along with interactions among atmospheric systems on various temporal and spatial scales. Spring onset is usually defined as the time when T2m either exceeds a threshold value (Qian et al. 2009; Qian et al. 2011a; Qian et al. 2011b) or undergoes a period of phase change in the seasonal cycle (Thomson 1995). These two approaches provide differing results regarding the long-term trends of spring onset because the underlying physics are different. On the one hand, Qian et al. (2009) applied a temperature threshold approach, which is more closely related to phenological spring onset due to the prominent link between phenological events and absolute surface air temperature, and found evidence for an advancing trend in spring onset linked to global warming and consistent with parallel phenological analyses. They further attributed spring onset variability to annual cycle variations and long-term warming trends (Qian et al. 2011a) and

demonstrated an interannual relationship between the time-varying annual cycle and El Niño events (Qian et al. 2011b). On the other hand, Thomson (1995) fitted the seasonal cycle to a pre-determined sinusoidal wave function, estimating the phase state from a complex demodulation approach, and found that the phase trend during the last century is consistent with the increasing CO2. However, using the same fitting approach but estimating the phase states via four different methods, Paluš et al. (2005) argued that more evidence is required to link the long-term trend in spring onset to an anthropogenic influence. Synoptic processes such as cyclones and anti-cyclones are important contributors to sudden temperature increases in high-latitudes during spring but it is very difficult to link them directly to phenological events, as pointed out by Asaa et al. (2004). The sinusoidal fitting method, which considers the physical and mathematical features of the time series alone, does not resolve dynamic processes. Therefore, neither approach discussed above is effective in identifying the coherent and rapid large-scale atmospheric transitions from winter to spring, more specifically the rapid changes in surface air temperature and large-scale circulation. Building on the existing research discussed above, the main goals of this chapter are to (a) develop a systematic and robust method to delineate rapid Arctic spring onset in the high latitude atmosphere and (b) characterize fundamental statistics of the spring onset timing. In pursuing (a) we introduce new approaches that effectively capture episodes of Arctic spring onset linked to rapid increases in surface air temperature.

2.2 Data and General Approach

Study in this chapter is based on the interim reanalysis data from ECMWF (ERAI) (Dee et al. 2011) for 32 years (1979-2010). In order to test the sensitivity of our results to

the dataset employed, we also identify ASO based on the NASA Modern Era Reanalysis for Environmental Research and Applications data (MERRA) (Rienecker et al. 2011). Unless otherwise mentioned, the results presented in this chapter are based upon the ERAI data. The daily average T2m is the fundamental field variable used to define ASO. February 29 of all leap years is first removed from the data. Before analyzing the annual temporal behavior, we construct areal averages over the polar cap north of 75ºN.

To isolate a rapid warming signal in daily areal-average T2m for each calendar year, we tested three algorithms: A time derivative method, a radius of curvature method, and a 2-phase linear regression. In the first two methods, a 30-day low pass filter is first applied to the areal average daily T2m to remove high frequency variability while the third method uses unfiltered data. Taking an areal average also reduces high frequency variability, thus helping to overcome the inherent deficiencies of applying 31-day running-mean averages to temporally smooth time series (as noticed by Qian et al. 2011a). Further details regarding the three methods are provided in Section 2.3.

2.3 Defining Arctic Spring Onset

This section describes and compares different algorithms for identifying rapid warming during ASO. We define an ASO index as the time when a rapid increase in T2m occurs over the Arctic. In order to identify abrupt transition points in each annual cycle of T2m, we explored three methods: The 2-phase linear regression model (Lund and Reeves 2002) (a statistical view point), the time derivative (a calculus view point), and the radius of curvature (a geometric view point).

The idea behind the second and third two methods is similar: They identify times marked by an abrupt increase in the rate of change of T2m (which can occur after periods of relatively weak T2m increases or even T2m decreases).

2.3.1 The 2-Phase Linear Regression

The 2-phase linear regression model is most commonly used in identifying change-points in climate time series (Lund and Reeves 2002). Cook and Buckley (2009) used this method to identify the monsoon season onset, which provides us with a novel perspective for viewing the abrupt ASO transition.

The 2-phase linear regression approaches the topic of rapid temperature increase by considering the general difference between springtime and wintertime temperature trends. T2m typically increases dramatically during springtime while it remains relatively stable with little increase or decrease during much of the winter. Its variability can be viewed as a high frequency signal embedded upon a steady mean state in winter and a gradually increasing state in spring. The transition between the two linear states is therefore taken as the ASO in this approach.

In order to obtain realistic longer-term background states for winter and spring, during each year we retain the unfiltered daily T2m for a relatively long period that begins in December of the year before and continues through June. This period is chosen for the 2-phase linear fitting procedure. The identification of change points, however, is restricted from late winter to mid-spring, that is Day 55 to 120 of each calendar year. In Figs. 1.3a and 1.3b, the long-term daily average T2m over the Arctic starts to increase while its variability starts to decrease at the end of February. The annual cycle exhibits less fluctuation after late April. Thus we restrict the search to the period from late February to

the end of April, Day 55 to Day 120. The results are relatively insensitive to changes in either the starting time or the ending time.

For each day falling within the identification period, the following algorithm is applied to generate the 2-phase linear model:

a) That specific day is selected as representing the separation between winter and spring periods.

b) A least square method is separately applied to the two periods: The steady winter period is taken from Dec 1st to the separation day and the gradually-warming spring period from the separation day to June 30th. A least square technique is applied to obtain the linear fits of the two periods, which are then taken to approximately represent the background winter and spring states, respectively.

c) The error associated with this representation is determined by calculating the cumulative sum of the daily root mean square difference between the linear regressions and the observed T2m series.

Procedure (a) through (c) is then repeated for each day throughout the identification period. The date when the error estimate reaches its minimum is taken as the most suitable separation between winter and spring, or ASO. The two corresponding linear regression fits represent the winter and spring background states of that year.

2.3.2 The Time Derivative

From a calculus view point, the "acceleration of T2m" is taken as the second derivative of T2m with respect to time (d2T hereafter). Thus, for each year the most rapid warming is taken to be the time when the maximum d2T occurs during a period

encompassing late winter through mid-spring, or the identification periods used in the 2-phase linear regression model.

Whether it is an abrupt transition not only depends on d2T alone but also by the concomitant rate of T2m change (first derivative of T2m with respect to time) at that time. Consider two cases: (1) T2m rate of change increases from 1 ºC/day to 1.2 ºC/day; (2) T2m rate of change increases from 0.01 ºC/day to 0.21 ºC/day. Although the acceleration is 0.2 (ºC/day)/day in both cases, the second case is basically a transition from near zero T2m change to a dramatic increase. To account for such situations, d2T is further normalized by the first derivative (dT), and d2T/dT is used as a proxy to represent the warming. We take the time of maximum d2T/dT as the ASO measure.

2.3.3 The Radius of Curvature

From a geometric view point, each curved segment in the T2m annual cycle can be fitted to small circles using the concept of radius of curvature (RoC), which is calculated as

$$R = \frac{\left(1 + \left(\frac{dT}{dt}\right)^2\right)^{3/2}}{\frac{d^2T}{dt^2}}$$

The RoC is positive during periods of T2m acceleration (with respect to calendar day). Thus when the RoC reaches a minimum positive value, T2m will exhibit the strongest "increase in the T2m increase". We search for the minimum positive value of RoC during the same period as in the d2T/dT method.

2.3.4 Comparison among the three methods

The three methods introduced above is based upon 2 different viewpoints of spring onset. The 2-phase linear regression considers the ASO transition as a general difference between springtime and wintertime temperature trends, which employs a rather long period for assessment. The second and third methods discussed above consider "temporally-localized" information, which only employs T2m during a period of several days around the date of interest and identifies times of acceleration in T2m. Fig. 2.1a provides the ASO indices calculated from the three methods for each year in the period of study. The results from the three methods demonstrate considerable similarity. The d2T/dT and RoC methods provide almost identical ASO dates except during 1991 and 2009, which will be discussed below. The correlation coefficient between the two time series is 0.8133 ($p = 2.69 \times 10^{-8}$). Although the fundamental interpretation of ASO is different for the 2-phase linear regression model than in the other two methods, the results are nonetheless consistent with correlation coefficients of 0.7862 ($p = 1.97 \times 10^{-7}$) and 0.6011 ($p = 3.49 \times 10^{-4}$), for the RoC and d2T/dT time, respectively.

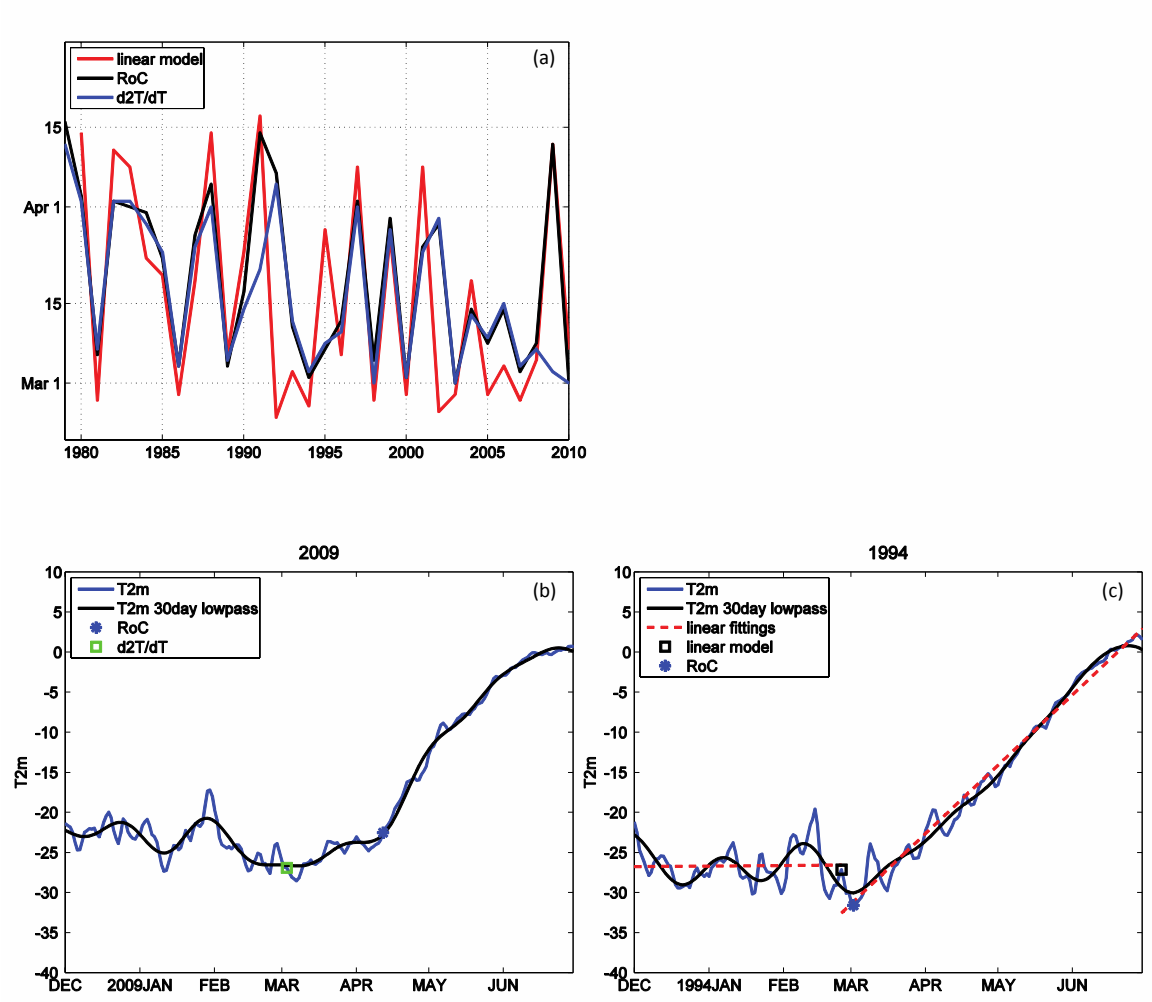

Figure 2.1: (a) ASO calculated from the two-phase linear model (red), time derivative (blue), and radius of curvature (black) methods. (b) ASO during 2009 is presented as an example of the comparison between d2T/dT and RoC methods. T2m (ºC) unfiltered (30-day low pass) data are shown with blue (black) solid line; and ASO via RoC (d2T/dT) is shown with a blue asterisk (green square). (c) ASO during 1994 is presented as an example of the comparison between RoC method and the linear regression model. T2m (ºC) unfiltered (30-day low pass) data are shown with blue (black) solid line; linear fittings of the winter and spring T2m states from the two-phase linear model are shown with read dashed line; and ASO via the RoC (linear regression model) is shown with a blue asterisk (black square).

Despite the reassuring consistency among the three methods, we need to select one as the primary index for our analysis of ASO. Noting the mathematical similarity between 1/[RoC] and d2T/dT, it is no surprise that the two methods provide very similar results. However, during the time of interest, T2m is almost always accelerating, thus d2T is rarely zero; but there is no guarantee of dT being non-zero, and a near zero dT will cause problems in calculating d2T/dT. As we find during individual years, it is common for the rapid acceleration to be embedded within a relatively small background dT. As shown in Fig. 2.1b, the two cases when d2T/dT and RoC give very different ASO indices (1991 and 2009 in Fig. 2.1a) are related to this problem (e.g., 2009 case in Fig. 2.1b): In 2009, d2T/dT identifies a time when dT is almost zero resulting in a large d2T/dT, while RoC identifies a time when d2T is truly large. Therefore, considering the inevitable near-zero dT events, from a practical perspective RoC is more generally applicable than d2T/dT as an optimal method to identify the T2m acceleration times.

We now contrast the RoC and 2-phase linear regression methods. Fig. 2.1c provides an example for 1994. The ASO identified with the RoC method (blue asterisk) coincides with the local minimum of both the unfiltered (blue solid line) and low-passed filtered (black solid line) T2m data, while the ASO identified with the 2-phase linear model (black square) occurs several days earlier during a period of decrease in both the unfiltered and low-passed T2m. Selecting among such differences depends on the scientific problem of interest. The 2-phase linear regression is clearly preferable for an investigation of the transition between wintertime and springtime background states, in which the temporally-localized T2m behavior matters less than the longer-term trends in T2m. However, since we are interested in identifying periods of relatively rapid T2m increase, the RoC method

provides a suitable approach for identifying the initiation of rapid warming periods. Therefore, we choose to adopt the RoC approach in defining ASO.

2.3.5 Data set sensitivity

Before analyzing the characteristics of ASO, the robustness of the RoC method is first tested by applying the same algorithm to a second reanalysis data set, MERRA. Figure 2.2a contrasts ASO dates derived by applying the RoC method to both ERAI and MERRA data sets. The overall similarity is quite remarkable. For 30 of the 32 events, the two methods provide dates that are within 5 days of one another. The only two exceptions are 2003 and 2005 that will be discussed further in Section 2.4.

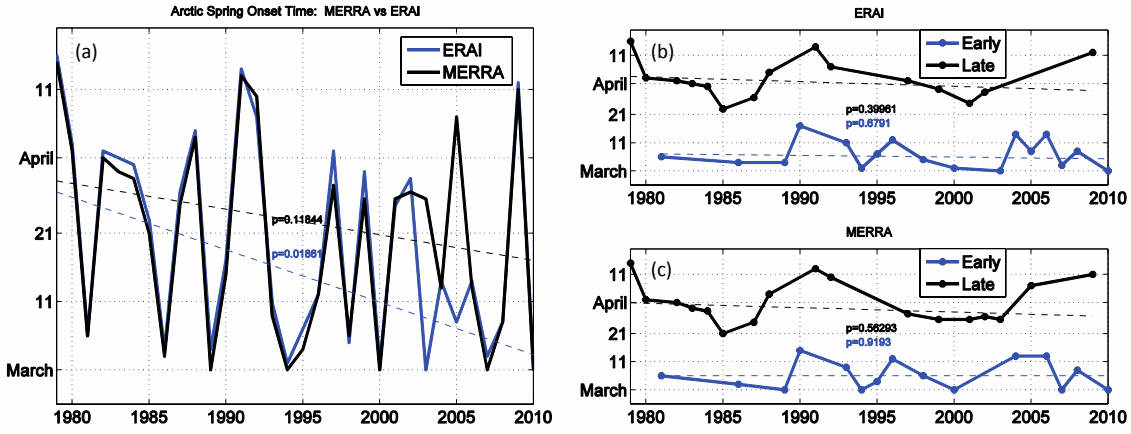

Figure 2.2: (a) ASO dates calculated using ERAI (blue) and MERRA (black), respectively. The trend lines of Sen's slope estimation are plotted in dashed lines of the corresponding color; *p* values are noted in the corresponding color. (b) Separate early (blue) and late (black) event dates from ERAI. Sen's trends are shown with a dashed line and *p* values are in the same color. (c) As in (b), but for MERRA.

2.4 Climatology and Trend of ASO events

The average ASO is day 78 of the calendar year, or March 19th, one day in advance of the vernal equinox. Among the 32 years from 1979 to 2010, the ASO dates exhibit substantial interannual variability, as shown by the black line in Fig. 2.1a. Onset occurs as early as March 1st and as late as April 16th. The events are not evenly distributed; instead, they appear to be separated into two groups: An "early" group having a mean onset date around March 2nd (day 61 of the calendar year) and a "late" group with a mean onset date near April 3rd (day 93 of the calendar year). This bi-modal distribution is reflected via the two concentrated peaks near March 6th and March 31st in the histogram (Fig. 2.3a). In addition, in applying the RoC approach to the climatological T2m annual cycle (the smoothed daily T2m climatology is isolated by (a) calculating the long-term climatological mean T2m for each calendar day and (b) subsequently applying the 30-day low pass filter to the resulting climatological cycle. In doing so, we are then able to apply the same methods of isolating rapid warming in the T2m climatological cycle) and isolating the first and second RoC minima, we identify two distinct T2m acceleration times in the annual cycle in Fig. 2.3b. The primary T2m acceleration feature is close to the average date of the late ASO events while the secondary T2m acceleration feature approximately corresponds to the average date of the early ASO events. This two-stage onset behavior is also evident in all the individual years considered.

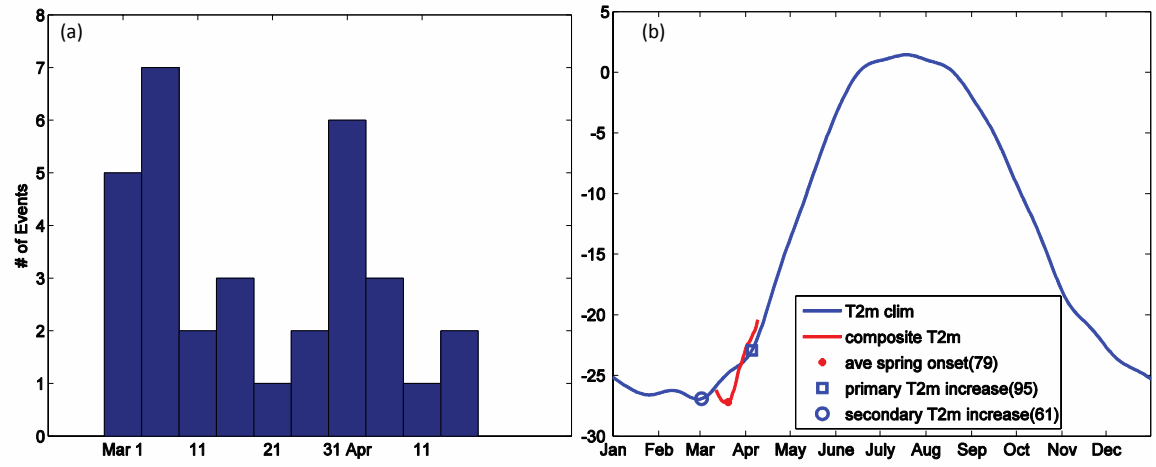

Figure 2.3: (a) Distribution of ASO dates. (b) Climatology annual cycle of daily Arctic T2m (ºC; blue line); primary (secondary) warming signature in the climatological annual cycle indicated by blue square (circle); for comparison, the composite T2m during the ASO is also displayed (red line); the average ASO is shown as a red dot. The most rapid increase of the climatological T2m is identified through RoC method. In contrast to the identification of rapud T2m increase for a specific year, the analysis of the climatological T2m retains both the minimum and the second minimum RoC signatures and denotes them as theh primary and secondary T2m warming signatures, respectively. The primary T2m signature is at Day 95 of the calendar year while the secondary is at Day 61.

There is considerable scientific interest in whether the timing of ASO exhibits a statistically significant trend associated with climate change. From a biological viewpoint, studies (e.g., Schwartz et al. 2006; Sparks and Menzel 2002) have ascertained an advancing trend in the ASO. Corresponding studies based upon the atmospheric observational record also indicate a long-term warming trend in Arctic air temperature during spring (e.g., Rigor et al. 2000). Consequently, studies defining ASO using a specific temperature threshold also demonstrate an advancing trend during the last century (Qian et al. 2009). As discussed in a number of papers (e.g., White et al. 1997; Schwartz and Crawford 2001), phenological spring onset events result from the preceding cumulative effects of heating, thus an advancing trend is generally attributed to global warming. However, ASO related to a rapid surface temperature increase represents an abrupt atmospheric seasonal transition, which is distinct from phenological spring onset (even though it may ultimately affect phenology). Thus, there is no a priori expectation that the two definitions will exhibit similar behavior in terms of long-term variability. In addition, due to the bi-modal nature of the onset date distribution, we must be very careful in assessing long-term trends in our analysis. The Mann-Kendall test and Sen's slope estimator are used to test for the existence of significant long-term trends (Helsel and Hirsch 1992) due to such non-Gausian distribution of ASO dates.

Figure 2.2a displays the ASO dates and Sen's trend line fits for both ERAI and MERRA data. Figures 2.2b and 2.2c, on the other hand, show onset dates and trend lines separately for the early and late events for both data sets. Trend values and corresponding p values are summarized in Table 2.1. In assessing the primary ASO dates (Fig. 2.3a) over the 32-year period, ERAI data exhibits an advancing trend ($p = 0.019$) while there is no

significant trend obtained from the MERRA data. This discrepancy is largely due to two years (2003 and 2005) in which early (late) events are identified in ERAI (MERRA). As shown in Figs. 2.3b and 2.3c and Table 1, when early and late events are assessed separately, no significant trends are identified from either data set. Therefore, the rapid ASO (as determined by the RoC method) does not exhibit recent long-term trends.

Table 2.1: The Sen's trend of ASO (unit: day/year) along with the corresponding *p* values. Trends and *p* values are calculated for a total 32 events from 1979 to 2010 as well as separate groups of early and late events from both ERAI and MERRA datasets.

	ERAI (32)	MERRA (32)	ERAI EARLY	ERAI LATE	MERRA EARLY	MERRA LATE
SEN'S TREND	-0.767	0.374	-0.061	-0.167	0.0	-0.158
P VALUE	0.019	0.118	0.679	0.400	0.919	0.563

The results of our trend analysis are not necessarily inconsistent with global warming behavior. As global mean temperature increases, the time when regional temperature exceeds a certain threshold will likely advance. However, as long as the local seasonal cycle in T2m does not change shape appreciably, increasing the mean temperature may shift the cycle upward but does not necessarily alter the typical time when the abrupt transition, or minimum RoC, occurs.

2.5 Summary and Discussion

In this chapter, we have discussed three methods for identifying Arctic spring onset (ASO) events in terms of surface air temperature evolution and have characterized the basic statistics of Arctic spring onset timing. To identify the rapid temperature transition serving as ASO, we applied methods from two perspectives. First, we consider ASO as a T2m transition from a wintertime steady state to a warming springtime state using a 2-phase linear regression model to isolate the two background states. Second, we consider the abrupt transition to be a T2m acceleration that is isolated in terms of the local radius of curvature (RoC). Although each approach has its pros and cons, the ASO dates obtained from the two different methods are highly correlated. Since our analyses concentrate upon surface temperature increase during ASO, we deem the RoC method to be most suitable and mainly employ this approach in our study.

Contrary to the general expectation of an advancing trend in spring onset associated with a warming background climate, we find strong interannual variability in spring onset but no evidence of significant long-term trends. Wiltshire and Manly (2004) and Wiltshire et al. (2008) analyzed spring onset in terms of phytoplankton bloom and also ascertained no significant trend with a comparable interannual variability. A recent study by Lohmann and Wiltshire (2012) linked the early and late spring onsets with the two major types of large-scale atmospheric regimes over the high-latitudes of Atlantic-European sector. This reinforces the notion that the robust interannual variability of spring onset timing suggests a key role for atmospheric dynamical processes in determining the seasonal transition time in individual years. Somewhat unexpectedly, the spring onset dates exhibit a bi-modal distribution (Fig. 2.3a). As is discussed in Section 2.4, the bi-modal distribution parallels

the 2-stage warming behavior that is inherent in the T2m climatological cycle, itself. A study of individual years reveals that this 2-stage process is very common. Our RoC algorithm differentiates between the two by selecting the stage with the greatest T2m acceleration. In a climatological sense, the later stage onset dominates; but during an individual year, it can be either of the 2 stages, depending upon the unique T2m evolution for that year. We note that the parallel results obtained from the 2-phase linear regression method provide a similar bi-modal representation of interannual spring onset behavior. A closer study of individual 2-stage events reveals that in years characterized by early (late) spring onset dates, the later (earlier) stage appears as a perturbation embedded in the springtime warming (steady wintertime) state. One interesting finding is that the average spring onset date, Mar 19th, is only one day away from vernal equinox, suggesting a prominent general role for the climatological annual solar cycle in determining the period of spring onset. The spatial structures of the temperature increase and associated synoptic evolutions are examined in Chapter 3.

CHAPTER 3: SYNOPTIC CHARACTERISTICS OF ARCTIC SPRING ONSET EVENTS

3.1 Introduction and General Method

The current study on the abrupt spring onset transition is motivated by the rapid increase in the zonally-averaged surface temperature over the polar region (Fig. 1.3c). Such "rapidity" is also observed in the areal-average 2-meter air temperature (T2m) over the polar cap (Fig. 1.3a and Fig. 2.3b) and is used as a criterion for identification of Arctic spring onset (ASO) events. Due to the uneven distribution of land surface and weather systems at high-latitude regions during the cold season, the spatial structure of temperature will be highly influenced by the local surface thermal capacity and heat transport associated with atmospheric circulations. In this chapter, the spatial-temporal structures of meteorological variables are analyzed via event composite analysis.

The general synoptic characteristics of ASO are studied using composite analysis. Both T2m and T2m anomalous (departure from the climatology) fields are analyzed to study the horizontal warming patterns associated with ASO events. A two-tailed student t-test (Wilks 2011) is used to test the statistical significance of anomaly fields. The composite analysis procedure is also later applied to the sea level pressure (SLP) field in order to characterize the synoptic behavior of ASO.

As will be illustrated in Section 3.3, although the regional warming patterns observed during ASO exhibit considerable interannual variability, they generally fall into three to four pattern categories. As such, we further pursue a synoptic classification and cluster analysis to categorize the resulting warming patterns. The synoptic classification is based on a simple visual identification of the location of the primary warming signature.

This approach is supplemented by a separate cluster analysis of the warming patterns. To isolate distinct spatial structures related to ASO, we use the hierarchical cluster method of Ward (Ward 1963), which has been widely used to categorize northern hemisphere wintertime geopotential height patterns (e.g, Cheng and Wallace 1993). The Euclidean distance between the anomaly maps is used as the measure of similarity. At each step, for each cluster, the sum of the Euclidean distance between all maps in the cluster and the centroid of the cluster (which is the average of all the maps within the cluster) is calculated and noted as the error sum of square for that cluster. The total of the error sum of square for all clusters is used as a criterion for the merging of the next step. All possible pairs of two maps merged together are tested. The pair of maps that is merged next is the one that guarantees a minimum increase in the total of the error sum of squares for all clusters. Further details of the clustering method can be found in Ward (1963) and Cheng and Wallace (1993).

3.2 Warming Structure

The vertical and horizontal structure of the warming pattern occurring during ASO is isolated via a composite analysis. For the 32 ASO events, a sequential composite analysis of synoptic variables (e.g., T2m, SLP) is performed for a 45-day period extending from 20 days prior to RoC ASO (denoted as day 0) to 25 days after onset. The timing of ASO varies from case to case but occurs within a period of marked climatological seasonal transition. Field variable anomalies are calculated by first removing the smoothed daily climatology prior to compositing. The resulting composite anomalies include coherent and statistically significant features since the behavior in each case typically differs appreciably from the climatological seasonal trend (annual cycle).

Figure 3.1 displays the composite time evolution of mean air temperature anomalies averaged over the latitudinal band extending from 70ºN and 85ºN. The analysis extends from 1000mb to 100mb. It illustrates the typical vertical structure of the air temperature anomalies during the ASO. We note that the significant temperature anomaly signature is restricted to tropospheric levels and extends no higher than 300mb. During the warming period (which begins at day 0), the air temperature anomaly signature is initially negative (below climatological values as in Fig. 2.3b), weakens in amplitude as temperatures approach climatological values (around day 15), and eventually becomes positive (exceeding climatology) around day 20. The majority of the warming is observed to occur in the two-week period following onset (day 0).

The "rapidity" of the transition process can be interpreted in two ways: First, the magnitude of the total air temperature increase (climatological seasonal trend plus anomaly) after ASO is greater than that occurring before onset, consistent with the RoC identification procedure. Second, the lower tropospheric air temperature shifts from a colder-than-climatological state (shown as negative anomalies in Fig. 3.1 and depicted by the red line in Fig. 2.3b) to a warmer-than-climatological state (positive anomaly in Fig. 3.1), indicating a temperature increase that is faster than the climatological-mean seasonal transition in air temperature observed during ASO. This warming occurs mainly in the 15 days after ASO as the temperature anomaly evolves from large negative values to near zero as the total temperature field approaches climatological values.

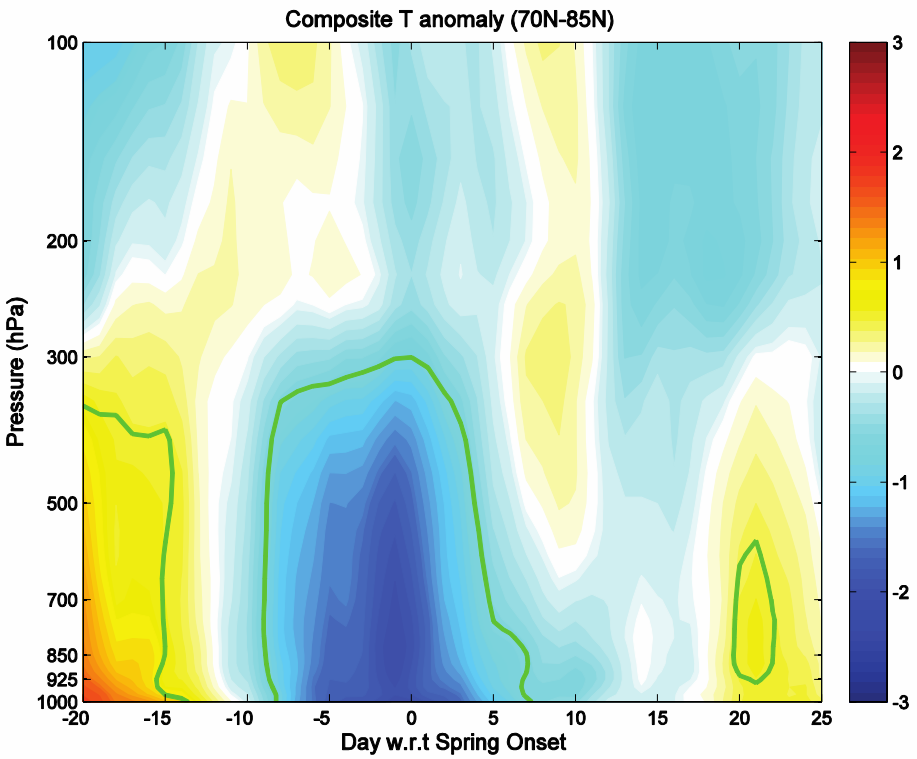

Figure 3.1: Composite vertical cross section of areal-averaged air temperature within the latitudinal band between 70 ºN and 85 ºN from 1000 to 100 hPa. Day 0 is the ASO date; negative lags indicate pre-onset days while positive lags are post-onset days. Then green lines represents the 0.95 level of confidence in a Student's *t* test.

The composite horizontal structure of the associated surface air temperature changes is shown in Fig. 3.2, in terms of local changes in both total and anomalous T2m. A remarkably zonally asymmetric structure emerges in both maps. In the left panel we observe that T2m is increasing almost everywhere during ASO (which, in itself, is not surprising). Although T2m increases robustly over the Arctic Ocean, the largest T2m increases occur over the high latitude portions of the main continents with gradually decreasing magnitudes toward the south. T2m changes over open ocean regions are relatively weak, as might be expected. The right panel displays corresponding changes in the T2m anomaly field after removing the mean seasonal cycle (which is done prior to compositing). Thus, positive values in the right panel represent local T2m increases that exceed climatological T2m increases while negative values indicate regions where T2m increases more gradually than climatology (or even decreases). Similar to the structure in the change of T2m total field, there are significant increases evident over the Arctic and high latitude continental regions. North of 75ºN, an approximately zonally-symmetric pattern of strong and statistically significant increases are observed over the Arctic. South of 75ºN, considerable zonal asymmetry is observed. In the west hemisphere, the T2m increase pattern extends southward to cover portions of the Canadian Northwest Territories and Greenland. In the east hemisphere, the most prominent signature is a strong T2m increase pattern over Northern Siberian. The strong spring time warming observed at high latitudes is consistent with the fact that meteorological variables exhibit larger magnitude seasonal cycles at high latitudes than lower latitudes (Hartmann 1994).

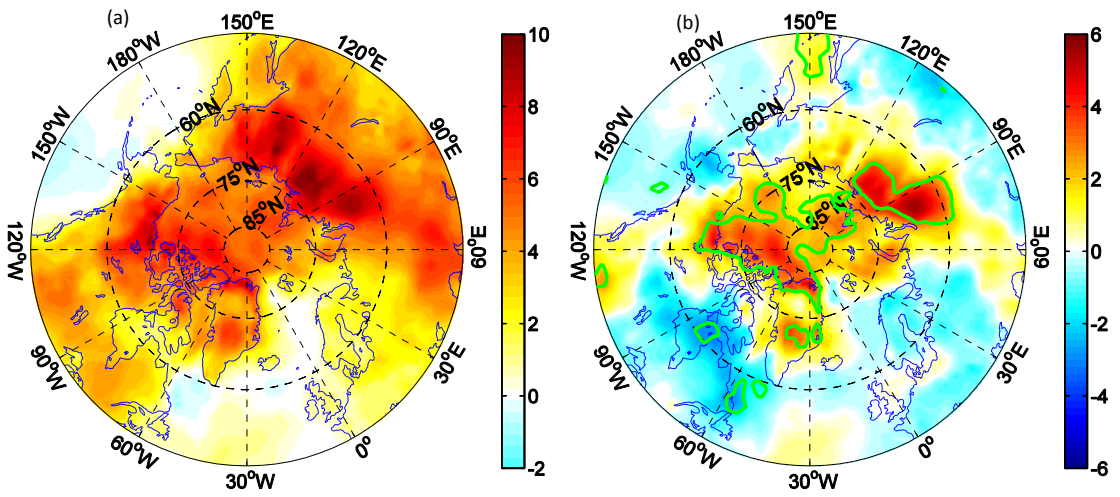

Figure 3.2: (a) Composite map of T2m changes (ºC) between days 0 and 15. (b) Composite map of the change in T2m anomaly field (ºC) between days 0 and 15; green contours represents the 0.95 confidence level from a Student's *t* test.

These composite maps isolate the T2m increase pattern common to most of the 32 events considered, while case-to-case variability is removed. As will be discussed in the following section, the individual warming patterns demonstrate remarkable case-to-case (interannual) variability. Nonetheless, almost all the events exhibit the robust T2m increase observed in the composite analysis over northern Siberia. Therefore, we hereafter denote North Siberia as the "critical" warming region. Generally speaking, North Siberia is characterized by marked surface variability. Past studies have concluded that the semi-

permanent system over the critical region of north Siberia, the Siberian High, is the most important large-scale circulation system occurring during boreal winter and strongly controls temperature and precipitation variability on multiple time scales (Gong and Ho 2002; 2004).

3.3 Categorizing Events

3.3.1 Synoptic Classification

As is shown in Fig. 3.2, the strongest warming in the composite analysis occurs over the critical region. However, a study of individual cases reveals that there are distinct regional flavors in the primary large-scale warming patterns. A synoptically-based algorithm is applied to each map of increase in T2m anomaly in order to assess the primary warming regions: For each event, contiguous regions of large T2m increases spanning at least 45 degrees of longitude and 12 degrees of latitude are first identified. We then categorize events into groups according to the regional central location(s) of the contiguous regions identified. We find that warming signatures commonly occur in four high-latitude (60ºN - 90ºN) sectors: the critical region over North Siberia (CR), the Greenland-North American continent (G-NA), East Asia (EA), and Alaska (AL). We note that multiple warming regions are sometimes active during an individual event. In such cases, we assign that event to each category in which it fits. Thus, we end up with 17 cases that exhibit warming signals over the critical region, 11 over Greenland-North America, 10 over East Asia, and 7 over Alaska. As discussed above, the four categories are not mutually exclusive. For example, since T2m anomaly warming occurs over both the critical region and Alaska during spring 1979, we assign the 1979 event to both categories in our analyses.

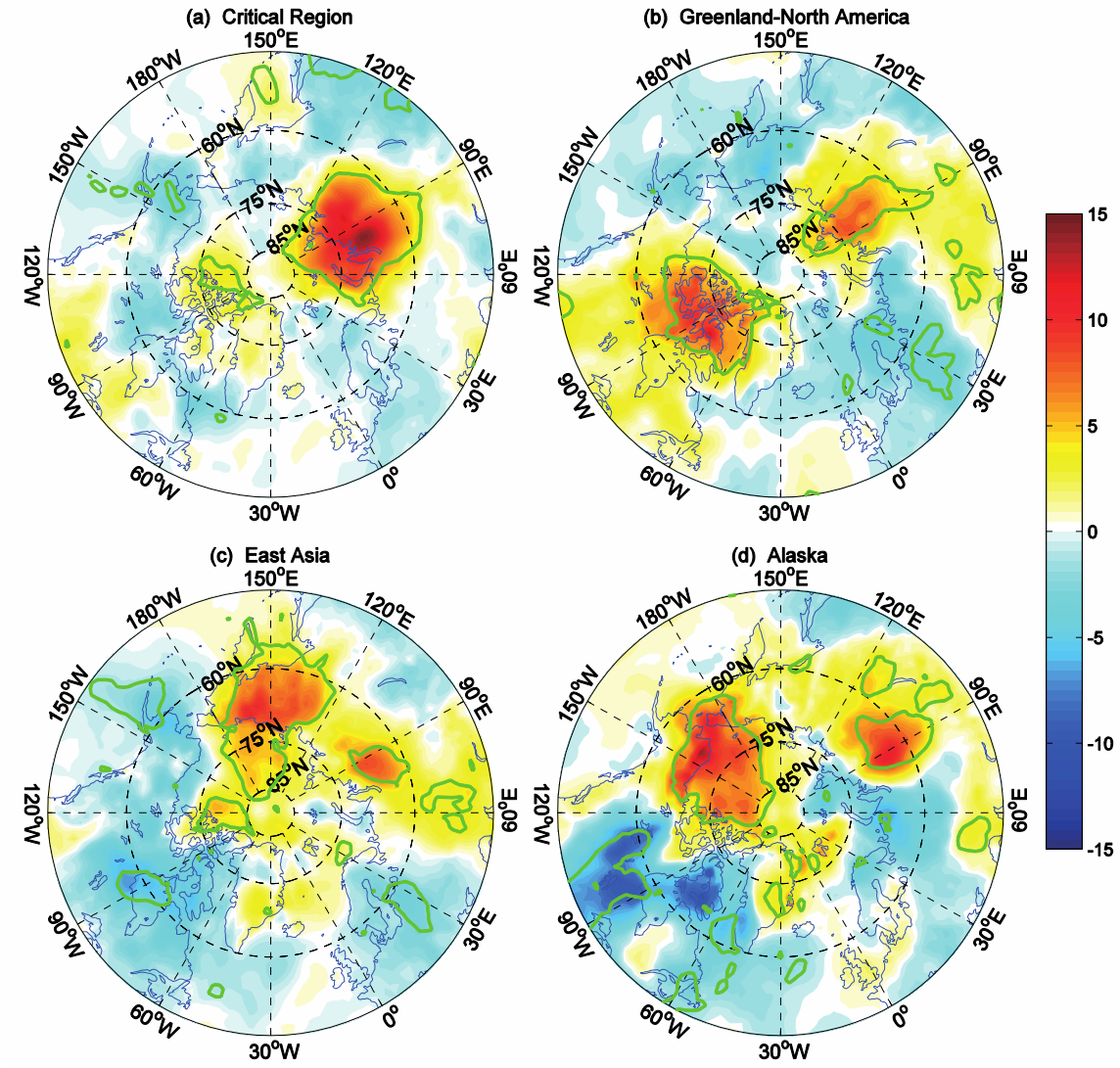

Figure 3.3: Composite map of the change in T2m anomaly field (°C) between days 0 and 15 for the four categories from synoptic classification: (a) CR category, (b) G-NA category, (c) EA category, and (d) AL category. Green contour represents the 0.95 confidence level from a Student's *t* test.

Figure 3.3 provides maps of the composite 15-day increase in T2m anomaly for the 4 categories. In Fig. 3.3a, the composite map for the 17 critical region events demonstrates a strong warming signal covering much of western Siberia. Compared with the composite map of all 32 events, more than 2/3 of the critical region is covered by the robust temperature increase (at the 0.95 confidence level) while the western hemisphere has a much weaker warming signal in these cases. Figure 3.3b shows the composite map for the Greenland-North America events. The warming pattern over the western hemisphere extends much further south into North America and eastward to the western edge of the Greenland plateau. A relatively weak but significant warming signature is also found over the eastern portion of the critical warming region. The composite map for the East Asian events is provided in Fig. 3.3c. T2m anomaly increases are observed over portions of the Arctic Ocean, East Siberian Sea, and Eurasian high latitude continent. Two substantial warming centers are found over East Asia and a portion of the critical region, respectively. Figure 3.3d displays the analogous composite map for the Alaskan category of events. These cases exhibit a broad statistically significant warming pattern that extends over the Bering Sea, Chukchi Sea, northern Alaska, and a large portion of the Arctic Ocean. A significant warming signature is also observed in the southern portion of the critical region. To summarize, besides the critical region cases (Fig. 3.3a), each of the other three groups have warming patterns that are characterized by (a) a primary warming center over the region indicated by the group name and (b) a secondary center that overlaps the critical warming region identified in the composite analysis of all cases (Fig. 3.2b). The differences noted in the primary warming features for each category suggest important interannual

differences in the factors leading to rapid T2m increases while the shared warming feature over the critical region suggests that a common forcing mechanism exists in this region.

3.2.2 Cluster Analysis

To more objectively categorize ASO events, a hierarchical cluster analysis using Ward's method is applied to the 32 annual maps of 15-day change in T2m anomaly during ASO. Figure 3.4 displays the last three merging steps of the cluster analysis. Two primary cluster branches of similar sample size (15 and 17) emerge at the last step in the analysis. The cluster having 15 events consists of three sub-branches, of which two are very small in size (2 and 3 events, respectively) while the other is relatively large (10). The four clusters deemed of primary interest are denoted as CR for critical region, NAmerica for North American continent, NAmerica-CR for North America-critical region, and up-CR for upstream of critical region. These designations are based on the location of main T2m anomaly warming signatures in the corresponding composite maps (Fig. 3.5).

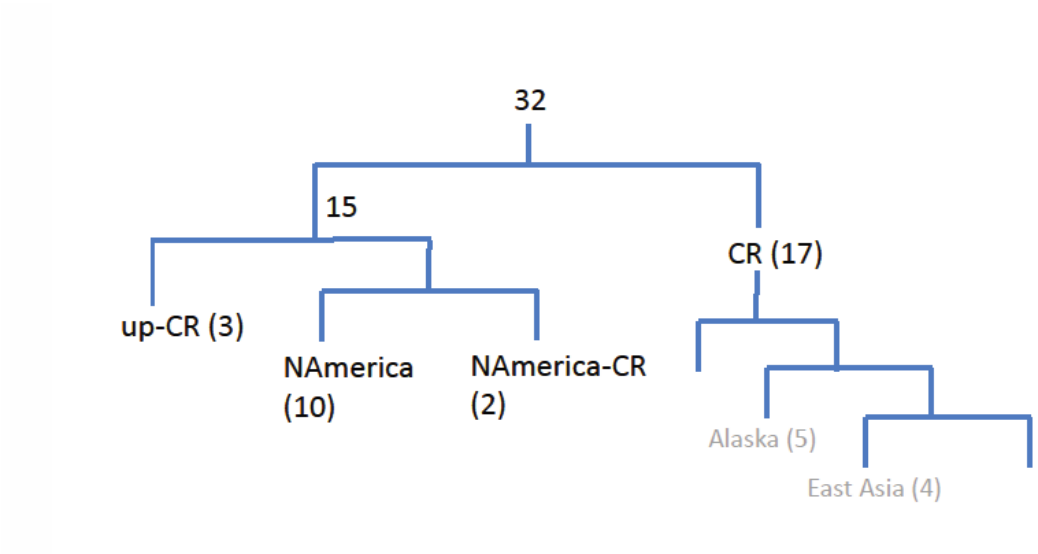

Figure 3.4: Cluster tree of the last three merging steps in the hierarchical cluster analysis.

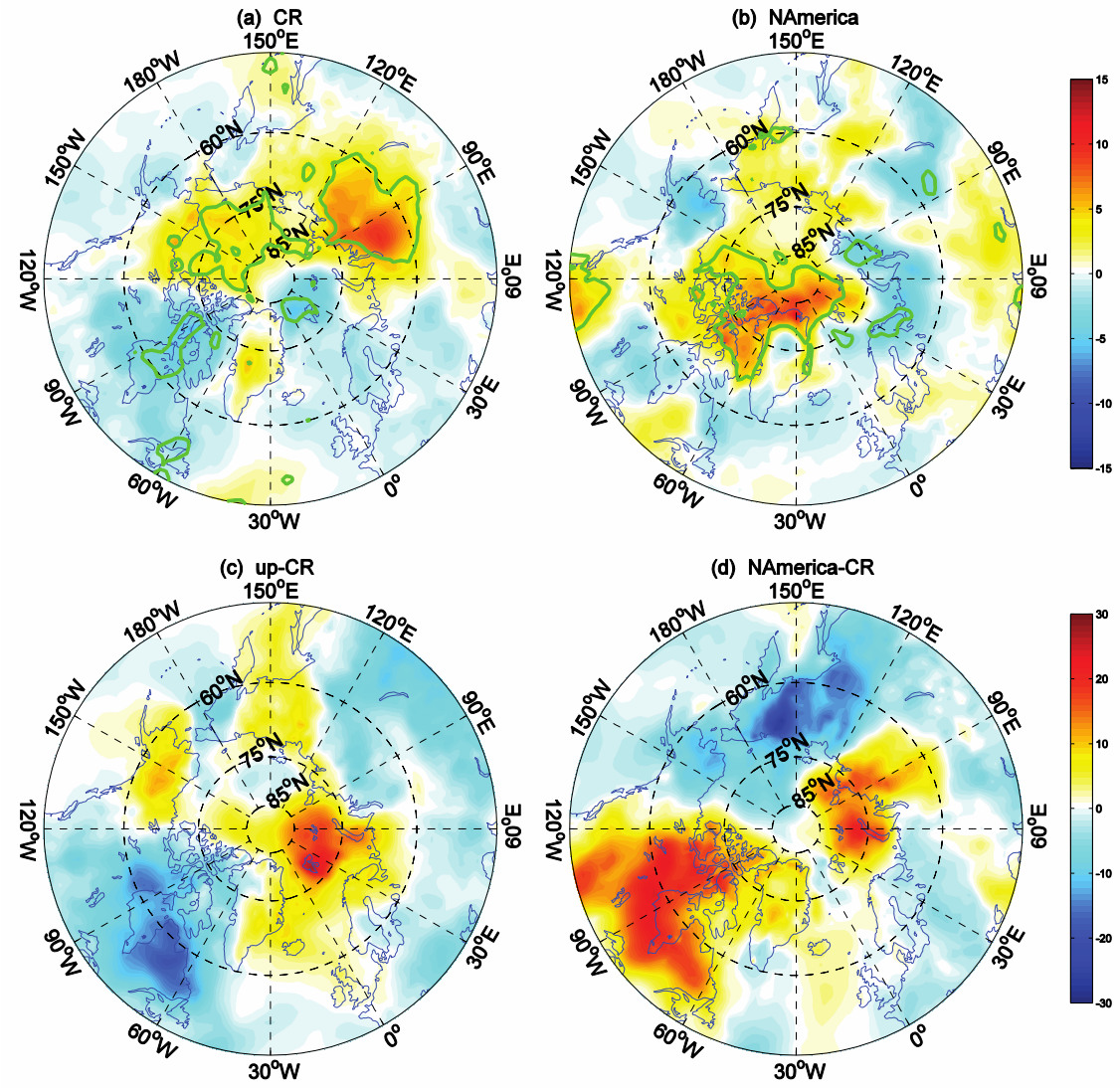

Figure 3.5: Composite map of the change in T2m anomaly field (ºC) between days 0 and 15 for the four categories from cluster analysis: (a) CR category, (b) NAmerica category, (c) up-CR category, and (d) NAmerica-CR category. Green contour represents the 0.95 confidence level from a Student's *t* test.

Despite the small sample size, the NAmerica-CR cluster (2 elements) and up-CR cluster (3 elements) each consist of events closely resembling one another. The NAmerica cluster (Fig. 3.5b) exhibits a robust warming signature over the North American sector extending through the northern edge of Greenland toward the North Pole. This pattern has a strong overlap with that associated with the Greenland-North America category in our earlier results of synoptic classification (Fig. 3.3b). More than half of the 32 events lie in the CR cluster, which is characterized by a prominent warming signature over the critical region as found in the 32 case composite map (Fig. 3.2). In the CR composite map (Fig. 3.5a), the largest amplitude warming signature occurs over the critical region with a weaker warming signal downstream north of the Bering Strait and Alaska.

In categorizing the events from synoptic classification, we ended up with one relatively small category characterized by warming in the Alaska sector (Fig. 3.3d). No single group having such a character appears as a unique branch in our more objective cluster analysis. However, the composite map for the CR cluster does, in fact, have a warming signal near Alaska sector. Considering the earlier merging steps in our cluster tree (Fig. 3.4), we find that 5 events with warming over Alaska are clustered together in the first few steps of the cluster analysis and later on merged with other clusters into the CR cluster. That is to say, events having Alaska warming (a) share a very similar spatial pattern to that isolated in the early steps of our cluster analysis and (b) also contain a non-negligible warming signature in the critical region (as confirmed by examining individual maps or the Alaska composite in Fig. 3.3d) so that they are eventually folded into the CR cluster during the later steps of our cluster analysis. Four events with warming over East Asia exhibit behavior similar to the Alaska warming events and they are also merged into the

CR cluster during the early stages. The events characterized by Alaska and East Asia warming are indicated in the cluster tree in grey even though they are not separate categories in the final cluster grouping.

The reader should keep in mind that in the cluster analysis events are merged together due to their similarity in spatial structure and each event is only allowed to belong to one cluster. However, the synoptic classification allows individual events to be placed in more than one category. Therefore, the fact that several of the 17 events in CR cluster have warming signatures over Alaska (5) or East Asia (4) does not imply that critical region warming is restricted to only the other 8 events in the CR cluster. Instead, a strong warming signature over the critical region is common among all CR events. Generally speaking, although the results from the synoptic classification and objective categorization approaches do not precisely correspond, the objective cluster analysis does similarly isolate the dominant regions of the rapid T2m increase during ASO. It also suggests a complex case-to-case variability in ASO. Since the synoptic classification not only allows for a larger sample size within each group, but also provides a well-defined spatial separation among the primary warming regions, our following composite analysis is focused on the synoptically-categorized events.

3.3 Evolution of Circulation

In this section, we study how the large-scale atmospheric circulation typically evolves during the ASO. The semi-permanent pressure systems, namely the Aleutian Low, the Siberian High, and the Icelandic Low, dominate the atmospheric circulation during boreal winter. In a climatological sense, the magnitude of these surface pressure systems weakens during spring (as shown in Fig. 3.6, the climatological trends of SLP during spring

onset demonstrate a significant increase over the oceanic low pressure systems and a significant decrease of the continental high pressure systems), resulting in large-scale changes in the atmospheric circulation. We first study the composite behavior considering all 32 annual events as a single group.

Prior to ASO (Fig. 3.6a), both the Aleutian Low and the Siberian High are stronger in magnitude than climatology (not shown) while the Icelandic Low is weaker and shifted eastward compared to climatology. During ASO, both semi-permanent low systems shift eastward in relation to the climatological features. By day +15 (Fig. 3.6b), the center of the Icelandic Low moves northeastward, extending into the Kara Sea. Figure 3.6c displays the map of the composite SLP difference between day +15 and -5. The change in the Icelandic Low is reflected by the SLP increase over the Atlantic-west Europe coast and the broader area of SLP decrease extending through the Barents Sea, Kara Sea, and northernmost Eurasia. Meanwhile, south of the critical region, the Siberian High markedly weakens and shifts northeastward, in association with a significant SLP decrease over central Siberia along with a region of little or no SLP change to the northeast of the initial high pressure center. Interestingly, another region of significant SLP decrease is observed over the mid-latitude East Asian coast. This is associated with a weakened Siberian High and a westward extension of the tail of the Aleutian Low. The central pressure of the Aleutian Low increases quite markedly; however, the resulting low pressure pattern extends zonally upstream through the west Pacific into East Asia, in association with significant SLP increases over the central north Pacific along with pronounced SLP decreases over easternmost Asia.

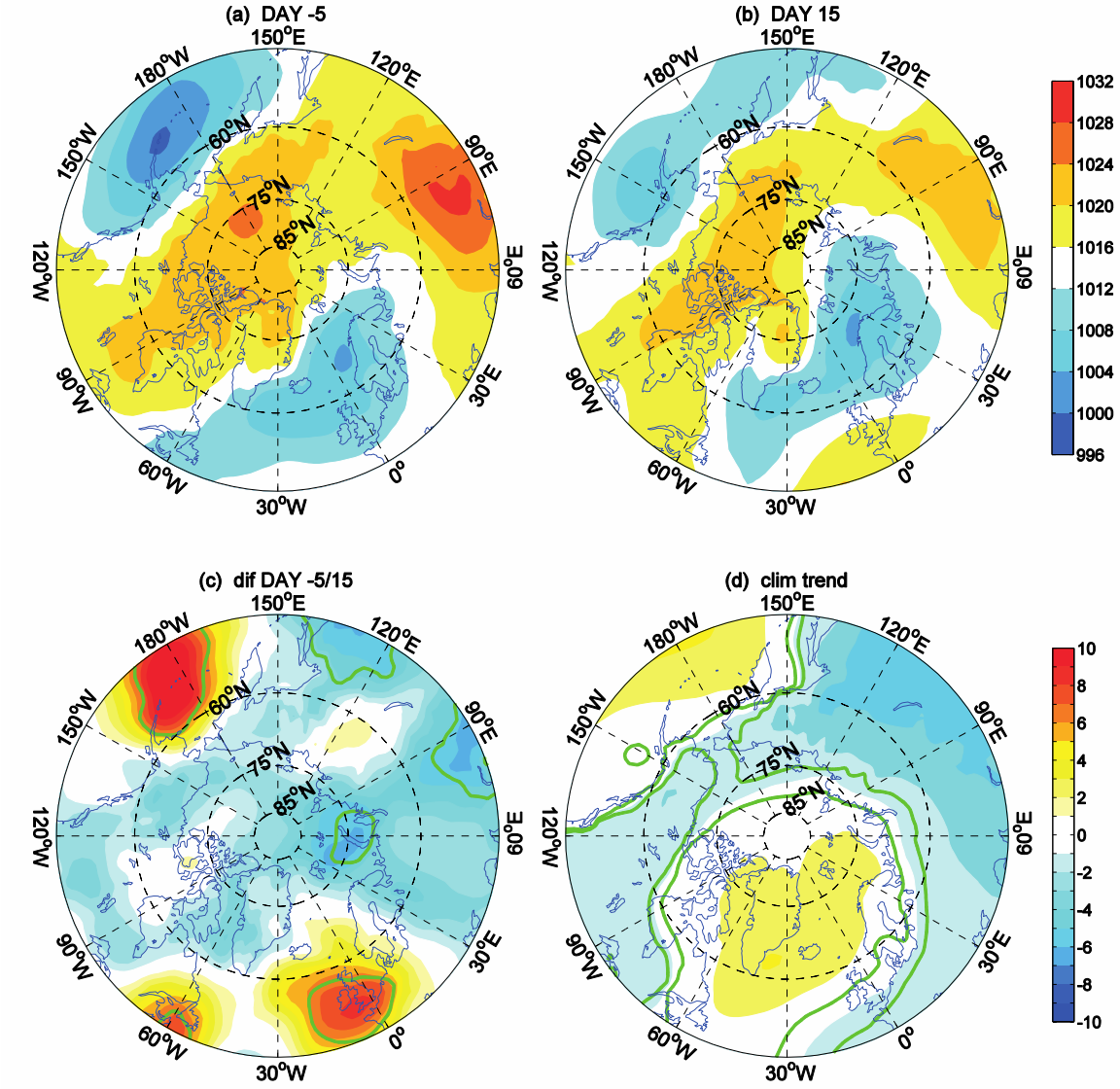

Figure 3.6: (a-b) Composite map of SLP (hPa) at days (a) -5 and (b) +15. (c) Composite map of the SLP difference (hPa) between days -5 and +15. (d) Composite map of difference in the SLP climatology (hPa) between days -5 and +15.

As will be demonstrated later, anomalous temperature advection is mainly due to the interaction of the anomalous horizontal circulation with the climatological-mean temperature field. Figure 3.7 superposes composite wind vector anomalies upon the climatological-mean T2m field averaged over the 15-day period following ASO (when maximum warming occurs). A systematic southwesterly flow is observed in the southern critical region with southeasterly flow over the eastern portion of the critical region. Meanwhile, relatively weak southeasterly wind anomalies are observed over the coastal region of East Asia. The cross-gradient anomalous circulation results in robust warm advection over a large portion of the critical region.

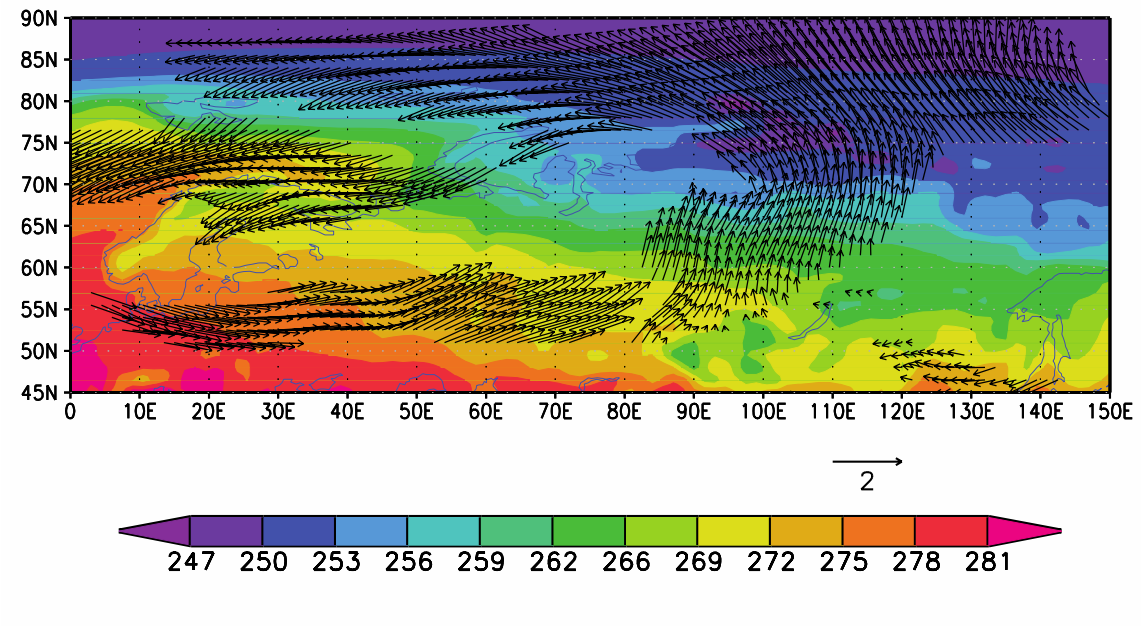

Figure 3.7: Composite of anomalous wind vectors (m/s) at 925 hPa and T2m climatology (K) averaged between days 0 and +15.

During the period of ASO, perturbation in the Icelandic Low and Siberian High jointly provide a northward pathway within the critical region for warm advection in association with southerly geostrophic flow. Meanwhile, the emerging low pressure system along coastal East Asia helps to bring relatively warm and moist air onshore from the western North Pacific. These two pathways of warm advection appear to be the primary source of rapid warming over the critical region. In addition, the concurrent weakening Siberian High results in less favorable conditions for cold air mass formation thereby reducing the inland cold air source. Our results provide an initial synoptic perspective of the rapid ASO warming and suggest an important role for dynamical processes in ASO.

The same synoptic analysis is additionally applied to each of the four categories from our synoptic classification scheme (Figs. 3.8-3.11). The evolving behavior of the surface semi-permanent synoptic features is qualitatively similar to the composite results discussed above for all 32 years (Fig. 3.6): The intensifying southerly flow located east of the migrating Icelandic Low along with the easterly flow associated with deepening low pressure over the westernmost North Pacific provide warm advection; the weakening Siberian High reduces the potential for cold air mass formation. As discussed in Section 4.2, the critical region serves as a secondary warming region in the other three ASO categories. Parallel behavior in the Siberian High, Icelandic Low, and East Asia coastal low pressure is also observed in the other categories, suggesting a common synoptic condition that favors Northern Siberia as a critical region for the rapid increase in surface temperature during ASO.

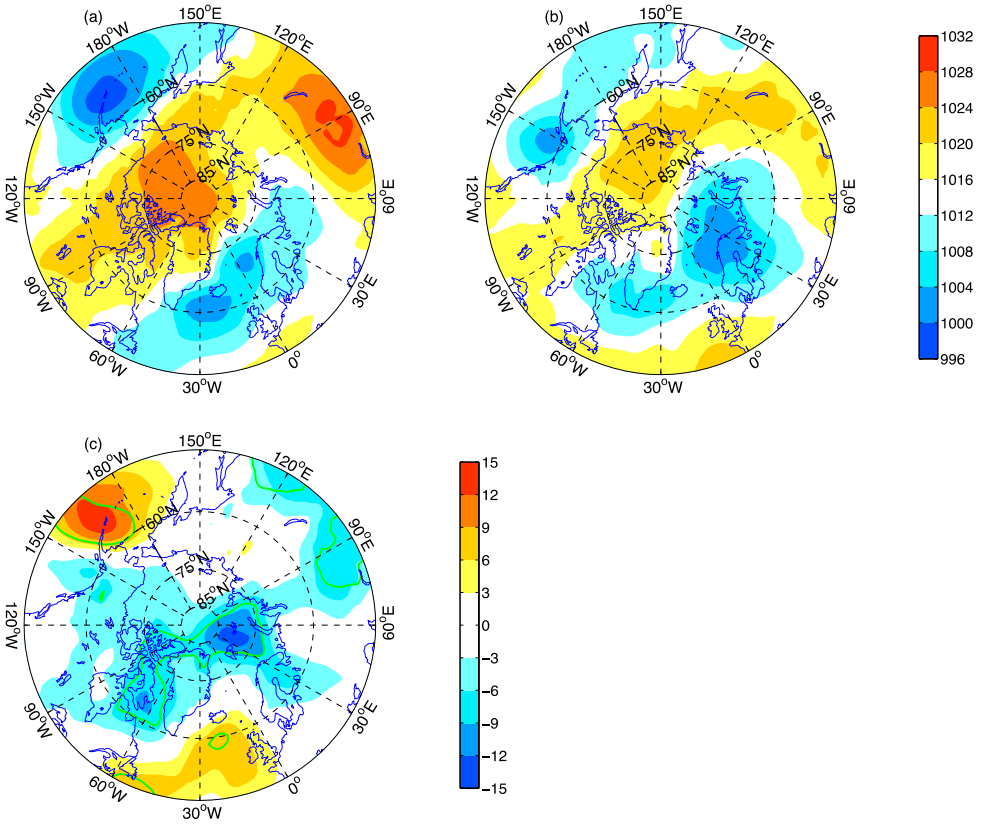

Figure 3.8: Composite SLP maps for the CR category. (a) Composite map of SLP (hPa) at day -5. (b) Composite map of SLP (hPa) at day +15. (c) Composite map of the SLP difference (hPa) between days -5 and +15. Green contours denote the difference significantly apart from 0.

Besides the critical region, the primary warming region in each of the other three categories exhibits a unique synoptic behavior in the SLP field. During ASO for the Greenland-north America category (Fig. 3.9), when warming is concentrated over northern

Canada into westernmost Greenland, high pressure over North America and the Pole weakens and shrinks in areal extent while low pressure spreads into the continental margins from both the east and west. Southwesterly flow associated with the eastward migrating Aleutian Low serves to transport warm moist air from the Gulf of Alaska into the continental interior. At the same time, easterly flow along the northern branch of the Icelandic Low carries warm moist air across Greenland into Baffin Bay, warming adiabatically upon descent. The two warm advection pathways feed into the primary warming region, with a concomitant weakening of continental high pressure and cold air mass formation. The SLP evolution of the Greenland cases (Figs. 3.9a and 3.9b) resembles that of the critical region category (Figs. 3.8a and 3.8b). This similarity carries over to the T2m anomaly change patterns: Comparing Figs. 3.3a and 3.3b, both categories demonstrate robust T2m increases in the critical region and the Greenland-North American sector. While the relative magnitude of these two warming features differ, they vary in direct relation to the concomitant differences in the regional amplitude of the SLP changes occurring in the two warming regions.

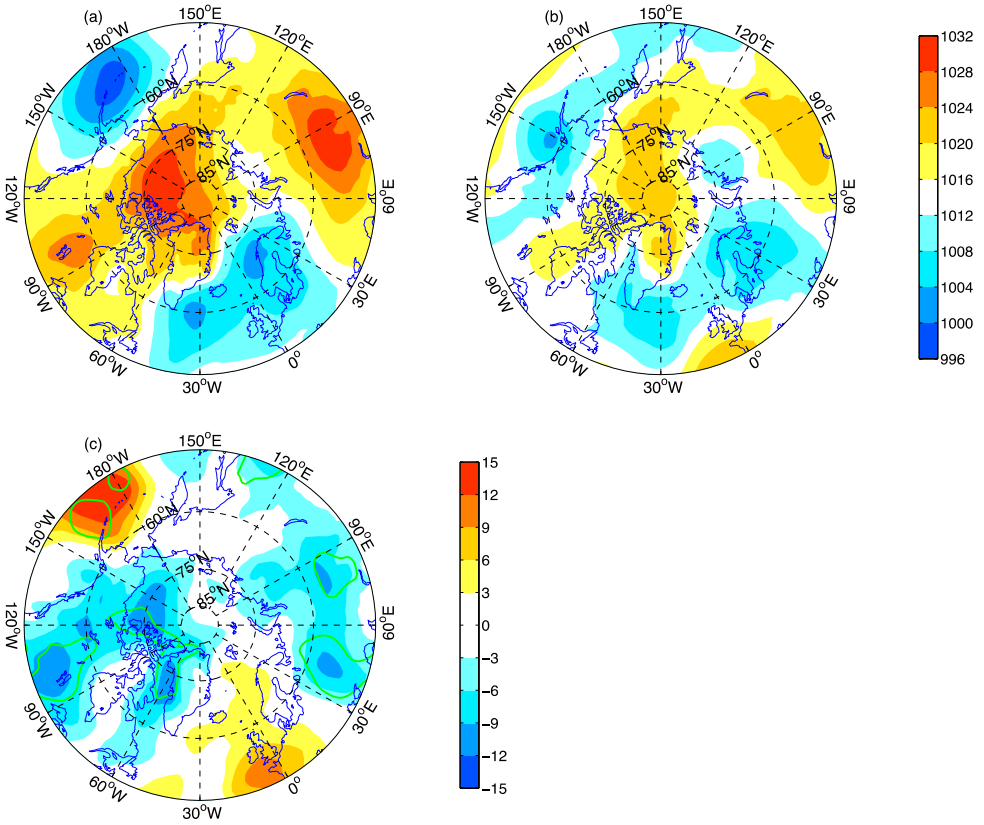

Figure 3.9: As in Figure 3.8, but for the G-NA category.

The other two categories exhibit very different synoptic behavior compared with the critical region and Greenland-North American composites. For East Asian events (Fig. 3.10), the Siberian High weakens but extends northeastward to the east coast of Russia resulting in a significant SLP increase along the coast. This high pressure extension not only increases the SLP locally over East Asia, but it also prevents the low pressure

disturbance from extending into the eastern continental margin. Thus, the oceanic low pressure system is restricted to the west Pacific and the associated circulation pathway leads to the transport of warm moist air across the Bering Sea and the Sea of Okhotsk into East Asia. In the Alaskan composite (Fig. 3.11), the Aleutian Low shifts slightly westward while the surface high pressure over the North American continent strengthens and extends into the westernmost North Pacific (a behavior opposite to that observed in the critical region composite). In this case, the associated geostrophic flow between the Aleutian Low and continental high effectively transports warm air from the Gulf of Alaska.

To summarize, our synoptic analyses indicate that the rapid regional warming signatures observed during the different types of ASO are closely tied to atmospheric circulation changes brought about by relatively rapid alterations in the strength and structure of well-recognized semi-permanent synoptic features, including the Aleutian Low, Icelandic Low and the Siberian High. Heat transport due to alterations in these synoptic patterns, particularly the advection of climatological temperature by the anomalous circulation field, plays a prominent role in transporting heat to the Arctic latitudes during rapid spring onset.

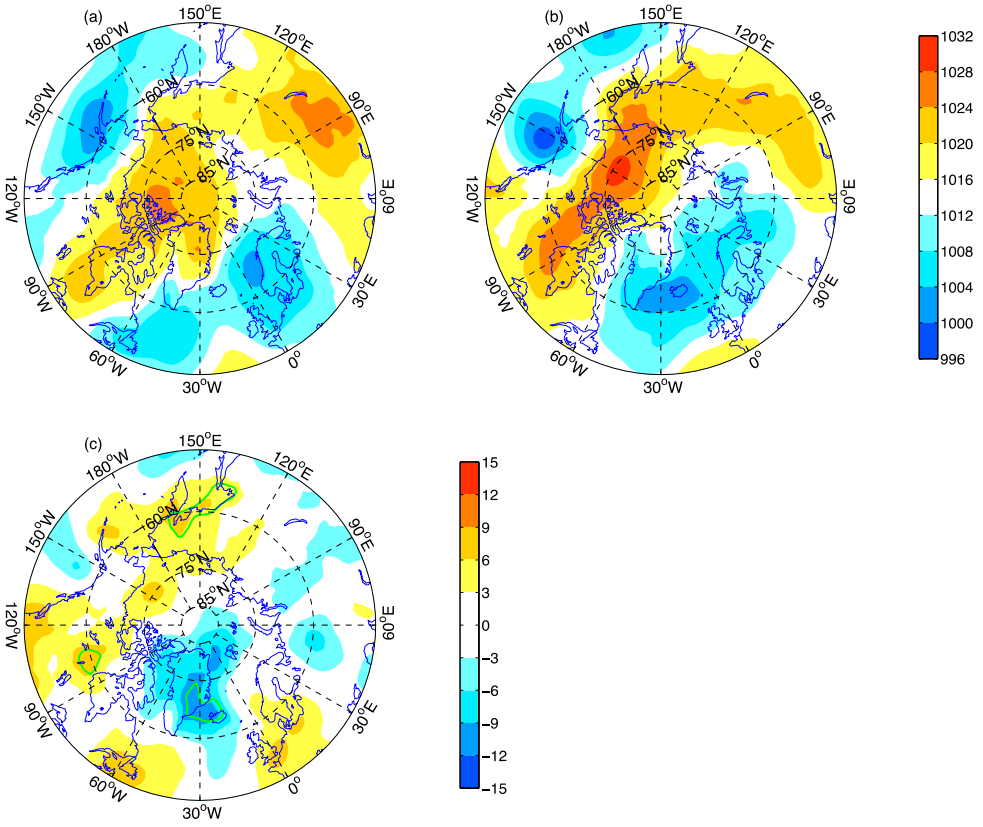

Figure 3.10: As in Figure 3.8, but for EA category.

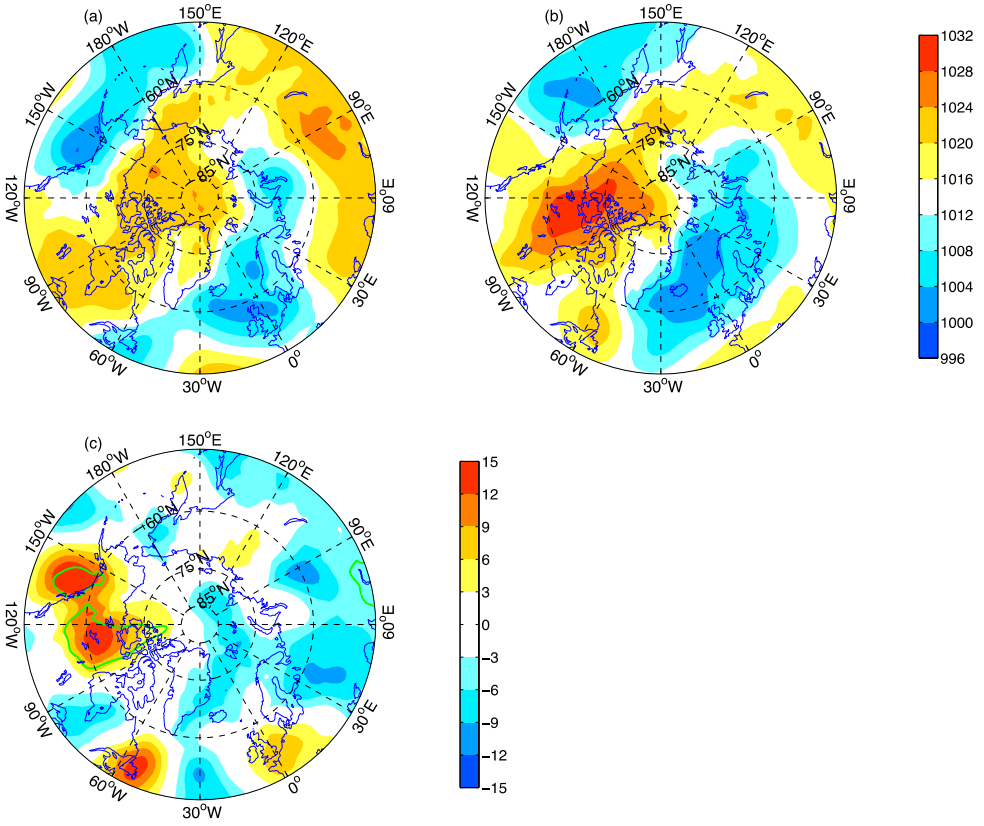

Figure 3.11: As in Figure 3.8, but for AL category.

3.4 Discussion

This chapter investigates the spatial structure of ASO T2m changes and associated SLP evolutions for the first time. To isolate common recurrent patterns, two different methods are applied to categorize warming events into groups having similar spatial structures: The first method identifies contiguous horizontal regions of T2m increase and then classifies events in terms of the central location of the warming regions; the second method applies a hierarchical cluster analysis based on Ward's method, objectively grouping similar events into the same category. Although the results obtained from the two methods differ, there is a remarkable similarity in the overall categorization. The two main branches in the cluster analysis correspond very well with the critical region category and the Greenland-North America category, respectively, obtained in the synoptic classification. The Alaska and East Asia warming categories obtained in the first classification method lie in the CR group of the cluster analysis. The remaining discrepancies mainly come from the different foundations of the two methods.

Despite slight differences in the results obtained via the two methods, both approaches uncover previously unrecognized regional warming structures associated with ASO, which can be categorized into 4 distinct groups. The unique spatial structure observed in each category is additionally linked to regional differences in the circulation anomaly patterns. In the Arctic, the springtime atmospheric circulation is influenced by stratospheric final warming events, when the stratospheric polar vortex breaks down in association with rapid warming at stratospheric altitudes (Andrews et al. 1987). During final warming events, the stratospheric circulation changes extend downward to tropospheric altitudes, leading to significant regional changes in the large-scale

tropospheric circulation (Black et al. 2006). Therefore, we originally hypothesized that Arctic spring onset may be linked to stratospheric final warming events. Although coherent decreases in zonal wind throughout the troposphere and stratosphere are observed during Arctic spring onset (not shown), we find no evidence of a causal link between stratospheric final warming events and rapid surface warming associated with Arctic spring onset. The observed rapid increase in air temperature is confined to below the tropopause with a robust signal extending from the surface to the mid-troposphere.

To further explore the tropospheric synoptic behavior of Arctic spring onset, we perform composite analyses of SLP. While the semi-permanent surface pressure systems demonstrate a weakening trend as the climatological circulation transitions from a steady state cold season toward the warm season, the anomalous circulation observed during spring onset events does not simply represent an amplification of this climatological trend. Instead, unique regional changes in the SLP anomaly field provide favorable synoptic conditions for regional rapid advective warming to occur. For the critical region and Greenland-north America events, the dominant wintertime continental high pressure system weakens dramatically while the adjacent oceanic low pressure system spreads inland, resulting in a new large-scale state characterized by (a) weakened cold air mass formation and (b) increased warm advection, both of which contribute to rapid continental warming. For the Alaskan and East Asian events, both the coastal high pressure system and oceanic low pressure system strengthen leading to a stronger geostrophic onshore flow. One complication in understanding the circulation change that takes place during spring onset events is the role of the background climatological seasonal trend (i.e., the climatological seasonal cycle). The SLP anomaly change studied here is embedded within

a gradually evolving background state. However, composite changes in the total (climatology plus anomaly) SLP field observed during spring onset exhibit a general similarity with parallel regional changes in the SLP anomaly field. This similarity suggests that the climatological seasonal transition only provides a minor contribution to the abrupt spring onset events studied here.

The strong coupling between the evolution of the SLP and T2M fields is consistent with such coupled behavior observed in earlier studies. For example, studies of the Siberian High reveal that cold surface conditions are essential to an intense high Siberian High (Takaya and Nakamura 2005) while diabatic cooling occurring within the high pressure system provides a source of surface cold air (Ding and Krishnamurti 1987; Ding 1990). Our analysis of the rapid surface warming represents a decreasingly favorable situation for the intensification of the Siberian High and formation of a cold polar air mass. Similarly, the study of anticyclogenesis over the Alaska region by Bodurtha (1952) identifies a pre-existing surface cold air mass subsequently altered by coherent warm advection from the west, which is consistent with the synoptic conditions we observe for our Alaska warming events.

The temperature increase can be further analyzed in terms of the thermodynamic equation in which the local temperature tendency is decomposed into linear advective, nonlinear advective, adiabatic and diabatic components (details in Chapter 4). Our synoptic analysis of the anomalous surface circulation in relation to the climatological-mean surface temperature field (Fig. 3.7) provides initial evidence that linear advection of climatological-mean temperature by the anomalous circulation likely provides an important contribution to the local rapid warming that occurs in southern and eastern

portions of the critical region. In a portion of the northern critical region (from the Laptev Sea westwards covering most of the Kara Sea and parts of the Barents Sea) the anomalous easterly circulation results in cold advection that locally opposes warming. However, nonlinear contributions linked to enhanced baroclinic eddy activity may also play a role.

On interannual or decadal time scales the springtime atmospheric circulation is influenced by winter low frequency modes such as the Northern Annular Mode (Liu and Ding 2007; Stine and Huybers 2012) and the Pacific-North American pattern (Stine and Huybers 2012). However, during Arctic spring onset, we find no statistically significant connection to any of the leading teleconnection indices, even though there is a strong and significant decrease in SLP covering most Arctic and the critical region (Fig. 3.6c). In mid-latitudes, there are significant SLP anomaly increases over the east north Atlantic and north Pacific. Although these structures bear some resemblance to the NAO pattern, the mid-latitude centers are longitudinally phase-shifted compared to the NAO. The results suggest a complex dynamical mechanism that connects Arctic spring onset to distinct large-scale circulation anomaly patterns at synoptic and intra-seasonal time scales.

3.5 Summary

The rapid warming observed over Polar latitudes during ASO is roughly zonally symmetric while the warming patterns observed further south show more regional localization with Northern Siberia identified as a critical region in which virtually all cases demonstrate a significant warming signature during ASO. However, regional warming patterns observed outside of the critical region during ASO vary noticeably from year to year, and thus the 32 events are additionally categorized based on the primary warming regions. The synoptic evolution of sea level pressure for the composite of all 32 events as

well as the four separate categories demonstrates a strong coupling between the SLP and T2m fields, which strongly suggests that ASO events are dynamically driven by large-scale atmospheric processes.

Although the analyses in this chapter implicate atmospheric dynamical processes as important players in Arctic spring onset, additional diagnostic research is required in order to ascertain the precise physical nature of such events. To this end, Chapter 4 will focus on pursuing dynamical diagnostic analyses in order to obtain a comprehensive understanding of the physical mechanisms that are responsible. This will include a detailed heat budget analysis in which we will quantitatively assess advective (linear and nonlinear), diabatic, and adiabatic contributions to the regional lower tropospheric temperature changes occurring during Arctic spring onset.

CHAPTER 4: HEAT BUDGET ANALYSIS OF REGIONAL SPRING ONSET EVENTS OVER THE NORHTERN HEMISPHERE HIGH LATITUDE REGIONS

4.1 Introduction

Chapter 2 (and He and Black 2015) introduces three methods of identifying Arctic spring onset (ASO) events. The Arctic spring onset dates exhibit strong interannual variability with no significant long-term trends. The characteristic spatial structures associated with Arctic spring onset warming events were presented in Chapter 3. In the 32 events analyzed, North Siberia stands out as a critical region in which a strong warming signature occurs most frequently. We also observed strong case-to-case variability in the spatial structure and suggested that, for individual events, the primary warming signature may occur outside the critical region (North Siberia). Thus, based on the primary regions of rapid temperature increase observed, ASO events were further categorized into four subsets: The critical region (with a total of 17 events), the Greenland-North American sector (11), East Asia (10), and Alaskan events (7). A composite analysis of sea level pressure (SLP) evolution in Chapter 3 suggests that distinct changes in the semi-permanent surface pressure systems provide favorable synoptic conditions for heat transport into the main warming regions, implying a dynamically-driven mechanism. However, the physical processes that drive and maintain such a rapid increase in near surface temperature have not yet been identified. In particular, the contribution of large-scale atmospheric dynamical transport, including the synoptic eddy heat flux, to Arctic spring onset has not been previously assessed. In their study of persistent height anomalies over North Pacific, Dole and Black (1990) applied a heat budget analysis to study the physics of temperature

anomaly formation. They decompose the local temperature tendency field into separate contributions from (a) linear interactions between the mean flow and circulation anomalies, (b) nonlinear eddy heat transport, (c) adiabatic warming/cooling and (d) diabatic processes. Their analysis implicated linear dynamical transport processes (e.g., baroclinic growth) as dominant in the development of persistent anomalies. Thus, such a decomposition of the thermodynamic equation is an effective diagnostic tool in deducing the physical processes and dynamical mechanisms responsible for temperature anomaly formation. Here we apply an analogous heat budget diagnostic metric to study the physical nature of ASO events.

Building upon existing research, this chapter aims to provide a more quantitative understanding of the physical sources for the rapid temperature increases observed during Arctic spring onset transition via a detailed thermodynamic heat budget analysis.

4.2 Data and Methods

4.2.1 Data

The observational data used in the study are the 6-hourly ERA-interim reanalysis data set (ERAI; Dee et al. 2011) with spatial resolution of 1.5° in longitude by 1.5° in latitude from the European Center for Medium-Range Weather Forecast. The Arctic spring onset events are identified from 36 years (1979-2014) of gridded ERAI 2-meter air temperature data (T2m). Previous validation studies of reanalysis datasets over the Arctic confirm that ERA-interim is the most reliable long-term dataset despite slight biases with respect to observations from land-based and drifting stations (e.g., Jakobson et al. 2012; Simmonds and Poli 2015).

The heat budget diagnostics employ 925 hPa air temperature and horizontal and vertical winds. The heat budget calculation was also applied to the 6-hourly Modern-Era

Retrospective Analysis For Research And Applications (MERRA; Rienecker et al. 2011) reanalysis dataset (spatial resolution of 1.25° in longitude by 1.25° in latitude) from NASA (for brevity, not shown). The temporal evolution and spatial structures of the dominant physical processes contributing to spring onset warming in the heat budget analysis do not differ appreciably between the two datasets. We note that in ERAI vertical interpolation is performed to represent fields on isobaric surfaces extending below the ground. Given our focus on 925 hPa, this would only be of concern in regions of substantial topography, such as Greenland. However, even for the G-NA region (which only extends to the western coast of Greenland) this is not an issue. Given the perceived higher quality of the ERAI data, we primarily restrict our attention to results derived from ERAI.

4.2.2 Identification of Regional Events

In the identification and characterization of ASO events in Chapter 2 and Chapter 3, the abrupt ASO event is identified via the areal-average temperature over the Pole. The collection of annual ASO events are then categorized into four subsets based upon the regional location of the most prominent warming signatures. The subset sample size ranged from 7 to 17, leading to rather small sample sizes within certain categories. Although particular regions stand out during ASO for individual years, it is also recognized that spring onset must occur within each respective region during each year, albeit with varying magnitude strength and spatial structure. In order to more effectively isolate potential regional differences in a statistically robust manner, in this chapter we extend our analysis by separately applying the RoC method to T2m areally-averaged, respectively, over the four regions identified in Chapter 3 (as opposed to a single average over the polar cap). Consequently, four categories of regional events are identified, with each category

consisting of 36 regional spring onset events. The geographical boundaries of the four regions are outlined in black in the composite maps of the T2m change occurring during regional spring onset (Figs. 4.1a-4.1d) and summarized in Table 4.1. As in Chapter 3, we demote the critical region as CR, Greenland-North American sector as G-NA, East Asia as EA, and Alaskan region as AL.

Table 4.1: Geographical boundaries for identification of the 4 categories of regional events. Values in brackets indicate numbers of events with each category.

	CR (36)	G-NA (36)	EA (36)	AL (36)
Longitude/Latitude	45E—135E; 60N – 81N	117W – 54W; 60N – 84N	120E – 180; 60N – 87N	162E – 120W; 64.5N – 87N

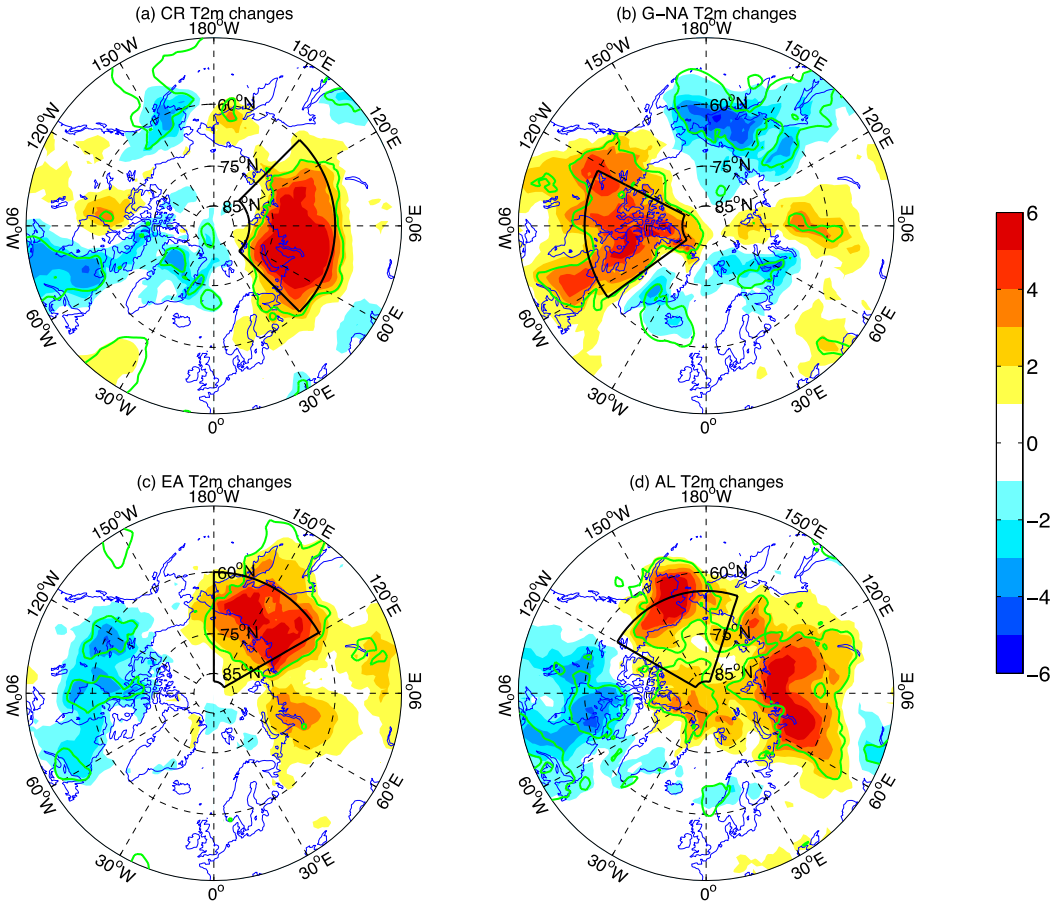

Figure 4.1: Composite maps of T2m (K) changes from day 0 to day +15 for (a) CR, (b) G-NA, (c) EA, and (d) AL events.

4.2.3 Isobaric Heat Budget Equation

To identify the dominant processes contributing to the rapid formation of near-surface air temperature anomalies, a decomposed version of the isobaric thermodynamic equation is applied separately to the four regional events. The analysis is applied to air temperature on the 925 hPa isobaric surface, a near-surface level in the planetary boundary layer, so as to represent the evolving thermal structure of the lowermost troposphere.

We first analyze the background climatological temperature tendency and its contribution from various physical processes for a seasonal period typically encompassing springtime transition. Thus, this analysis parallels the seasonal-mean heat budget analyses of Lau (1979) except for the focus on a seasonal transition period. Then, the tendency of temperature anomalies associated with the rapid spring onset warming is assessed. The derivation and physical interpretation of the heat budget equation for the climatological and anomalous temperature tendency is described in detail below.

Derivation and Physics of the Climatological Heat Budget Equation

The derivation starts with the first law of thermodynamics in the pressure coordinate system (Davis 1963):

$$\dot{q} = c_p \frac{\partial T}{\partial t} + \nabla \cdot c_p T\vec{V} + \frac{\partial}{\partial p} c_p T\omega - \alpha\omega$$

…… Eq. (1)

where $\dot{q}$ is the diabatic heating rate, c_p is the specific heat capacity, T is temperature, $\vec{V}$ is the horizontal wind vector, $\omega = \frac{dp}{dt}$ is vertical pressure velocity, $\alpha = \frac{RT}{p}$ is the specific

volume (the volume of a unit mass). Dividing Eq. (1) by c_p and assigning $\dot{Q} = \frac{\dot{q}}{c_p}$, we obtain:

$$\dot{Q} = \frac{\partial T}{\partial t} + \nabla \cdot T\vec{V} + \frac{\partial}{\partial p} T\omega - \frac{RT}{c_p p}\omega$$

…… Eq. (2)

All of the dependent variables in Eq. (2), including $\dot{Q}$, T, $\vec{V}$, and ω, can be written as the sum of the climatological value and an anomaly, that is, $A = \bar{A} + A'$, where A represents T, $\vec{V}$, ω, and $\dot{Q}$. An overbar represents a daily climatological value while a prime indicates a departure from the climatology. Subsituting this decomposition into Eq. (2), we get:

$$\dot{\bar{Q}} + \dot{Q}' = \frac{\partial(\bar{T} + T')}{\partial t} + \nabla \cdot (\bar{T} + T')\left(\bar{\vec{V}} + \overrightarrow{V'}\right) + \frac{\partial}{\partial p}(\bar{T} + T')(\bar{\omega} + \omega') - \frac{R}{c_p p}(\bar{T} + T')(\bar{\omega} + \omega')$$

…… Eq. (3)

Note that the average and anomaly fields have the following features: $\overline{A'} = 0$, $\overline{A + B} = \bar{A} + \bar{B}$, $\overline{\bar{A}B'} = 0$. For Eq. (3), the climatological-mean (long-term daily average) of the entire equation is performed and Eq. (3) becomes:

$$\dot{\bar{Q}} = \frac{\partial \bar{T}}{\partial t} + \bar{\vec{V}} \cdot \nabla \bar{T} + \nabla \cdot \overline{\overrightarrow{V'T'}} + \bar{\omega}\left(\frac{\partial \bar{T}}{\partial p} - \frac{R\bar{T}}{pc_p}\right) + \left(\frac{\partial}{\partial p}\overline{\omega'T'} - \frac{R}{pc_p}\overline{\omega'T'}\right)$$

…… Eq. (4)

Eq. (4) reveals the climatological heat budget balance. Placing the climatological temperature tendency on the left hand side and everything else on the right hand sight. Eq. (4) can be re-organized as:

$$\frac{\partial \overline{T}}{\partial t} = -\overline{\vec{V}} \cdot \nabla \overline{T} - \overline{\omega}\left(\frac{\partial \overline{T}}{\partial p} - \frac{R\overline{T}}{pc_p}\right) - \nabla \cdot \overline{\vec{V}'T'} + \left(-\frac{\partial}{\partial p}\overline{\omega'T'} + \frac{R}{pc_p}\overline{\omega'T'}\right) + \dot{\bar{Q}}$$

LTT_c A B C D Q

…… Eq. (5)

Eq. (5) is the same equation used by Lau (1979) in analyzing the winter mean heat budget at the low tropospheric levels (1000 mb and 700 mb). The physical meaning of each term is:

LTT_c: The Eulerian (local) tendency in climatological-mean air temperature. In Lau (1979) this is taken as zero since his analysis focuses on the winter-average heat balance, for which air temperature is taken as steady. However, our work analyzes a transition season, during which time the background air temperature field itself increases. In our case, we assess LTT_c from day-to-day variations in the climatological temperature rather than assuming it is zero.

A: Temperature tendency due to the horizontal advection of climatological-mean temperature by the mean circulation (wind field).

B: Temperature changes due to the climatological-mean vertical motion, including vertical heat transport and adiabatic expansion/compression.

C: The horizontal convergence of transient eddy heat flux.

D: Temperature changes due to vertical motion associated with transient eddies, including vertical heat transport and adiabatic expansion/compression.

Q: Net contribution of climatological-mean diabatic processes (assessed as a residual from all other terms to make a balanced heat budget).

<u>Derivation and Physics of the Anomalous Heat Budget Equation</u>

In order to assess the contributions for the anomalous temperature tendency, by subtracting Eq. (4) from Eq. (3), we obtain:

$$\dot{Q}' = \frac{\partial T'}{\partial t} + \bar{\vec{V}} \cdot \nabla T' + \overrightarrow{V'} \cdot \nabla \bar{T} + \nabla \cdot \overrightarrow{V'} T' - \nabla \cdot \overline{\overrightarrow{V'} T'} + \bar{\omega} \frac{\partial T'}{\partial p} + \omega' \frac{\partial \bar{T}}{\partial p} + \frac{\partial}{\partial p} \omega' T'$$

$$- \frac{\partial}{\partial p} \overline{\omega' T'} - \frac{R}{p c_p} \bar{\omega} T' - \frac{R}{p c_p} \omega' \bar{T} - \frac{R}{p c_p} \omega' T' + \frac{R}{p c_p} \overline{\omega' T'}$$

…… Eq. (6)

To illustrate the various physical processes contributing to the anomalous temperature tendency, Eq. (6) is re-organized as:

$$\frac{\partial T'}{\partial t} = \left(- \bar{\vec{V}} \cdot \nabla T' \right) + \left(- \overrightarrow{V'} \cdot \nabla \bar{T} \right) + \left[- \nabla \cdot \overrightarrow{V'} T' - \left(- \nabla \cdot \overline{\overrightarrow{V'} T'} \right) \right]$$

LTT HL1 HL2 hEHF hEHF_c

$$+ \left(- \bar{\omega} \frac{\partial T'}{\partial p} \right) + \left(- \omega' \frac{\partial \bar{T}}{\partial p} \right) + \left[- \frac{\partial}{\partial p} \omega' T' - \left(- \frac{\partial}{\partial p} \overline{\omega' T'} \right) \right]$$

VL1 VL2 vEHF vEHF_c

$$+ \left(\frac{R}{p c_p} \bar{\omega} T' \right) + \left(\frac{R}{p c_p} \omega' \bar{T} \right) + \left(\frac{R}{p c_p} \omega' T' - \frac{R}{p c_p} \overline{\omega' T'} \right) + \dot{Q}'$$

AD1 AD2 AD3 AD4 Q’

…… Eq. (7)

Eq. (7) is the heat budget equation we apply to analyze the anomalous temperature tendency for the regional spring onset events. The Physical meaning of each term is described below:

LTT: The local (Eulerian) tendency in the air temperature anomaly field. Positive values represent day-to-day air temperature increases that are more rapid than the

background day-to-day climatological-mean seasonal warming that typically occurs during this time of the year. Leading episodes of areal-averaged temperature anomaly increases represent the phenomena of interest in our study.

HL1, HL2: Linear interaction between the climatological circulation and composite anomaly field. HL1 is the advection of anomalous air temperature by the climatological circulation while HL2 is the advection of climatological-mean temperature by the composite wind anomaly field. HL2 tends to dominate over HL1.

hEHF + hEHF_c: Anomalous temperature tendency due to nonlinear processes, that is, anomalous eddy heat flux convergence (i.e., the composite-mean deviation of the eddy heat flux convergence from its climatological mean value).

VL1, VL2, vEHF, vEHF_c: Vertical heat transport terms, with each respectively analogous to the horizontal terms HL1, HL2, hEHF, and hEHF_c.

AD1, AD2, AD3, AD4: Anomalous tendency due to adiabatic expansion and compression. AD1, AD3, and AD4 are found to provide negligible contributions compared with other terms, and therefore are not discussed in the following analysis.

Q' represents the net contribution of anomalous diabatic processes and is assessed as a residual term. This residual temperature tendency does not vary appreciably between ERAI and MERRA datasets (not shown), both of which slightly exceed parallel results derived from the explicit diabatic heating estimates provided by MERRA. Given our earlier discussed decision to focus on ERAI-based diagnostics, our analysis of contributions from anomalous diabatic processes is presented in terms of ERAI residual estimates of diabatic heating.

4.2.4 Composite Analysis of the Heat Budget Equation

The decomposed thermodynamic equations derived in Section 4.2.3 is now applied to the regional spring onset events.

As discussed in Chapter 3, Arctic spring onset is characterized by a rapid temperature increase that exceeds the climatological-mean seasonal tendency. Since the spring onset timing varies dramatically from year to year (Fig. 2.2a), the representative background climatological state, from which temperature and circulation anomalies are calculated, also differs for individual years. Thus, we do not employ the common practice of determining climatological fields via the calculation of a simple multi-month average (e.g., March-April-May). Instead, in our case it is more appropriate to adopt the following procedure: First, the daily climatological value for each term in Eq. (6) is calculated and archived with respect to each day in the calendar year. Then, for each spring onset event, the climatological heat budget terms are integrated from day 0 to day 15 to assess the cumulative climatological contribution, and then composited among all events in the four regional categories.

A similar composite technique is applied to assess the anomalous temperature tendency for each of the four separate regional event categories. Each of the four event categories is analyzed separately using Eq. (7) in order to highlight any regional differences. In all 4 categories, the largest temperature increases mainly occur during the 15-day period immediately after spring onset (day 0). Thus, for each individual event within a given category, the budget terms in Eq. (7) are each first calculated on a daily basis for the period day -10 to day +15 and then the daily values are composited among the 36 events in the given category. To investigate the temporal behavior and spatial structure

of spring onset warming, 5-day average maps of the various composite heat budget terms are plotted for periods that encompass days +1 to +5, days +6 to +10, and days +11 to +15.

4.2.5 Synoptic Diagnostics

Baroclinic wave activity is analyzed using the envelope function of geopotential height at 500 hPa, that is, a 10-day lowpass filtered signal of the square root of the 2.5-6-day bandpass filtered geopotential height (Nakamura and Wallace 1990). The envelope function reflects the high frequency height variability associated with synoptic waves and is widely used in analyzing baroclinic eddy activity associated with the extra-tropical storm tracks. Past studies have used the envelope function to study the Pacific storm track response to the western boundary currents (O'Reilly and Czaja 2015) and MJO convection (Lee and Lim 2012), and the influence of synoptic waves on variability in the Polar Annular Mode (Black et al. 2012) and Stratospheric Northern Annular Mode (Lee and Black 2015). In this chapter, the envelope function anomaly is used to highlight regional patterns of anomalous synoptic wave activity, which is linked to anomalous heat flux convergence contributing to rapid warming during spring onset.

4.3 Climatological Heat Budget during Spring

The resulting maps for budget terms LTT_c, A, B, C, and Q in Eq. (6) are shown in Fig. 4.2.

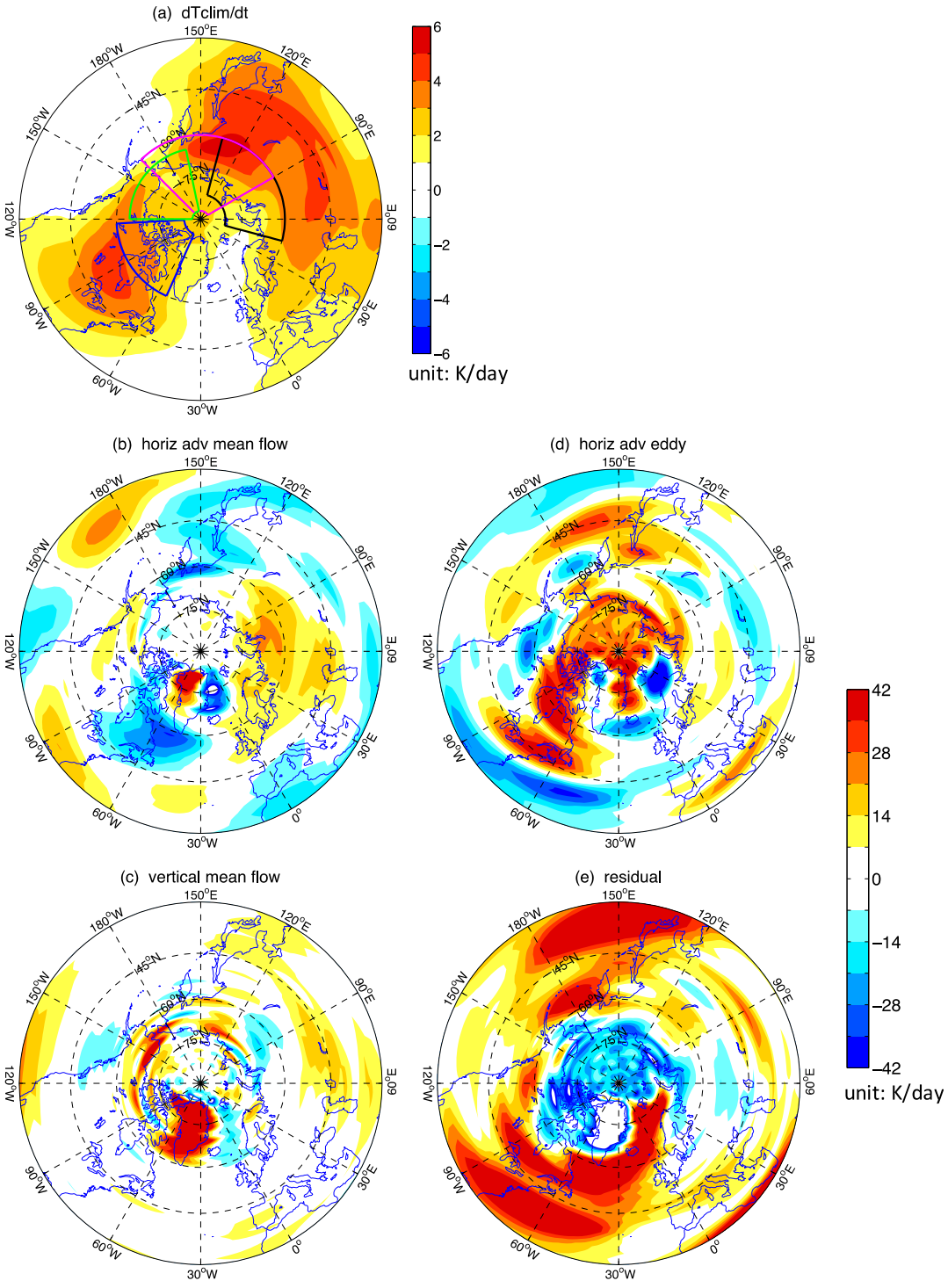

Figure 4.2: Composite heat budget balance. Composite maps of 15-day time integration of (a) LTT_c, (b) term A, (c) term B, (d) term C, and (d) term Q in Eq. (6) during average spring onset transition time. In panel (a), the four regions are outlined in black for CR, magenta for EA, green for AL, and blue for G-NA.

During spring, temperature is gradually warming up over the continents (Fig. 4.2a), at a rate that is one order of magnitude smaller than that of its 5 contributing factors (Figs. 4.2b-4.2e). Similar to the winter-mean heat budget results of Lau (1979), horizontal advection by the mean flow provides warm advection along the western continental coastlines and cold advection along the eastern continents extending outward over the Kuroshio Current and Gulf Stream. In Lau (1979), temperature changes at 700 hPa related to climatological-mean vertical motion mostly reflect adiabatic compression and expansion associated with flow over topographic features, e.g. adiabatic cooling (warming) on the west (east) side of the mountains. Such adiabatic effects are less prominent in the current analysis at 925 hPa because of the weak vertical motion close to Earth surface. However, relatively weak adiabatic cooling west of Rocky Mountains, Scandinavian Mountains, and the higher-topography of Siberia is noted (Fig. 4.2c). The contributions of the horizontal and vertical mean flow (Figs. 4.2b-c) are of opposite sign with the horizontal advection having larger magnitudes and larger spatial scales. The horizontal eddy heat flux (Figs. 4.2d) provides heat flux divergence (convergence) to the south (north) of the two baroclinically active storm tracks. Temperature changes related to transient eddy vertical velocity are negligible and therefore not shown for brevity. Strong diabatic heating patterns are found over both storm track regions and through the Bering Sea Strait and Gulf Stream where warm oceanic currents extend to higher latitudes (Fig. 4.2e).

Within the regions of interest for the four region spring onset events (denoted by latitude-longitude "boxes" in Fig. 4.2a), horizontal advection by the mean flow provides substantial warming into the CR sector, cooling into the G-NA sector with little impact over the EA and AL sectors. Transient eddy heat flux convergence contributes positively

within all four regions, as well as into the central Arctic Ocean and adjacent seas. With its large magnitude and dominant warming signature over the entire Arctic, transient eddy heat flux convergence serves as a primary contributor to Arctic spring onset in a climatological sense. Although the incoming solar radiation increases during spring, the high-latitude atmosphere remains governed by a net radiative cooling. Thus, diabatic processes provide a net climatological cooling during the period encompassing spring onset.

4.4 Heat Budget Analysis of Regional ASO events

Figures 4.1a-4.1d display local changes in the composite T2m anomaly field between day 0 to day 15 for each of the four regional spring onset event categories. The spatial structures for the 4 categories strongly parallel those identified in the subset analysis in Chapter 3: CR events exhibit robust temperature increases over north Siberia but little significant change elsewhere; the other three categories show robust T2m increases over their unique locations, as well as significant warming over the critical region.

The physical nature of the rapid warming in the near-surface air temperature anomaly field is explored via the application of Eq. (7) at 925 hPa. Figure 4.3 displays maps of the integration of LTT from day 0 to day 15, which represent the local change in the 925 hPa temperature anomaly field (T925) during this period. The spatial pattern of T925 increase closely resembles that of T2m except for EA events, for which the domain of significant warming is larger in longitudinal extent for T925 versus T2m. Therefore, our current heat budget analysis of EA events will focus on the larger domain (Thus, the black box denotes the region of EA *identification* while the magenta box denotes the region of EA *analysis*).

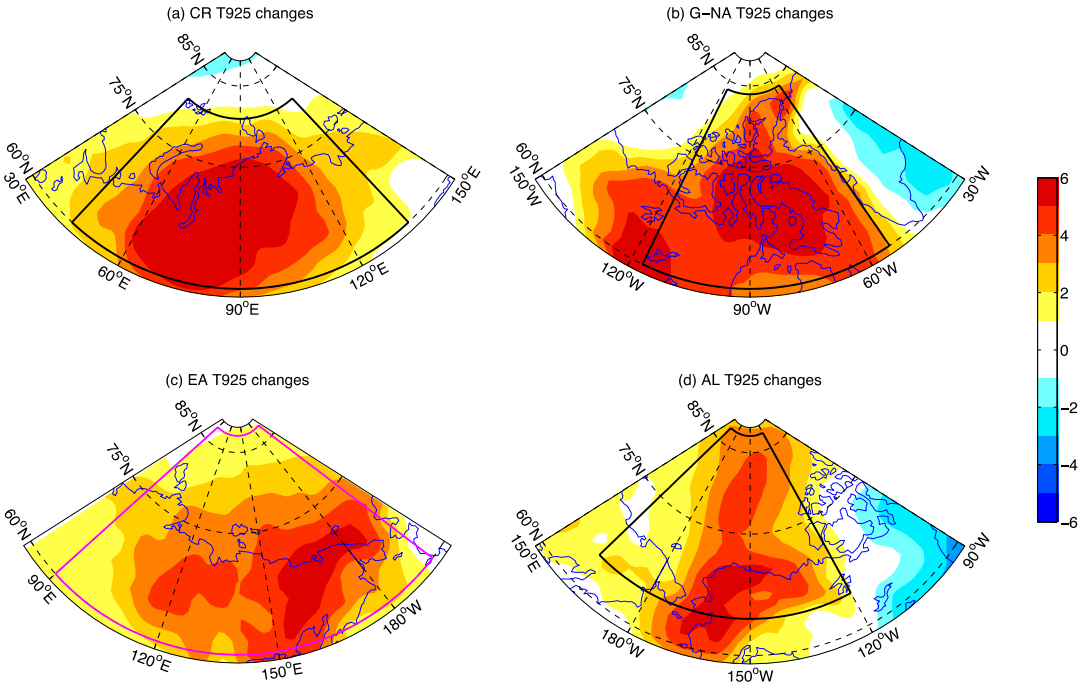

Figure 4.3: Composite maps of 15-day time integration of LTT (unit:K) from day 0 to day 15 for (a) CR, (b) G-NA, (c) EA, and (d) AL events.

4.4.1 Regional Structural Evolution and Large-Scale Dynamical Forcing

As discussed in Chapter 3, the unique behavior of the semi-permanent surface pressure systems during spring onset suggests a primary contribution from dynamical processes, more specifically, heat transport via large-scale horizontal advection and the eddy heat flux convergence of synoptic waves. To more rigorously test these ideas, here we analyze the temporal and spatial structures of T925 changes due to linear and nonlinear processes by dividing the 15-day warming periods into 3 sequential 5-day subsets and studying the sequence of 5-day average maps of the various tendency and forcing terms in Eq. (7). The primary advective terms contributing to the regional warming patterns are displayed in Figs. 4.4-4.7, respectively, for the four event categories.

The composite budget results are displayed for the CR cases in Fig. 4.4. During the early stage (day 1 to day 5), there is a small region of weak warming observed over the southwest corner of the CR event domain (Fig. 4.4a), and this is attributed to the convergence of an enhanced eddy heat flux into the domain at the southern boundary (Fig. 4.4g). Although the interior of the domain also exhibits anomalous heat flux convergence, this is largely offset by strong local cooling associated with the linear advection term (Fig. 4.4d) resulting in little or no temperature change over much of the domain interior during this time. At the middle stage (day 6 to day 10), a very robust warming pattern emerges covering most of the domain encompassing the critical region (Fig. 4.4b). This warming arises from the combined effects of eddy heat flux convergence (to the west) and large-scale linear temperature advection (to the east). During the late stage (day 11 to day 15), the warming signature weakens but remains centered within the critical region (Fig. 4.4c).

The late stage warming is largely attributed to a robust linear warm advection signature associated with a broad swath of southerly wind anomalies (Fig. 4.4f).

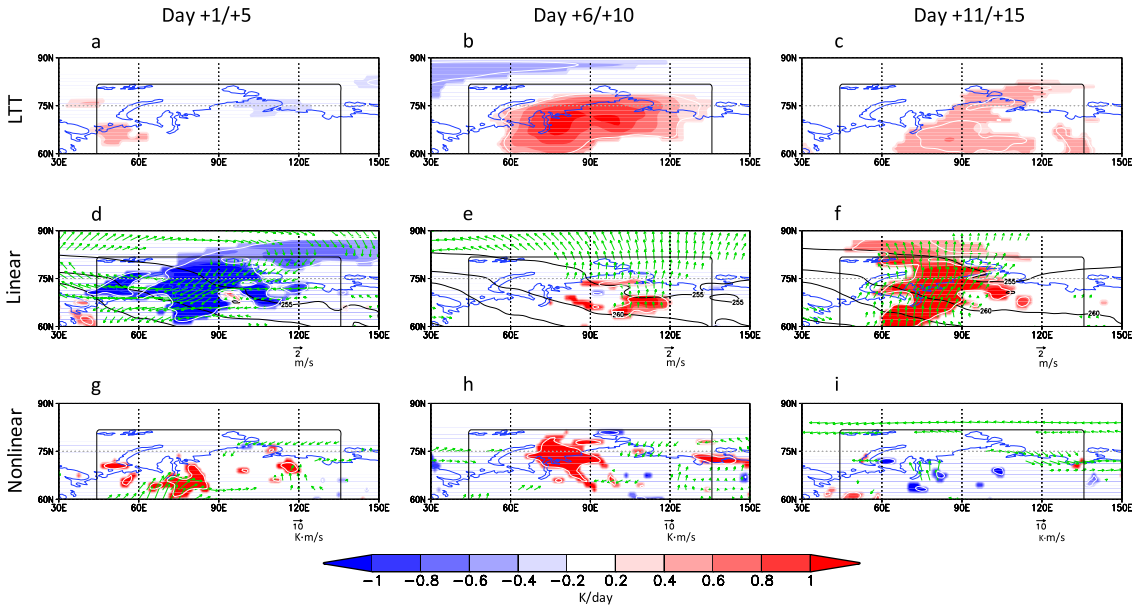

Figure 4.4: Composite maps of spatial structural evolution of temperature anomaly tendency and large-scale dynamical forcings of CR events. (a-c) Composite maps of anomalous temperature tendencies (unit: K/day). (d-f) Composite maps of linear advection (shading, unit: K/day), anomalous wind vector (arrows, unit: m/s), and climatological temperature (black contours, unit: K). (g-i) Composite maps of nonlinear term (shading, unit: K/day) and eddy heat flux anomalies (vectors, unit: K•m/s). Only values significant at the 0.90 confidence level are shaded; the 0.95 significance level is plotted as a white contour. Only vectors at the 0.95 significance level are plotted.

Figure 4.5 displays the parallel diagnostic map sequence for G-NA events. During the early stage, a coherent warming pattern is observed in the northern portion of the region (Fig. 4.5a). The linear advection term is the primary contributor to warming along the northern boundary (Fig. 4.5d). For the middle stage, the warming center shifts to the southern part of the region. Although the statistical significance is relatively weak, linear advection contributes positively to this warming signature over the Davis Strait and Victoria Islands (Fig. 4.5e). Packets of southward-directed anomalous eddy heat flux results in several smaller scale warming structures that are distributed evenly over the domain (Fig. 4.5h). Thereafter (late stage), warming remains in the south but expands northward into the central part of the domain (Fig. 4.5c). The linear temperature advection remains the main source of warming at this time (Fig. 4.5f) with more scattered contributions coming from anomalous eddy heat flux convergence over Baffin Bay, Davis Strait, and the adjacent islands (Fig. 4.5i).

The overall composite warming signature of EA events is much weaker in amplitude and limited in spatial extent compared to the other regional events (Fig. 4.6). Early on (Figs. 4.6a, 4.6d, and 4.6g), no notable warming signature is observed over most of the region. During the middle stage, a coherent pattern of significant (albeit weak) warming is observed over the East Siberian Sea and the adjacent Asian continent to the south (Fig. 4.6b). The continental warming is mostly due to linear advection while the warming over the ocean arises from anomalous eddy heat flux convergence (Figs. 4.6e and 4.6h). Thereafter (late stage), the warming signature weakens and drifts northwestward, covering the Bering Strait region and the Arctic Ocean (Fig. 4.6c), and is mainly caused by linear temperature advection (Fig. 4.6h).

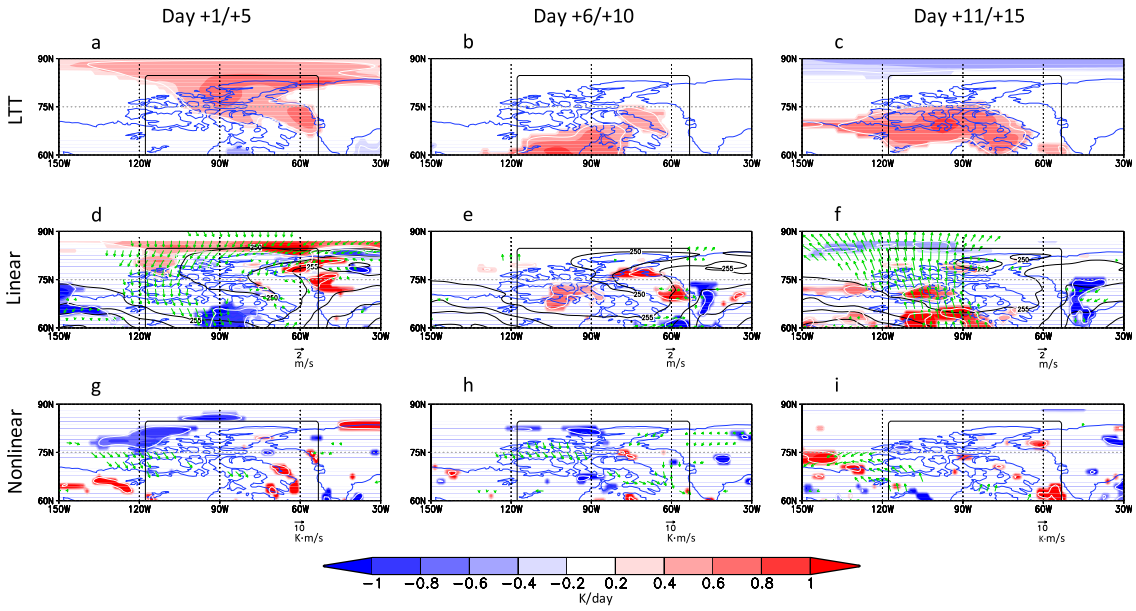

Figure 4.5: As Figure 4.4, but for G-NA events.

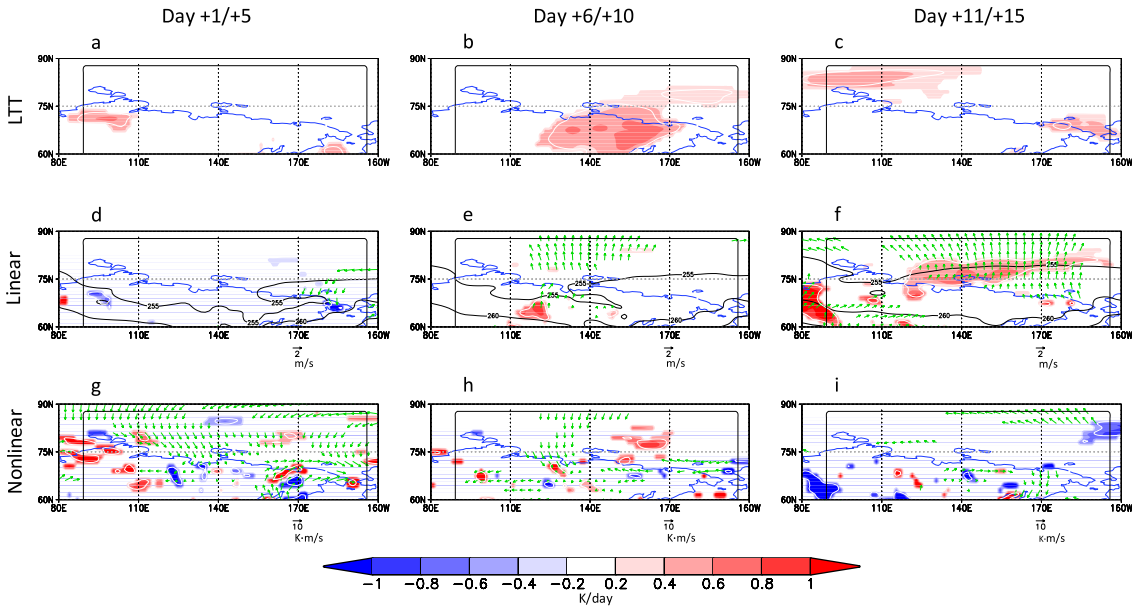

Figure 4.6: As in Figure 4.4, but for EA events.

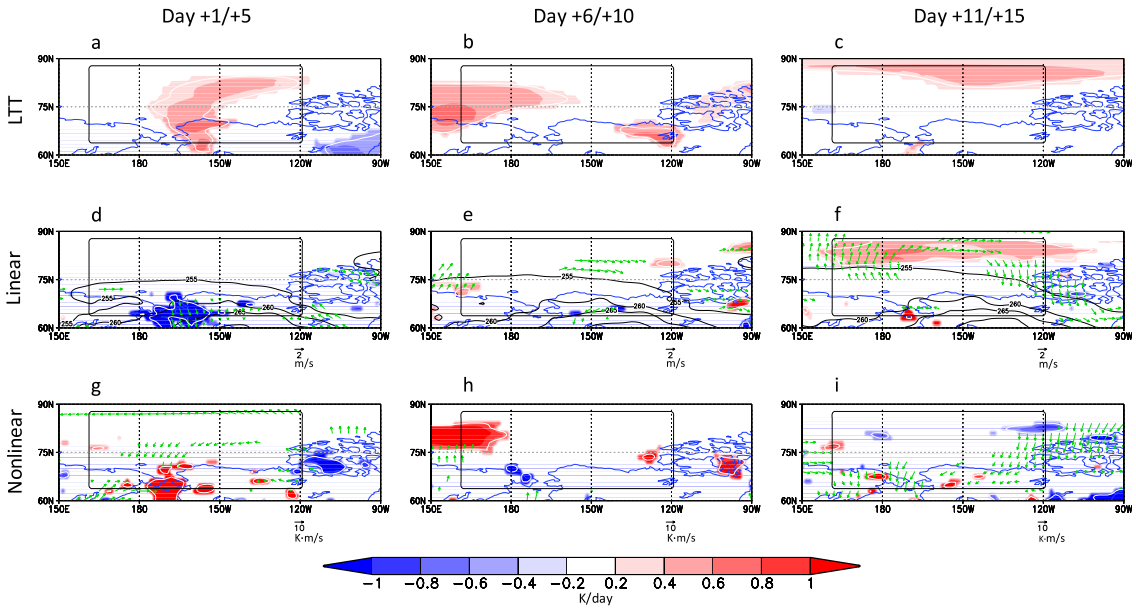

Figure 4.7: As in Figure 4.4, but for AL events.

Figure 4.7 provides the heat budget results for AL events. During the early stage of AL events, a warming signature extends from the Alaskan coast through the Chukchi Sea into the central Arctic Ocean (Fig. 4.7a). The local convergence of a southward eddy heat flux anomaly is the leading contributor to the warming signature over the Alaskan coast, the Bering Strait, and southern Chukchi Sea (Fig. 4.7g). However, this nonlinear contribution is partially offset by cooling due to linear temperature advection, resulting in a relatively weak net warming pattern. During the middle stage, the warming signal in Fig. 4.7b splits into two centers; one over the East Siberian Sea and another over northeast Alaska and the Queen Elizabeth Islands. The Siberian signature is mainly due to the convergence of an anomalous northward eddy heat flux signature combined with a weaker contribution from linear advection (Figs. 4.7e and 4.7h). Warming to the east is due to anomalous eddy heat flux convergence over the Alaskan region and linear advection over Beaufort Sea. During the late stage, there is a significant warming pattern further north over the central Arctic Ocean, where linear advection provides the primary source (Fig. 4.7f).

4.4.2 Areal_Average Time Evolution

Figure 4.8 displays areal-averaged time series of the daily temperature tendencies due to the various dynamical and physical forcing terms in Eq. (7), thereby summarizing the primary source terms in a domain-average sense. Supplementary spatial maps related to some of the adiabatic and diabatic source terms are also included in Figs. 4.9-4.12, for completeness.

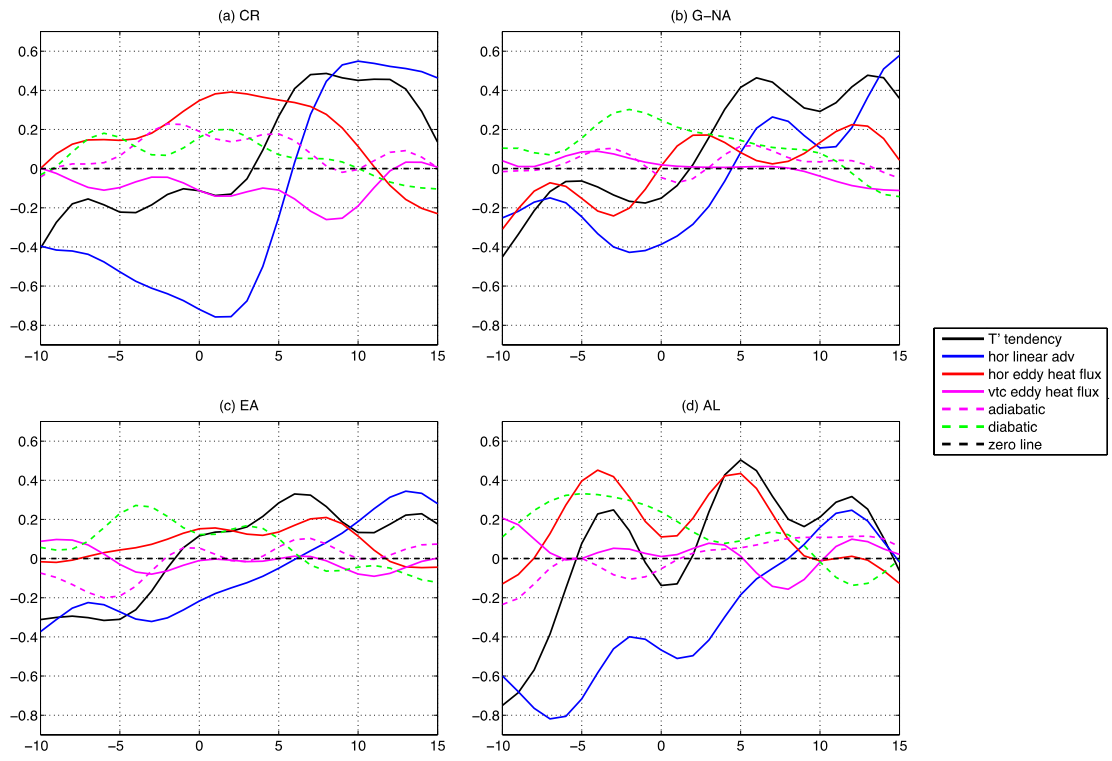

Figure 4.8: Composite time evolution from day -10 to day +15 of daily areal-average contributions (unit: K/day) of the forcing terms in Eq. (7).

For CR events, the nonlinear term (related to anomalous eddy heat flux convergence) contributes most prominently to warming during the early stages of the evolution from day 0 until about day +10. A leading positive contribution of linear temperature advection to warming begins around day +5 and then dominates the warming at later stages, consistent with the map analyses presented in Fig. 4.4. During day +1 to day +10, apart from the dynamically-related linear and nonlinear contributions, anomalous

adiabatic processes make a smaller contribution (about half the magnitude of the leading term) to the temperature increase. Spatial maps of this term are provided in Fig. 4.9. During the early stage, adiabatic warming is observed within the same region as anomalous horizontal eddy heat convergence (Fig. 4.4g). Thereafter (middle stage), the anomalous adiabatic heating signature (Fig. 4.9b) closely coincides with the regional warming due to linear temperature advection (Fig. 4.4e). Although positive contributions from anomalous diabatic heating are also observed during this time, they have weak amplitudes and limited areal extent.

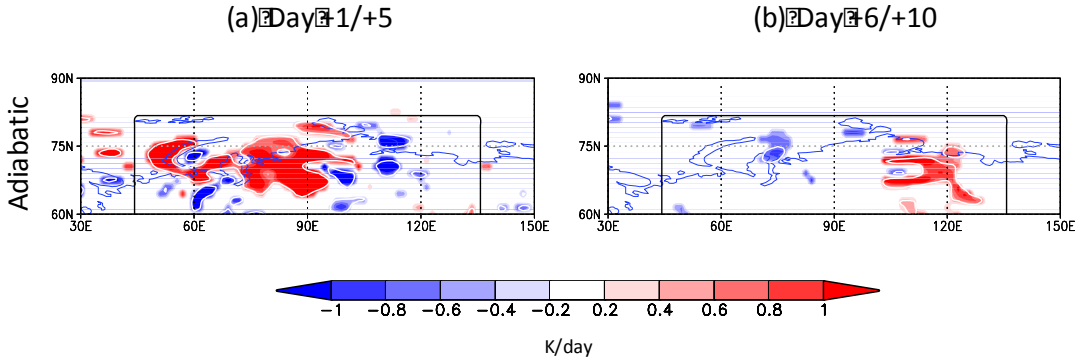

Figure 4.9: Composite structures of the adiabatic contribution (unit: K/day) during (a) days +1/+5 and (b) days +6/+10 for CR events. Only values at the 0.90 significance level are shaded; the 0.95 significance level is plotted as a white contour.

For G-NA events, the nonlinear (eddy heat flux) contribution is relatively small during spring onset, which is not surprising given the sparse small-scale features noted in Fig. 4.5. During the early stage, the time series analysis suggests a potential role from anomalous diabatic heating. Figure 4.10 displays the spatial structure of diabatic heating during the early and middle stages of G-NA events. During the early stage, although limited in areal coverage, the most prominent diabatic heating anomalies are over the northern domain edge (Fig. 4.10a) where anomalous northerly wind advects relatively warm air from the ocean (Fig. 4.5d). Thereafter, this diabatic signature weakens (Fig. 4.10b) so that, by the middle stage, the pattern consists of an incoherent pattern of weak contributions.

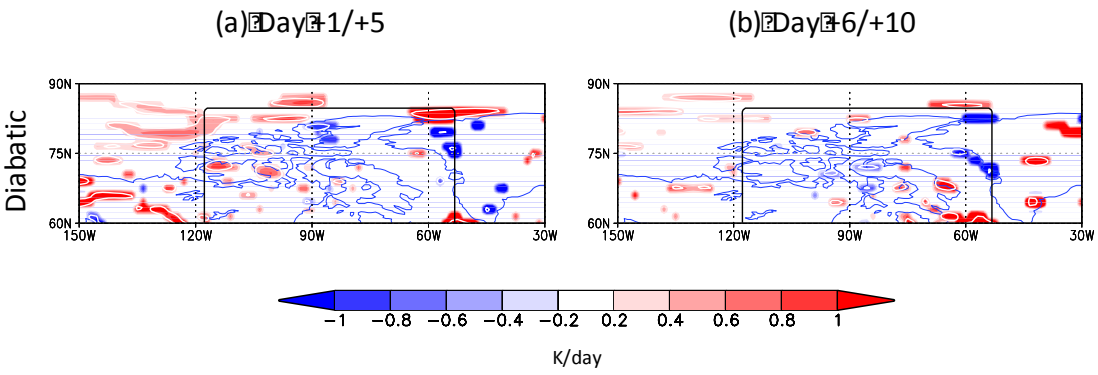

Figure 4.10: Composite structures of the diabatic contribution (unit: K/day) during (a) days +1/+5 and (b) days +6/+10 for G-NA events. Only values at the 0.90 significance level are shaded; the 0.95 significance level is plotted as a white contour.

Compared to the other regional events, EA events are characterized by relatively weak warming patterns linked to similarly weak spatial patterns in the advective forcing terms (Fig. 4.6). Although the warming patterns over the coastal region near the Barent-Kara Sea and the region from East Siberia to Bering Strait are relatively weak during the early stage (Fig. 4.6a), the areal-average results (Fig. 4.8c) indicate a coherent warming during this stage due to the combined effect of anomalous nonlinear and diabatic processes. As discussed earlier (Fig. 4.6), there are small-scale patterns of eddy heat flux convergence observed over the coastal Barent-Kara Sea, East Siberian Sea, and the Bering Strait. For the same time period, there is a weak but systematic contribution coming from anomalous diabatic heating over East Siberia (Fig. 4.11a). During the middle stage of onset, the nonlinear forcing remains dominant (Fig. 4.6i), mainly over the oceanic region, while linear advection plays a minor role over the continent, supplemented by adiabatic warming due to anomalous subsidence (Fig. 4.11b).

Prior to (before day 0 of) and during the early stages of AL events, there is a rather large positive warming contribution associated with anomalous eddy heat flux convergence (Fig. 4.7h) that is largely offset by cooling due to linear advection (Fig. 4.7d). Apart from the horizontal linear advection and eddy heat flux convergence terms, anomalous adiabatic heating provides a minor contribution between day 1 to day 10 with a similarly weak contribution from anomalous vertical eddy heat flux during day 1 to day 5. As shown in Fig. 4.12a, anomalous adiabatic heating is mainly observed over the Bering Strait and Alaskan coast where there are robust temperature increases due to nonlinear processes (Fig. 4.7g). The vertical eddy heat flux term mainly provides warming over the Chukchi Sea and

East Siberian Sea (Fig. 4.12b) where notable net warming is observed but with very little contribution from the linear, nonlinear, and adiabatic terms.

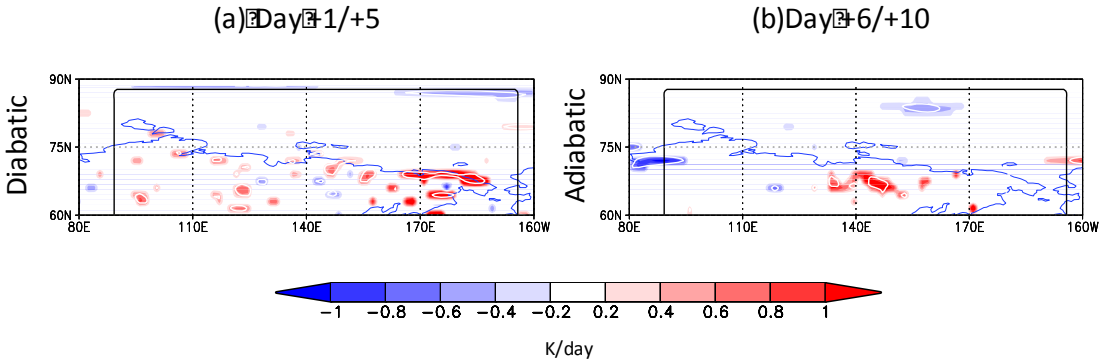

Figure 4.11: Composite structures of the (a) diabatic contribution (unit: K/day) during days +1/+5 and (b) adiabatic contribution (unit: K/day) during days +6/+10 for EA events. Only values at the 0.90 significance level are shaded; the 0.95 significance level is plotted as a white contour.

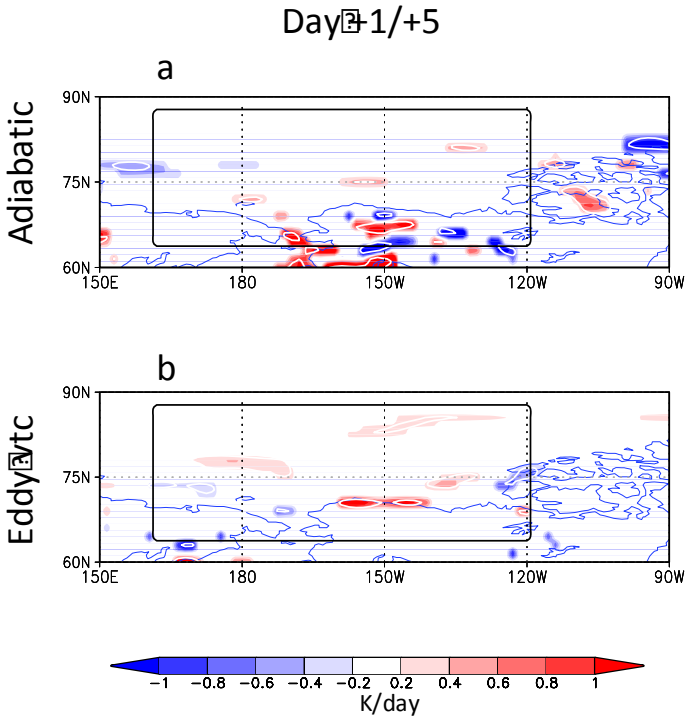

Figure 4.12: Composite structures of the (a) adiabatic contribution (unit: K/day) and (b) vertical eddy transport (unit: K/day) during days +1/+5 for AL events. Only values at the 0.90 significance level are shaded; the 0.95 significance level is plotted as a white contour.

Although the four regional event categories exhibit rather distinct differences in spatial structure, the areal-average temporal sequence of leading contributors are similar. In all four cases, the rapid temperature increase is primarily dynamically driven by linear and nonlinear horizontal heat transport. Although the most rapid temperature increase

begins around day 0, prior to onset a prominent warming contribution from nonlinear processes accompanied by diabatic heating is observed for the CR, EA, and AL events. A detailed examination of day-to-day envelope function evolution (not shown) reveals a continuous propagation of synoptic eddy activity from upstream toward the southern edge of the warming region, leading to enhanced northward eddy heat flux into along the southern boundary. The concomitant diabatic heating appears to be associated with enhanced turbulent mixing, a by-product of cyclone systems. Thus, via the combined effect of anomalous eddy heat flux and diabatic heating, the enhanced synoptic wave activity provides a leading source for the initial set-up of the rapid temperature increase during spring onset. Anomalous eddy heat flux convergence provides a coherent warming signature that leads into and then initiates the regional warming associated with spring onset. During the same time period, the contribution of linear horizontal temperature advection partially offsets the warming induced by the nonlinear term. However, later on, as the nonlinear contribution weakens in magnitude, the role of the linear temperature advection term switches to become a positive contributor, ultimately becoming the leading forcing of the regional warming signature during the later stage of events. Anomalous adiabatic and diabatic forcing both provide weaker and relatively limited impacts upon spring onset warming.

As demonstrated in Chapter 3, the rapid surface temperature increase in different regional events is closely related to changes in the large-scale atmospheric circulation. More specifically, alterations in the strength and spatial structures of the semi-permanent surface pressure systems lead to favorable conditions for anomalous heat transport, especially advection of climatological temperature by the anomalous wind field. Such an

evolution of synoptic circulation patterns can lead to changes in horizontal advection, via the linear term, in the heat budget analysis. A dramatic increase in the linear advective contribution occurs concomitantly with an increase in the temperature tendency, itself, immediately after the transition (Fig. 4.8). When the temperature tendency maintains high values during the middle stages of onset, the large-scale circulation transition is complete and the primary contribution continues to be the linear temperature advection

4.5 Synoptic Diagnostics

As shown in Fig. 4.8, the time scale for the warming associated with spring onset events is roughly 2 weeks, same as discussed in Chapter 2. Events occurring on such time scales are most likely driven by dynamical processes and this is quantitatively verified in the current study as the regional warming patterns associated with spring onset events arise primarily in response to anomalous (nonlinear) eddy heat transport and the linear advection of the climatological temperature field by composite wind anomaly field. In this section, supplementary composite synoptic analyses are reviewed to gain additional insight into the physical mechanisms leading to the large-scale dynamical forcing of regional warming signatures. We first consider the nonlinear forcing term.

For all four regional event categories, anomalous eddy heat flux convergence provides rapid temperature increases during the early stage – usually beginning prior to event onset and continuing toward day +10. We further analyze the eddy heat flux convergence at 925hPa and the 500 hPa geopotential envelope function (hgt500) to better understand this eddy behavior. The climatological-mean distributions of eddy heat flux and envelope function are plotted in Fig. 4.13. Three local maxima in synoptic eddy activity are observed in Fig. 4.13a: The two strongest maxima represent the northern portions of

the North Pacific and North Atlantic storm tracks. The third weaker maximum corresponds to a local continental region of baroclinic eddy activity. The regional maps of climatological eddy heat flux (Figs. 4.13b-4.13e) illustrate that all four regions are typically characterized by a northward eddy heat flux that gradually weakens to the north (providing a broad swath of heating over high latitudes). As we will show later, a common feature among all four regional event categories is the systematic weakening of eddy activity within the interior of the region of interest, leading to a reduction in northward heat flux (compared to climatology) over the northern reaches of the domain and a strong anomalous accumulation of heat within the region.

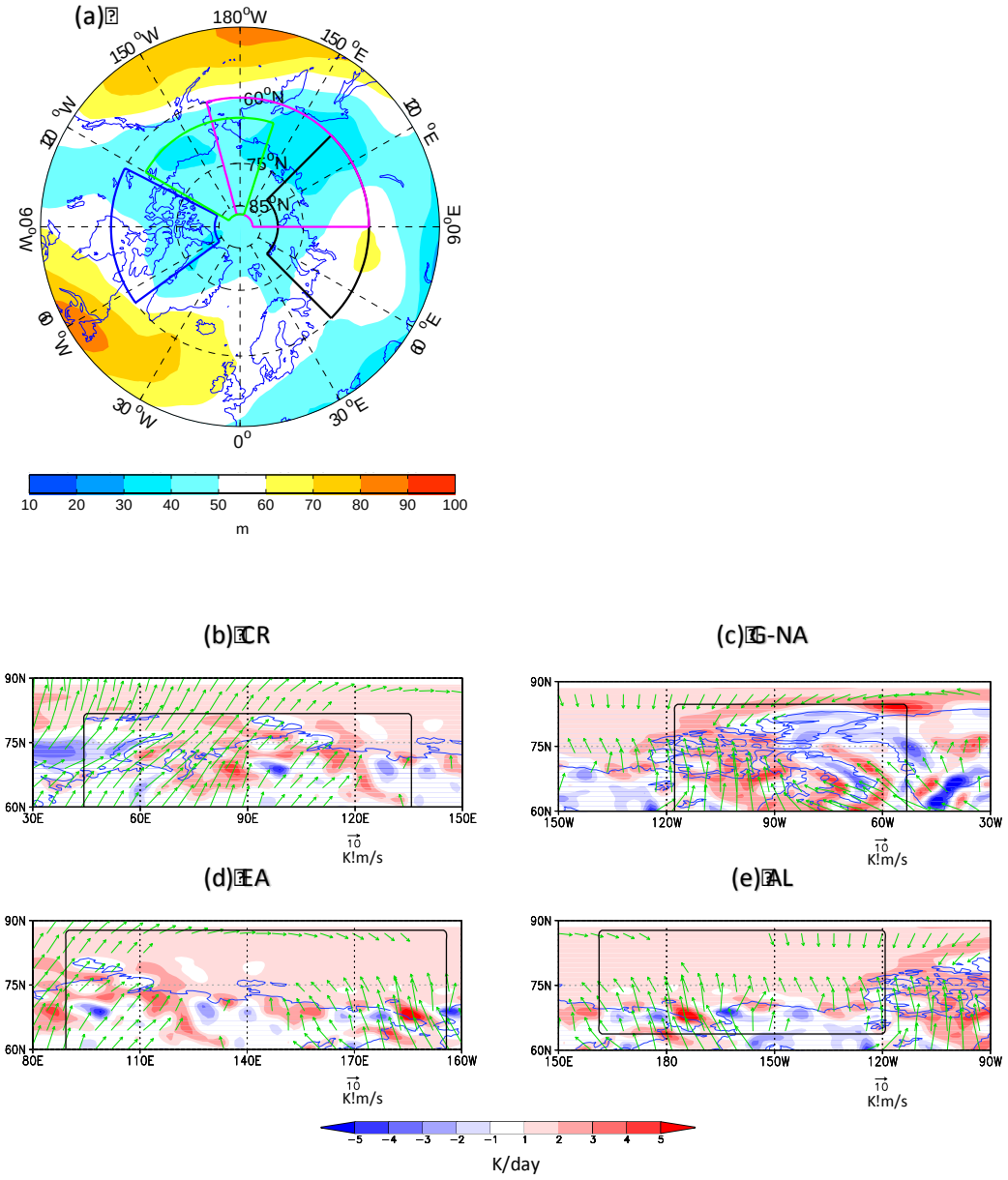

Figure 4.13: (a) Climatology of the envelope function (unit: m) with the 4 regions outlined in black for CR, magenta for EA, green for AL, and blue for G-NA. (b-e) Climatology of eddy heat flux (vectors, unit: K•m/s) and its convergence (shading, unit: K/day).

The CR region lies on the north side of the continental eddy activity maxima discussed above, and is associated with a strong northeastward climatological eddy heat flux (Fig. 4.13b). During day +1 to day +10 of CR events, anomalous eddy heat flux convergence provides warming over most of the CR region, with northward heat flux anomalies along the southern boundary and southward heat flux anomalies to the north (Figs. 4.4h and 4.4i). These heat flux anomalies enhance the background climatological northward heat flux to the south and reduce it to the north, leading to an anomalous accumulation of heat within the critical region. Figure 4.14 provides maps of the composite envelope function anomaly during the pre-onset (days -4 to 0), early (days +1 to +5) and middle stages (days +6 to +10) of CR events. Prior to day 0, a weak positive anomaly appears along the southern edge of the domain while the interior of the critical region exhibits negative anomalies, indicating enhanced baroclinic wave activity to the south with reduced activity over the central and northern parts of the critical region. After day 0, the southern positive anomaly shifts northeastward into the southeastern corner of the critical region while another positive anomaly center emerges just outside the southwestern domain edge and is linked to northward heat flux anomalies (Fig. 4.4h). Meanwhile, the region of negative baroclinic eddy activity expands eastward to cover the central portion of the critical region where reduced northward heat flux and anomalous heat flux convergence is observed.

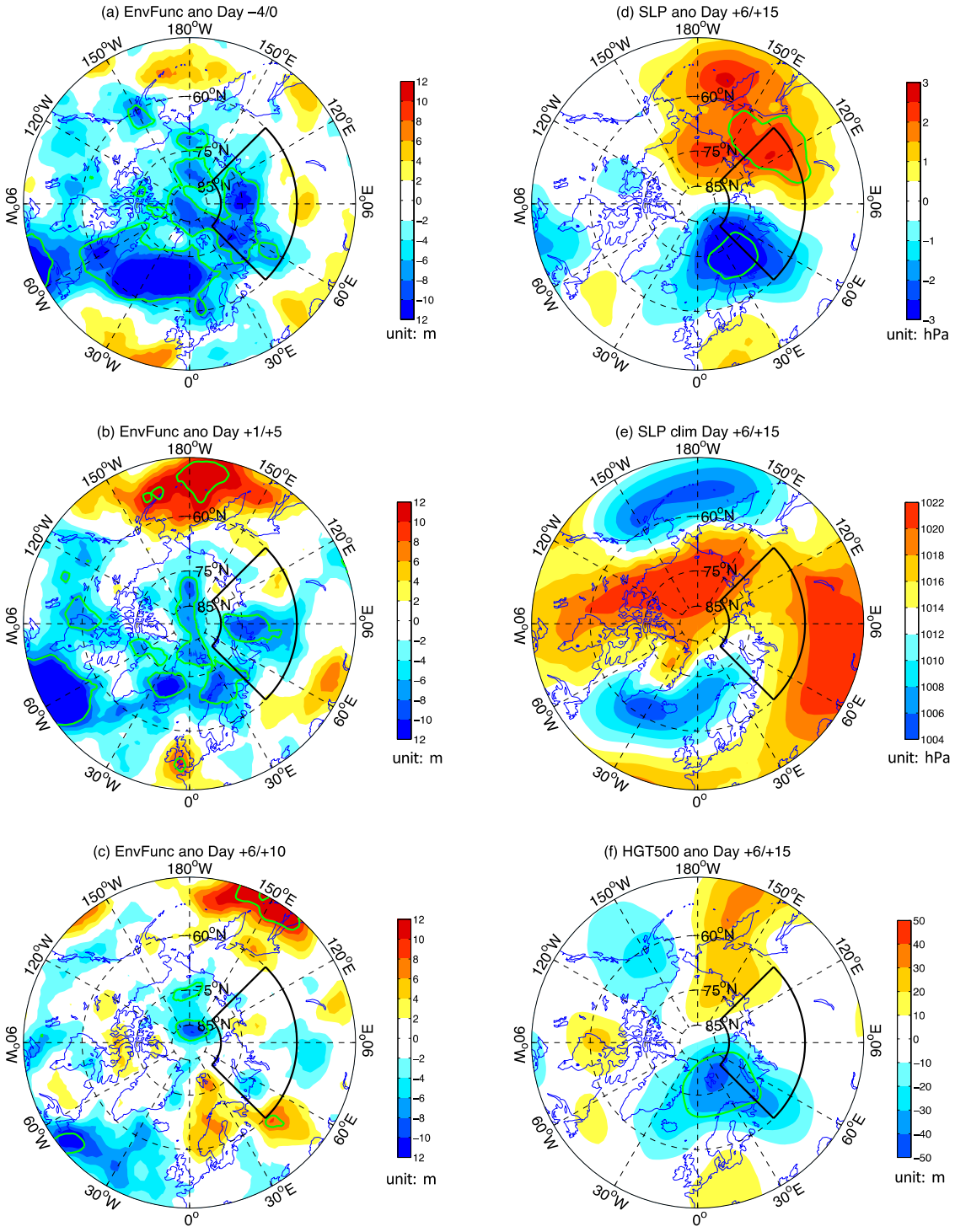

Figure 4.14: (a-c) Composite evolution of envelope function anomalies (unit: m) for CR events. (d-f) Composite-mean structures of SLP anomalies (d, unit: hPa), SLP climatology (e, unit: hPa), and 500 hPa geopotential height anomaly (f, unit: m). The 0.95 significance level is plotted as a green contour.

The G-NA sector lies to the north of North Atlantic storm track entrance region (Fig. 4.13a), where synoptic wave generation commonly occurs. The climatological heat flux pattern for G-NA (Fig. 4.13c) includes strong northward and northwestward eddy heat fluxes extending northward from the southernmost portion of the domain along with weak southward directed eddy heat fluxes observed along the northern edge. The largest eddy heat flux magnitudes are found over the Davis Strait. The envelope function analyses indicate weak suppression of eddy activity during the early stage of G-NA events followed by a weak enhancement during the late stage (Fig. 4.15). In terms of the heat budget, at the early stage, the contribution of anomalous nonlinear forcing to G-NA warming is limited (less than half of the magnitude of temperature anomaly tendency as in Fig. 4.8). After day +10, a relatively stronger positive nonlinear contribution emerges in association with enhanced eddy activity in the southeast corner of the G-NA (Fig. 4.15) region and an anomalous strengthening of the northwestward eddy heat flux over the Davis Strait (Fig. 4.5).

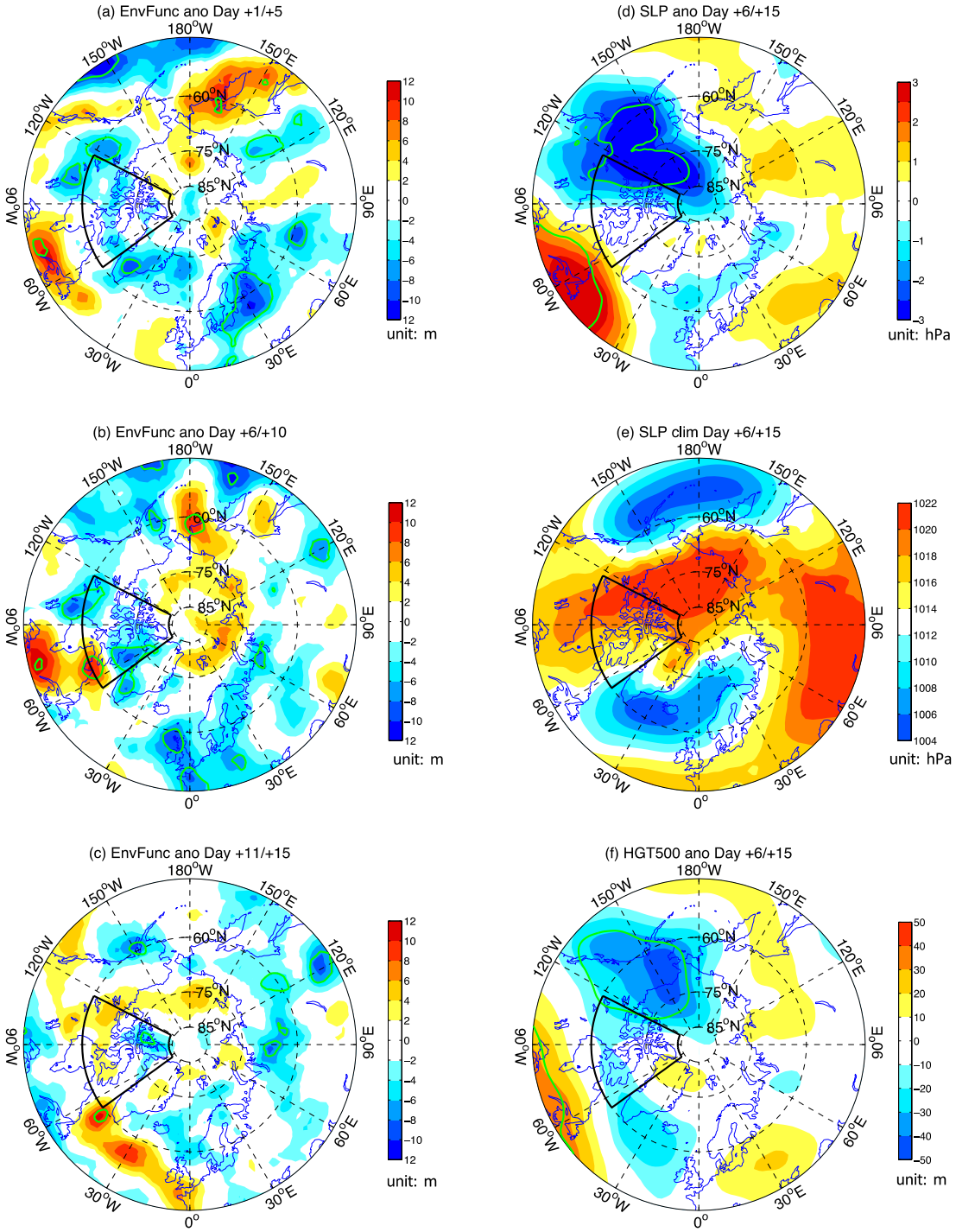

Figure 4.15: As in Fig. 4.14, but for G-NA events. As shown in Fig. 4.8, the nonlinear contribution initiates at around day 0 during G-NA spring onset (in contrast to the other regional events when nonlinear contribution initiates prior to the events), thus the envelope function anomalies are shown at Days +1/+5, +6/+10, and +11/+15, unlike for the other three categories.

From a climatological perspective, the EA sector is characterized by weak northward eddy heat fluxes that decrease in magnitude toward the Pole (Fig. 4.13d). Along the northern domain edge, the eddy heat flux becomes more zonally (eastward) oriented and rotates further to include a southward meridional component in the northeastern corner. An anomalous southward heat flux dominates a large portion of the oceanic region during the early and middle stages (Fig. 4.6), in association with a large region of suppressed eddy activity (negative anomalies in the envelope function; Figs. 4.16a and 4.16b). Since the EA sector is not very close to either storm track region, there is little influence from either. The key signature is reduced eddy activity within the region itself.

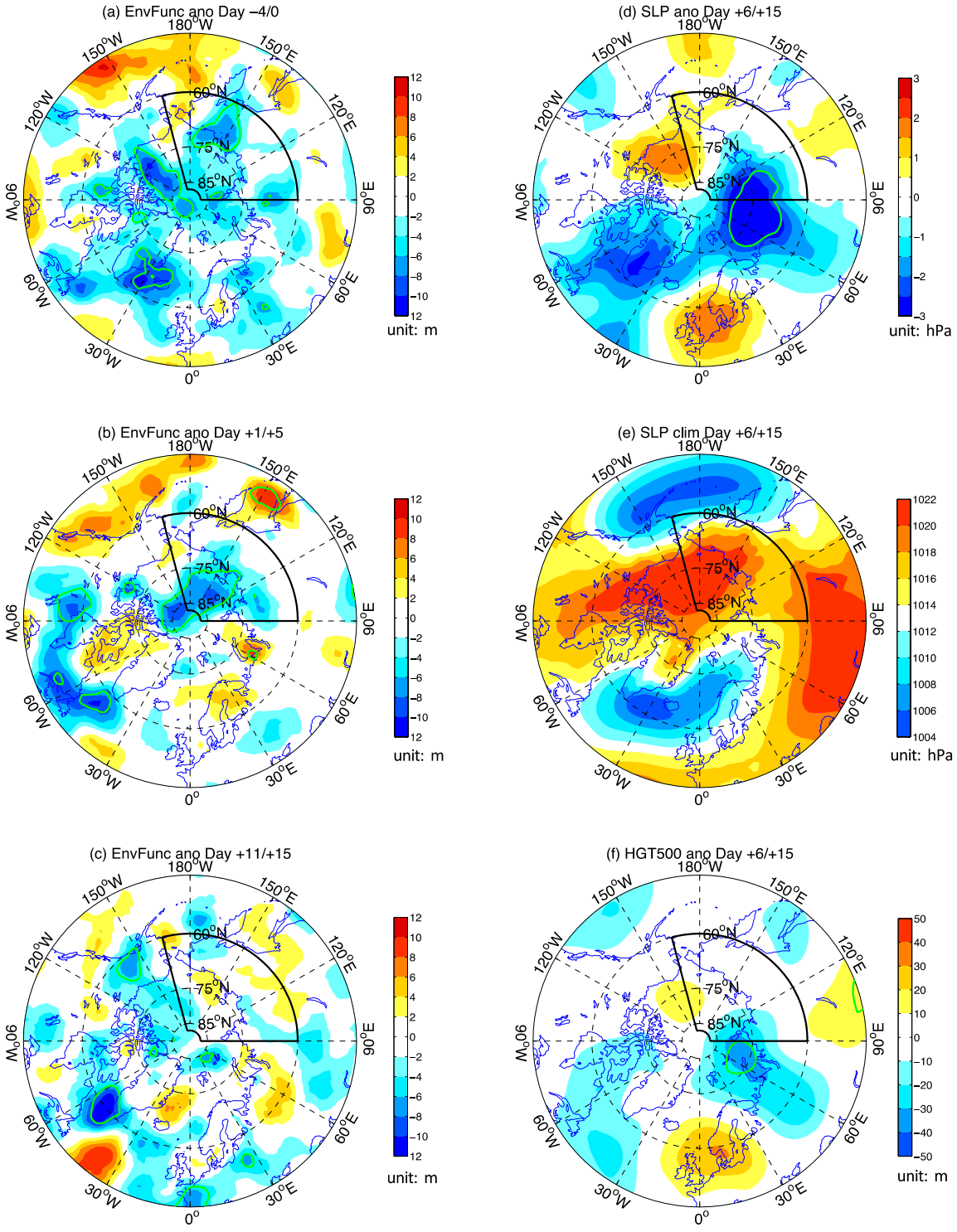

Figure 4.16: As in Fig. 4.14, but for EA events.

Although the AL region is also distinct from the primary storm tracks, it lies north of the Bering Strait, a pathway through which some North Pacific storms travel into the Arctic leading to robust climatological-mean heat flux convergence (Fig. 4.13e). A strong northward heat flux is observed in the region surrounding the Bering strait. Prior to onset, eddy activity is suppressed over the central Arctic Ocean and Beaufort Sea and enhanced to the south of the Bering Sea (Fig. 4.17a). Although both features weaken thereafter, they still result in an anomalous southward eddy heat flux over the central AL domain, leading to an anomalous eddy heat flux convergence over the Bering Strait (Fig. 4.7g). After day +5, enhanced eddy activity develops over the Beaufort Sea and this positive anomaly feature extends upstream through the Chukchi Sea into the East Siberian Sea. Meanwhile, a northward heat flux anomaly leading to eddy heat flux convergence is observed over the East Siberian Sea, along the western edge of the AL region (Fig. 4.7h).

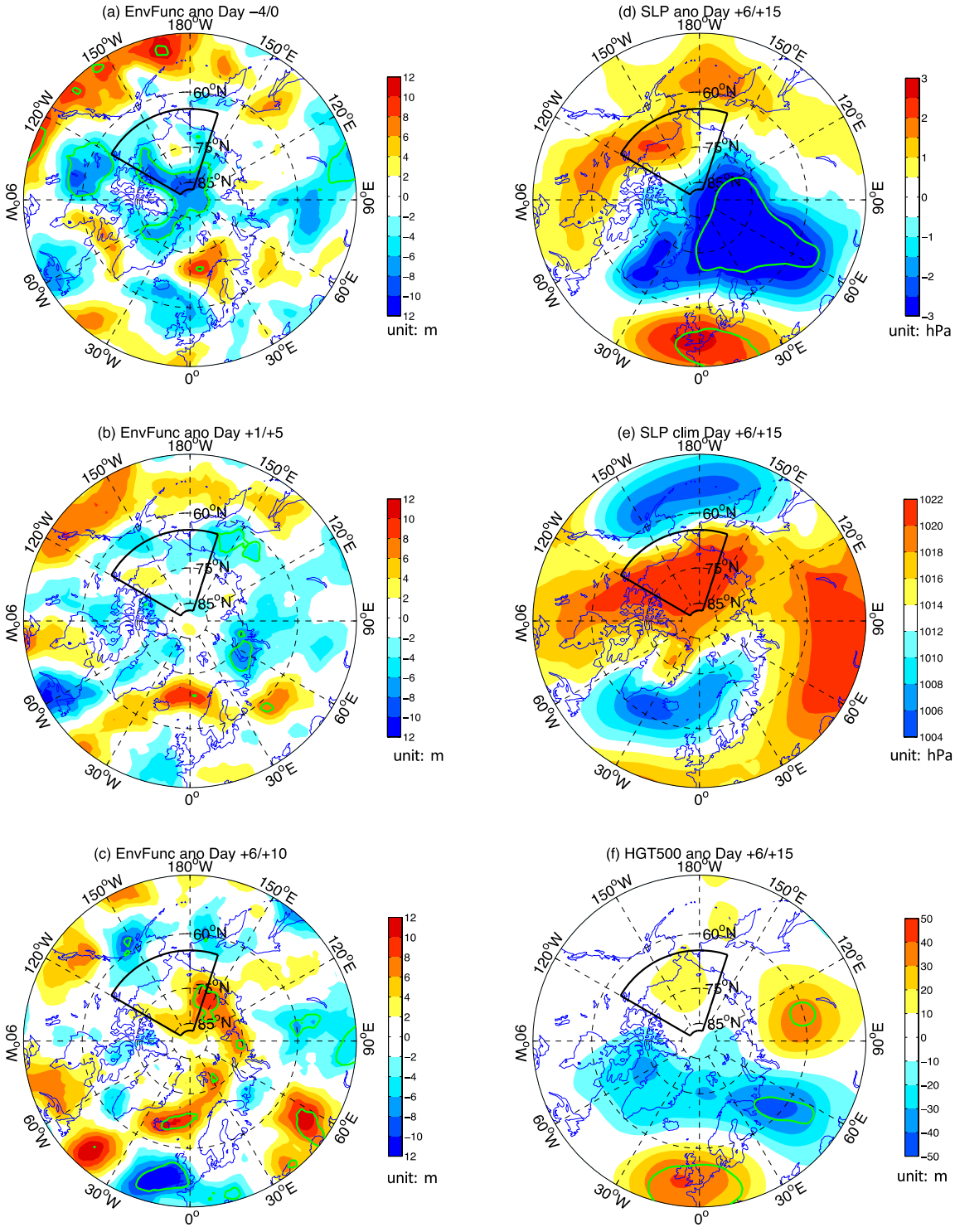

Figure 4.17: As in Fig. 4.14, but for AL events.

By studying composite sea level pressure changes during spring onset, synoptic analysis in Chapter 3 deduces an important role for heat transport by the large-scale flow near the Earth's surface, especially in relation to changes in semi-permanent pressure systems. The current heat budget analysis reveals that linear advection, mainly advection of climatological temperature by the anomalous wind field, is a primary contributor to regional warming during the later stages of spring onset. The right columns of Figs. 4.14-4.17 display components of the composite circulation anomaly field averaged from day +6 to day +15, the time period during which linear temperature advection provides a sustained contribution. We note that common to CR, G-NA, and EA events there is a negative SLP anomaly center located in the western portion of the region that transitions to weak positive anomalies downstream to the east. Such a pattern is associated with a broad swath of anomalous southerly wind, leading to the linear warm advection diagnosed using Eq. (7).

As discussed in Chapter 3, for CR cases, the broad low pressure anomaly center extending from the Barent Sea through the Kara Sea into the Laptev Sea, is a result of the strengthening and northeastward intrusion of the semi-permanent Icelandic low. The anomalous high pressure center located over eastern Russia and East Siberian Sea is related to a northeastward shift of the Siberian High and a strengthening of the Polar High. These two SLP anomaly centers generate a pathway for southerly wind anomalies as shown in Figs. 4.14d-4.14f. For the G-NA sector, a large low pressure anomaly feature in the western portion of the domain covers Alaska, North Canada and the Beaufort Sea (Figs. 4.15d-4.15f). Superposed with the climatological-mean fields, this corresponds to an intrusion of Aleutian Low into the North American continent along with a weakening of continental high pressure over North America. A significant southerly wind anomaly

pattern is observed along the eastern edge of the low pressure anomaly feature (Fig. 4.5f). For EA events, the low pressure anomaly feature is over northern Siberia and the ocean to its north (Figs. 4.16d-4.16f), consistent with the observation of a weakened Siberian High (as in Chapter 3). An anomalous high pressure center is found over the Beaufort region, implying an enhanced Beaufort High. The region between the weakened Siberian High and strengthened Beaufort High is characterized by robust southerly wind anomalies (Figs. 4.6e-4.6f).

In contrast to the three regional events discussed above, AL events don't exhibit an anomalous low pressure center over the western AL domain; instead, a robust anomalous low pressure center is located to the northwest of the domain over the Barent-Kara Sea together with a weaker positive anomaly center to the southeast (Fig. 4.17d). This northwest-southeast anomaly dipole in sea level pressure forms a pathway for geostrophic southwesterly flow emanating from the Bering Strait, but providing only a weak contribution at higher latitudes. Consistent with this weak anomaly structure, we note the modest and spatially limited contribution of linear temperature advection to AL event onset (Figs. 4.7e-4.7f) compared to the other three event categories.

4.6 Summary

This chapter applies the RoC method introduced in Chapter 2 to regional surface air temperature and identifies four categories of Arctic spring onset events over the following regions: The primary (critical) region over North Siberia (CR), Greenland-North America (G-NA), East Asia (EA), and Alaska (AL). Local tendencies in near-surface air temperature anomaly are decomposed into separate dynamic and thermodynamic contributions using a heat budget analysis. The spatial and temporal structures of these

dynamic and thermodynamic processes and their relative contributions to the overall changes in temperature anomalies are investigated.

A common feature discovered among all four event categories is the leading role of eddy heat flux convergence and linear horizontal temperature advection in creating rapid temperature increases during Arctic spring onset. The nonlinear dynamical contribution of baroclinic eddies is found to provide a leading positive contribution that begins prior to regional spring onset and lasts until about 10 days after the onset. Anomalous baroclinic wave activity, linked to regional storm track variability, alters the eddy heat flux patterns, resulting in anomalous heat flux convergence. Horizontal linear advection of the climatological temperature field by the anomalous large-scale circulation contributes to warming at later stages, usually about 5 days after event onset when the role of eddy heat fluxes diminishes. Concurrent composite analysis of SLP anomalies shows a dipole structure with anomalous low (high) pressure to the west (east), providing anomalous southerly geostrophic flow during the later stages of CR, G-NA, and EA events (leading to linear warm advection). For AL events, however, linear advection only contributes at a very late stage (after day +10) in the evolution with a limited magnitude; no significant SLP signature is observed within the Alaskan region during AL. Regional temperature anomaly changes associated with vertical motion (both adiabatic heating and vertical transport) and diabatic processes are found to play only minor roles with weak magnitudes and limited spatial and temporal extent. In the CR and AL categories the adiabatic warming contribution occurs simultaneously with large-scale linear advective cooling, indicating a systematic large-scale sinking associated with cold advection. The minor contribution from diabatic processes principally occurs prior to spring onset when the nonlinear heat flux

from synoptic eddies dominates. A parallel analysis (based upon MERRA; not shown) of temperature tendency induced by friction, radiative forcing, moist process, and turbulent mixing, respectively, suggests that the residual warming occurring prior to spring onset is related to turbulent mixing, which itself is a by-product of enhancements in synoptic eddy activity. The residual warming after spring onset is mainly due to radiative processes. Studies on decadal time-scale temperature trends suggests that enhanced downward infrared radiation is a likely consequence of strengthened meridional heat transport, latent heat release, and increased cloudiness (Flournoy et al. 2016), which could be a potential contributing factor for spring onset warming.

The composite analysis as presented in Chapters 2 through 4 have increased our knowledge of rapid T2m increase during ASO events, including formulating an effective method for identifying ASO events, characterizing the temporal and spatial evolutions of synoptic structures during ASO events, and assessing the leading dynamical processes contributing to different stages of ASO events. In the following chapter, we will perform a case study of the CR event in 2000 using both observational data and model simulations.

CHAPTER 5: A CASE STUDY OF THE 2000 CR EVENT

5.1 Introduction

In analyzing the synoptic behaviors of, and studying the heat budget contributions toward, Arctic spring onset (ASO), we have largely focused on the composite analysis of observational data, an effective tool for isolating the average/common features within the life cycle of an event category. Composite maps of T2m changes and SLP evolution provide the spatial structure of ASO events and the associated synoptic conditions that impact regional temperature advection. A diagnostic heat budget assessment during ASO events identifies the dominant contribution to regional warming is nonlinear eddy heat transport prior to and during the early ASO stages while the leading contribution during the late stages of events comes from linear temperature advection.

In this chapter, we explore the CR ASO event occurring in 2000 (CASE2000) that is selected based on its resemblance to the canonical (composite) behavior of CR events, making it a representative case for further investigations of the dynamical mechanisms for ASO. In this chapter, the fundamental features of CASE2000 and a comparison to the composite behavior illustrated in previous chapters are first provided. Then, numerical model experiments are performed using the Weather Research and Forecasting Model to investigate the influential role of synoptic eddies on the timing of ASO events and the magnitude of T2m increases during events.

5.2 Observed Characteristics of CASE2000

As discussed in Chapter 2, ASO timing exhibits strong interannual variability and thus ASO events can be classified into early and late categories based on the onset dates.

Regional ASO events also demonstrate considerable interannual variability. CASE 2000 occurs on February 25th and is denoted as an early event, that actually occurs three days' earlier than the average date of early CR events (February 28th).

Time series plots of the daily T2m and T2m tendency are shown in Fig. 5.1, along with the CASE2000 onset date. The daily T2m averaged over the CR region contains sizable high frequency variability (blue line) and is used for the 2-phase linear regression model to detect the optimal transition from a steady winter state to the warming spring state. The 2-phase linear regression method identifies March 3rd as the optimal separation between 1999/2000 winter and 2000 spring. The corresponding smoothed daily T2m (via a 30-day low-pass filter; black line), which is used as the input into the RoC method to identify the CASE2000 onset date February 25th is also display. The local minimum in the unfiltered T2m (a "valley" between February 26th to 28th) lies in between the onset dates identified from the two methods. The temperature tendencies of unfiltered and smoothed T2m, respectively, are provided in Fig. 5.1b, along with the RoC identified CR onset date. The tendency derived from the smoothed T2m time series shows a gradual shift from negative to positive, illustrating the set-up of the warming process. This transition occurs 2 days later in the unfiltered T2m time series with an even sharper slope in the T2m change. In both cases, the tendency falls back below zero in roughly two weeks. The following analysis focuses on the short period of sustained T2m increase observed after the local T2m minimum.

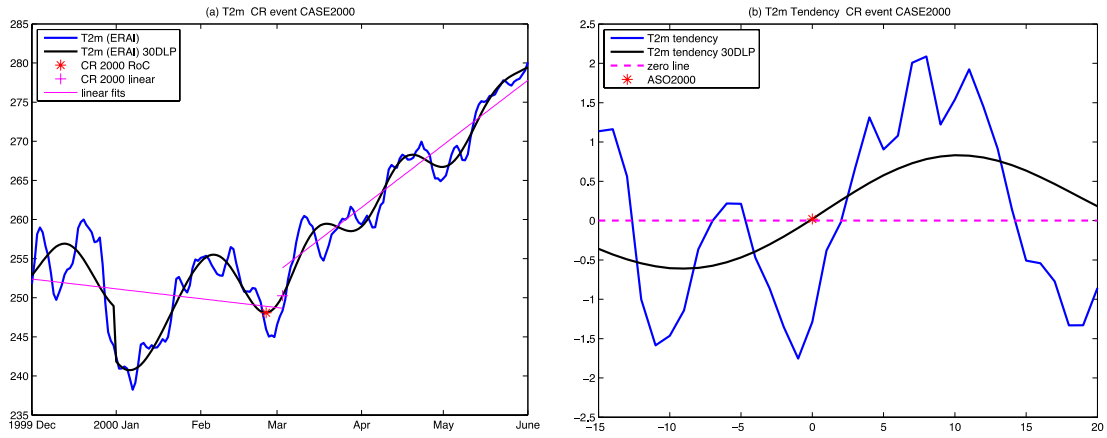

Figure 5.1: (a) T2m (unit: K) unfiltered (30-day low-passed) data in blue (black) solid line; linear fits of the winter and spring T2m states from the 2-phase linear model in magenta solid line; CASE2000 onset date via RoC (linear regression model) in red star (magenta cross). (b) Daily tendency of T2m (unit: K/day) unfiltered (30-day low-passed) data in blue (black) solid line; zero values in magenta dashed line; CASE2000 onset date via RoC in red star.

Figure 5.2 provides spatial maps of the T2m/T925 changes occurring between day +1 to day +14 during CASE2000. Robust warming signatures are clearly evident over the CR region. Although most of the region is covered by the warming pattern, the strongest surface temperature increase occurs over the western portions of the region (Fig. 5.1a) while the warming center shifts eastward at the 925 hPa level (Fig. 5.1b). Temperature changes for CASE2000 are much notably larger in magnitude compared to the composite

T2m changes for CR events (Figs. 4.1a and 4.3a), which is likely due to the implicit temporal and spatial smoothing that occurs in the creation of composite fields.

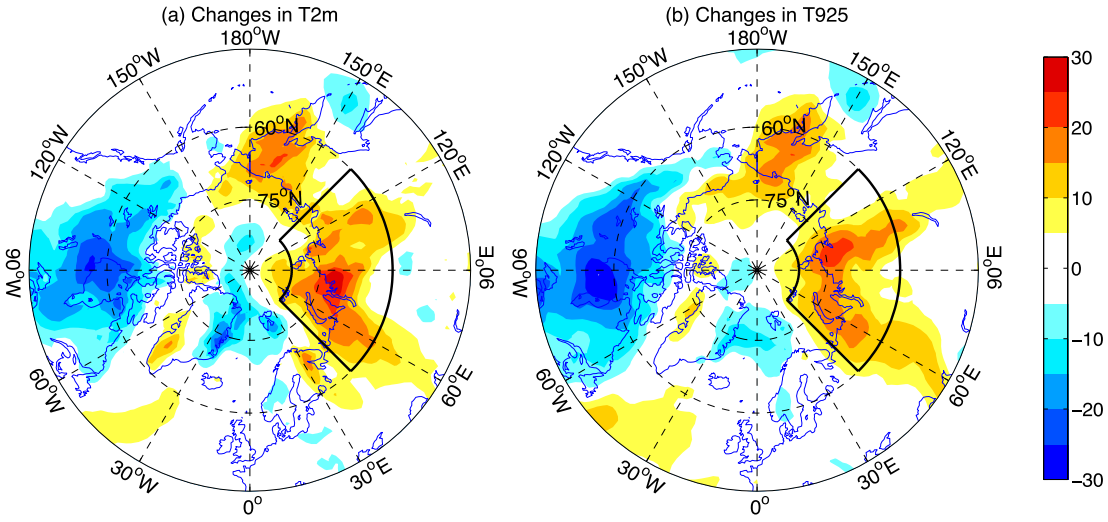

Figure 5.2: Changes in (a) T2m anomaly and (b) T925 anomaly (unit: K) between February 26th and March 1st.

A heat budget analysis is also applied to assess the contributors to temperature increases for CASE2000. Figure 5.3 shows the areal-average evolution of temperature tendency due to different physical processes based upon Eq. (7). Compared with the composite evolution of CR events, the nonlinear contribution initiates relatively late, however, it remains the primary driver for the early stage. The linear advection takes over as the leading process during the middle stage while the nonlinear contribution gradually diminishes. During the late stage, as the linear advection wanes, the temperature tendency also decreases dramatically. Envelope function anomalies during day -2 to day +2 (when nonlinear processes initiate rapid warming) are shown in Fig. 5.4a. A coherent negative envelope function feature is observed within the northern portion of critical region with a prominent positive anomaly center located over the southwest corner, indicating reduced synoptic eddy to the north and enhanced eddy to the southwest. Such a distribution of anomalous eddy activity results in an increased northward eddy heat flux into the region (along the southwest boundary) and decreased eddy heat flux towards the pole, leading to eddy heat convergence within the CR region. A similar mechanism has been shown to be a common feature in the composite analysis of CR events (Figs. 4.14a and 4.14b). A composite map of the SLP anomaly field averaged over days +7 to +9 is shown in Fig. 5.4b. During the middle stage, an SLP anomaly dipole is observed, with low pressure over the southwest and high pressure over the northeast. This pattern provides a favorable synoptic environment for producing anomalous warm advection into the critical region from the southeast. In contrast to the composite structure of CR events (Fig. 4.14d and 4.14f), this dipole anomaly persists for a shorter period in CASE2000 and exhibits a tilt

into southwest-northeast direction versus the east-west dipole structure found in the CR composite analysis.

Despite of the noted differences in the synoptic behavior and heat budget analyses of CASE2000 compared to the composite results, CASE2000 shows a very similar set of dynamical driving processes — A primary contribution from nonlinear heat transport in initiating the rapid warming process and leading into the early stage of the event followed by an associated modification to the large-scale circulation leading to the advent of large-scale linear warm advection during the middle stage. In the following Section 5.3, results from numerical model experiments based on the Weather Research and Forecasting model are presented to isolate the synoptic eddy activity and study its contribution to CASE2000.

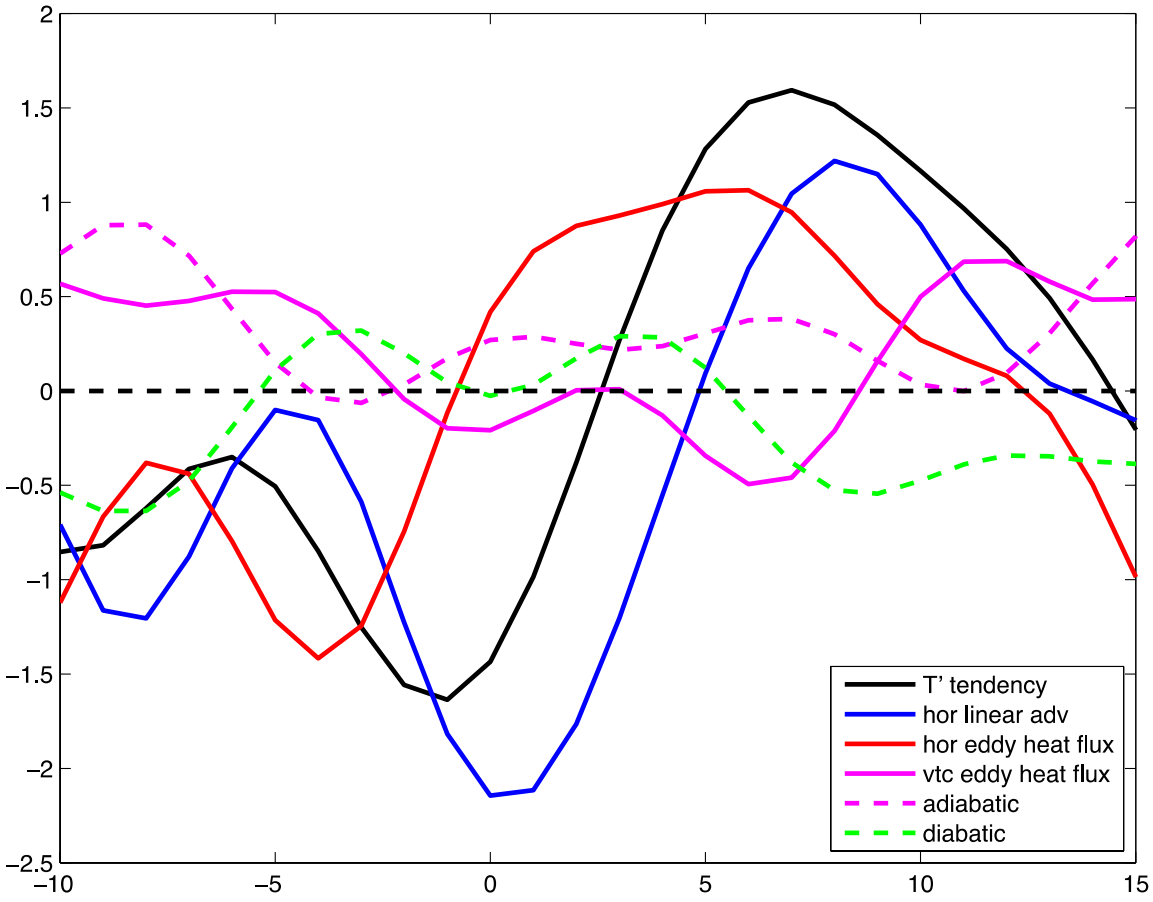

Figure 5.3: Time evolution from day -10 to day +15 of daily areal-average contributions (unit: K/day) of the forcing terms for CASE2000 in Eq. (7).

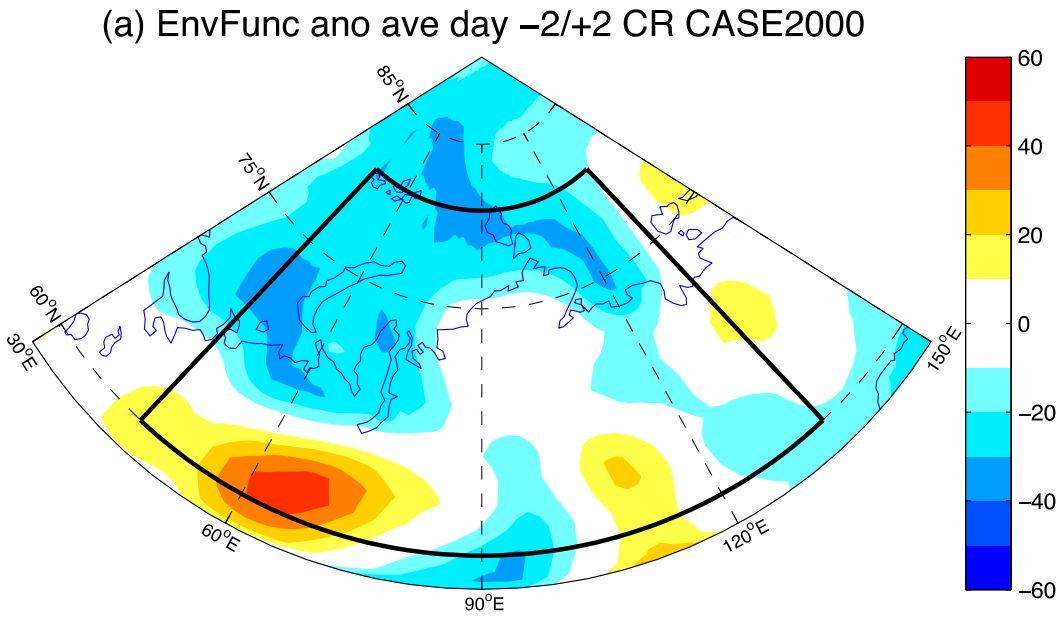

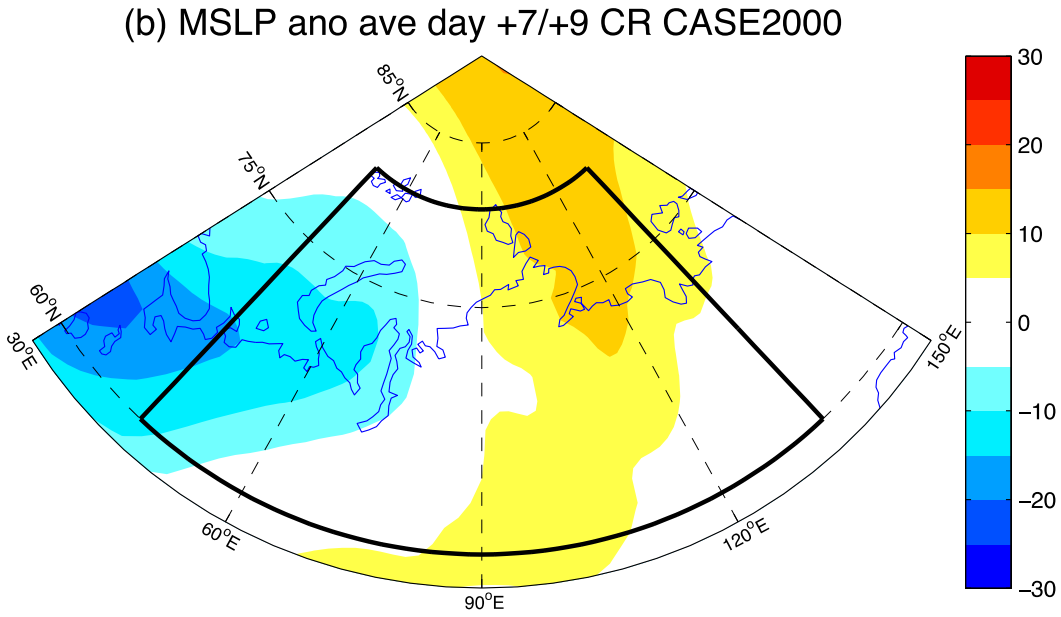

Figure 5.4: (a) Anomaly of envelope function (unit: m) averaged between day -2 and day +2 of CASE2000. (b) Anomaly of SLP (hPa) averaged between day +7/+9 of CASE2000.

5.3 WRF Simulations of CASE2000 CR Event

5.3.1 Model Configurations for Simulations over the Arctic

The Arctic region is very sensitive to changes in the Earth climate system. Despite the challenges in simulating the Arctic system, numerical models have been widely used to study the response of Arctic atmosphere to a changing global climate, particularly in relation to sea ice variability (e.g., Deser et al. 2007; Deser et al. 2010; Gerdes 2006; Handorf et al. 2015; Screen et al. 2013; Singarayer et al. 2006). The Polar Meteorology Group of Byrd Polar Research Center at the Ohio State University has made progress in developing the Polar WRF (http://www.polarmet.osu.edu/PWRF/) by implementing a set of polar optimizations of boundary layer processes, cloud physics, and sea ice treatment over the Arctic regions, including the Greenland ice sheet (Hines and Bromwich 2008), Arctic Ocean (Bromwich et al 2009), and Arctic land (Hines et al 2011). Evaluations of its forecasting performance show that, at the surface level, Polar WRF produces the best prediction of field variables (Wilson et al 2011). Such optimizations in Polar WRF have been included in the standard WRF released by NCAR after version 3.4.1 (stated on the Polar WRF website). The on-going optimizations and most recent version of Polar WRF is available at their website.

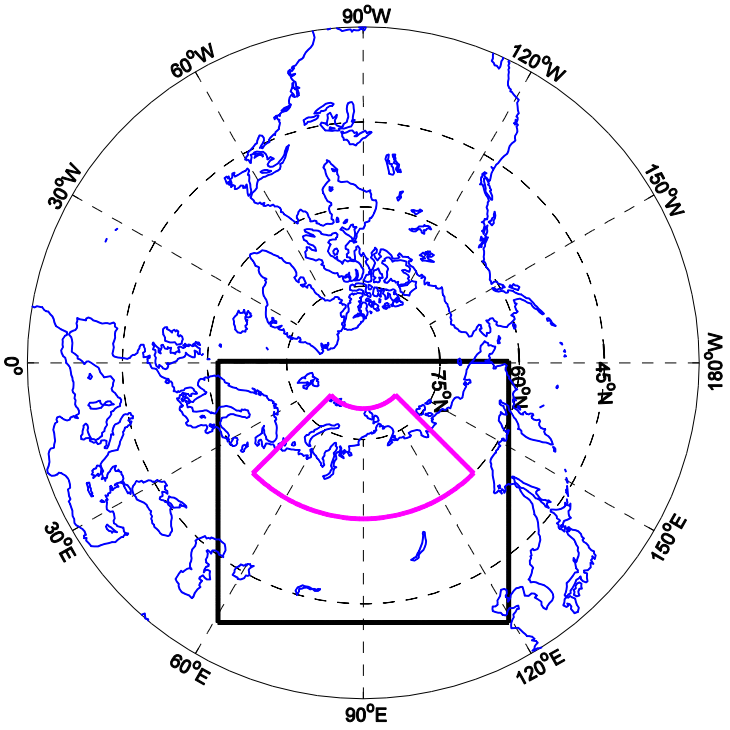

Figure 5.5: Experiment domain in black box. CR region in magenta box.

The CASE2000 experiments presented in this chapter are performed with WRF-ARW version 3.7.1 for a domain of 301 X 271 grid cells using a polar projection. The horizontal resolution is 20 km in both directions. Following the model configurations in Bromwich et al. (2009) and Hines et al. (2011), we use the Morrison two-moment scheme for cloud microphysics, the Rapid Radiative Transfer Model (RRTM) for long wave radiation, and the Goddard scheme for short wave radiation. The Mellor-Yamada-Janjić

(MYJ) scheme is used for the planetary boundary layer and the land surface model employs the Noah-MP scheme with fractional sea ice treatment.

Figure 5.5 outlines the experimental domain in the black box and CR region in the magenta box. The southern domain boundary for the model experiments is extended to about 40°N to allow for local generation of transient eddy activity which is considered to be a vital source in providing enhanced eddy heat flux into CR region during the early stage.

5.3.2 Experiment Design

The model experiments presented in this chapter are aimed at investigating the nonlinear contribution of synoptic-scale eddies during the early stages of CASE2000. ERA-interim data are used as input for the initial and boundary conditions of the model simulations.

Control Experiment

A control experiment (CTRL) is first performed from February 15th to March 11th, that is day -10 to day +15 of CASE2000, to simulate the T2m evolution. The first 5 days of the CTRL simulations are performed with nudging toward the parallel observed state. This nudging is turned off on February 20th (day -5 of CASE2000).

10Dave Experiments

Two different sets of additional experiments are performed to explore the role of the nonlinear contribution of synoptic eddies toward the T2m evolution. In Eq. (7), each meteorological variable is separated into respective climatological-mean and anomaly components. Thus, V' and T' within the nonlinear term term $\left[-\nabla \cdot \overrightarrow{V'T'} - \left(-\nabla \cdot \overrightarrow{\overline{V'T'}}\right)\right]$ in

Eq. (7) represent transient eddy fields. In the first set of experiments, the ERA-interim meteorological variables from ERA-interim (including geopotential heights at all levels, sea level pressure, and surface pressure) are temporally smoothed using a 10-day running mean filter prior to model insertion. The running mean filter effectively removes most of the synoptic time scale eddy activity. Noting our earlier diagnostic results – indicating the role of upstream eddy activity and nonlinear eddy heat transport during the early stages of ASO, we performed three different experiments in which the time-filtered ERAI data are inserted to alter the boundary conditions for the CASE2000 simulation during three different time periods (referred to as the 10Dave experiments).

As for the CTRL experiment, the 10Dave experiments also incorporate nudging the first 5 days (February 15th to 19th) with nudging turned off at February 20th (day -5). The 10Dave_day-5 experiment begins using the smoothed boundary conditions on February 20th (day -5, prior to CASE2000); the 10Dave_day0 experiment follows the CTRL experiment until February 24th (day -1) and begins using the smoothed boundary conditions on February 25th (day 0); the 10Dave_day+5 experiment follows the CTRL experiment until February 29th (day +4) and begins using the smoothed boundary conditions on March 1st (day +5). Comparisons among the three 10Dave experiments and CTRL run provide information on the role of nonlinear synoptic eddy processes during different stages of CASE2000.

<u>COMPOSITE Experiments</u>

In analyzing the composite heat budget, the daily contributions from the nonlinear term $\left[-\nabla\cdot\overrightarrow{V'T'}-\left(-\nabla\cdot\overrightarrow{\overline{V'T'}}\right)\right]$ are first calculated for each individual event and the net

composite contributions is then assessed as $\langle -\nabla \cdot \overrightarrow{V'T'} - \left(-\nabla \cdot \overrightarrow{\overrightarrow{V'T'}}\right)\rangle$, where the angle bracket represents a composite among all ASO events. Similar to a separation of variables into climatological-mean and anomaly components, in assessing the composite nonlinear contribution, field variables can be decomposed into composite-mean and anomalies related to case-to-case variability. That is, $A = \langle A \rangle + A^*$, where the angle bracket represents the daily composite value and the star represents the departure of each individual event from the daily composite value. The calculation of the composite field $\langle A \rangle$ is another effective way to smooth the data, thus leaving the residual quantity, A^*, as an eddy component encompassing synoptic eddies. Using such a formulation, the other set of WRF experiments, the COMPOSITE simulations, employ the composite meteorological variables as initial and boundary conditions for the model to filter out synoptic transient eddy signals from the model input.

Since the average onset dates for the early and late events are separated by about a month, the radiative and boundary forcing will generally be quite different between the early and late events. Thus, only early events are selected for calculating the composite meteorological variables for these experiments. The COMPOSITE experiments begin with nudging on February 10th (day -10), earlier than either the CTRL or the 10Dave experiments, to allow a longer time of model adjustment to the composite fields. To allow for the model run freely with composite boundary conditions, the nudging is shut off on February 20th for COMPOSITE_day-5, on February 21th for COMPOSITE_day-4, on February 22th for COMPOSITE_day-3, on February 23th for COMPOSITE_day-2, on February 24th for COMPOSITE_day-1, and on February 25th for COMPOSITE_day0 simulations, respectively.

5.3.3 Results of CASE2000 Simulations with WRF

Composite heat budget analysis indicates that the dominant process leading into the rapid warming during spring onset is nonlinear heat transport due to synoptic eddies. By reducing the amount of synoptic-scale wave activity in the boundary condition, we expect the T2m evolution during the early stages in the 10Dave experiments to be altered compared with the CTRL experiment. Figure 5.6 provides the time evolution in the areal-average T2m from ERA-interim (observed event), the CTRL experiment, and the three 10Dave experiments employing smoothed boundary conditions beginning at day -5 (February 20th), day 0 (February 25th), and day +5 (March 1st) relative to observed onset (February 25th, noted by the blue star on the local minimum value in the 30-day low-pass filtered T2m from ERA-interim). We first note that the low-pass time series includes a slight forward shift in the minimum T2m compared with the unfiltered time series (black line). The unfiltered (and observed) T2m falls to its minimum at February 26th and then maintains this value for 3 days before the rapid warming process begins. All of the model simulations well represent the minimum T2m feature at February 26th, but the subsequent "flatness" in the T2m profile is not well simulated in either the CTRL run or any of the10Dave experiments. Instead, the simulation results demonstrate an immediate increase after the minimum T2m.

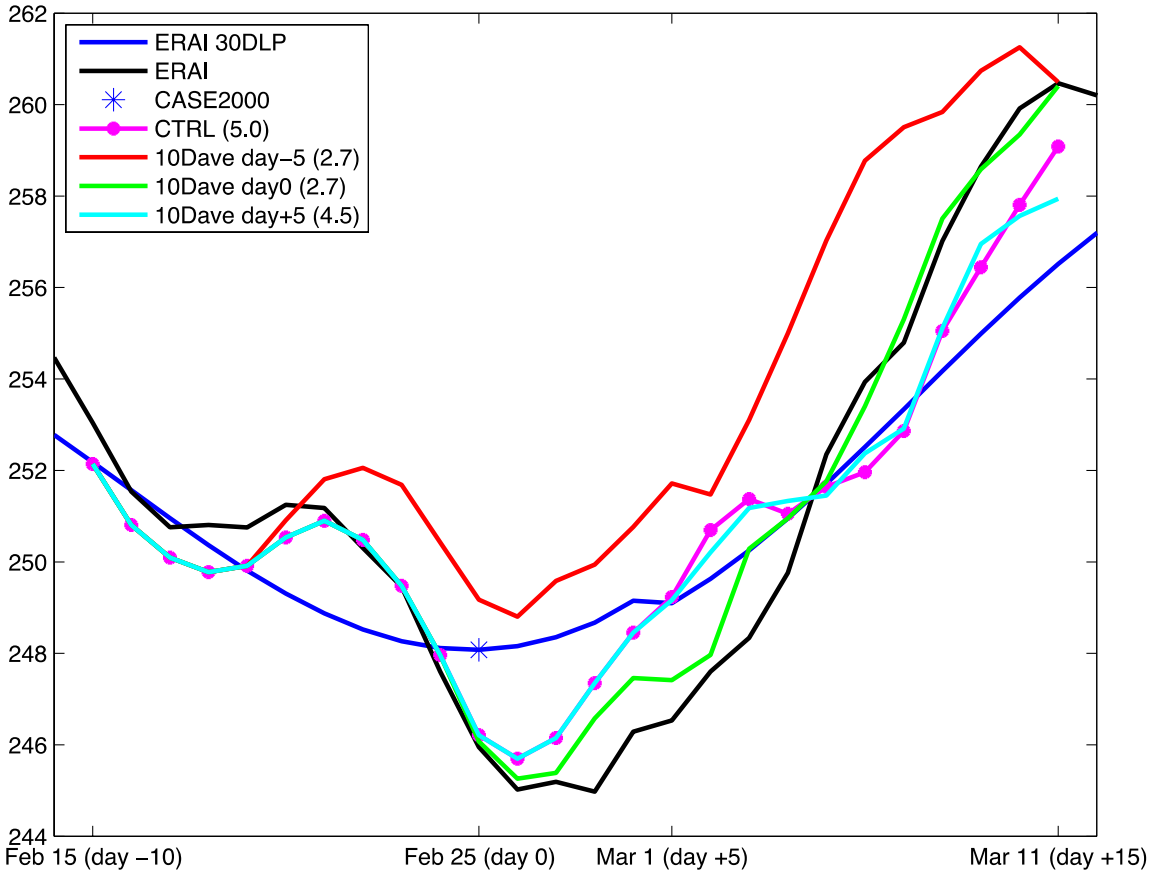

Figure 5.6: Time evolutions of daily T2m (unit: K) averaged over CR region. Unfiltered T2m from ERA-interim in black; 30-day low-pass filtered T2m from ERA-interim in blue; CTRL simulated T2m in magenta with star; 10Dave_day-5 simulated T2m in red; 10Dave_day0 simulated T2m in green; 10Dave_day+5 simulated T2m in light blue.

In the CTRL experiment, T2m increases by 5K between February 26th and March 2nd (5 days after the T2m minimum). For the same time period, the 10Dave_day-5 and 10Dave_day0 model experiments both exhibit a weaker T2m increase of 2.7K, about half of the T2m increase found in the CTRL experiment. The two 10Dave experiments also include quite different T2m variability versus the CTRL. The 10Dave_day+5 experiment, on the other hand, exhibits a T2m evolution very similar to CTRL. These experimental results are consistent with the heat budget diagnostics suggesting that, prior to and during the early stages of ASO events, synoptic eddies provide the dominant contribution toward rapid warming. During the middle event stage by which time the large-scale circulation has been modified favorable to induce linear advective warming, the contribution from the nonlinear term diminishes. Thus, the insertion of the smoothed boundary conditions at a later time does not significantly alter the existing circulation, thus not altering much of the warming process afterwards.

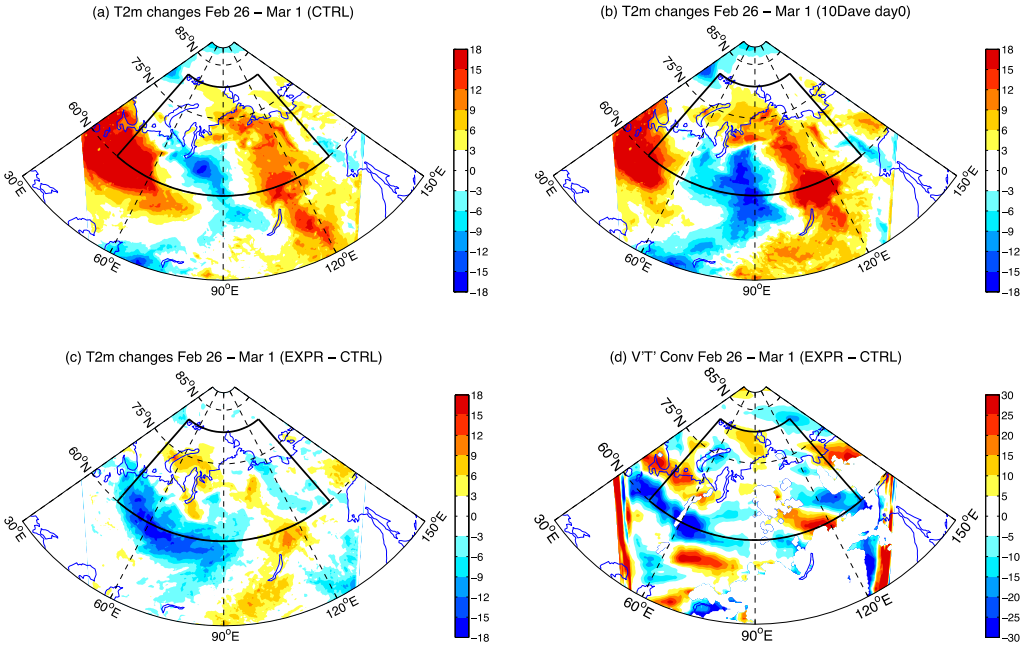

Figure 5.7: (a) T2m changes from February 26th to March 1st in CTRL simulation. (b) T2m changes from February 26th to March 1st in 10Dave_day0 simulation. (c) Differences of T2m changes from February 26th to March 1st between CTRL and 10Dave_day0 simulations. (d) Differences in eddy heat flux convergence from February 26th to March 1st between CTRL and 10Dave_day0 simulations.

A comparison between the CTRL and the 10Dave_day0 simulations of the patterns of 5-day T2m changes is provided in Fig. 5.7. A systematic T2m increase is observed over the northern and southeast portions of CR region while the southern edge is covered with T2m increase around 60E and decrease around 90E. By taking the differences between the CTRL and 10Dave_day0 experiments (Fig. 5.7c), we notice that the southwest corner of the CR region is dominated by a large area of negative values, implying a *weakened* T2m

increase within this region when synoptic eddy activity is removed in the boundary condition. The local convergence of synoptic eddy (2.5-6-day band-pass) heat flux is also calculated for the CTRL and 10Dave_day0 experiments, respectively, and the difference between the two is shown in Fig. 5.7d. A robust *weakening* of the heat convergence is observed over the southwest corner of the CR region for the 10Dave_day0 experiment, largely contributing a *reduction* in the T2m increase. This area of reduced T2m increase corresponds very well with the primary region of nonlinear heat flux convergence during the early stages of composite heat budget analysis (Fig. 4.4g).

Figure 8 displays an analogous comparison of the T2m time series among ERA-interim, the CASE2000 CTRL simulation, and the COMPOSITE model experiments. The composite T2m evolutions of CR early events demonstrate a relatively weaker increasing rate compared with the single CASE2000 event likely in association with the removal of case-to-case variability. The COMPOSITE experiments with different initial dates can be viewed together as an ensemble of simulations that effectively test the contribution of the nonlinear synoptic eddy transports associated with case-to-case variability. The ensemble mean T2m evolution reveals a much weaker and more gradual T2m increase. The onset date for the ensemble mean is effectively delayed by about one week compared to either the CTRL run or the ERAI composite. Even by day +20, the ensemble mean T2m increase of the COMPOSITE experiments is only about half that of the CTRL run. The T2m behavior of the COMPOSITE experiments indicates that the transient eddy activity plays a vital role in determining the onset date and CR warming behavior in 2 week period (time scale of ASO events discussed in Chapter 3) surrounding ASO.

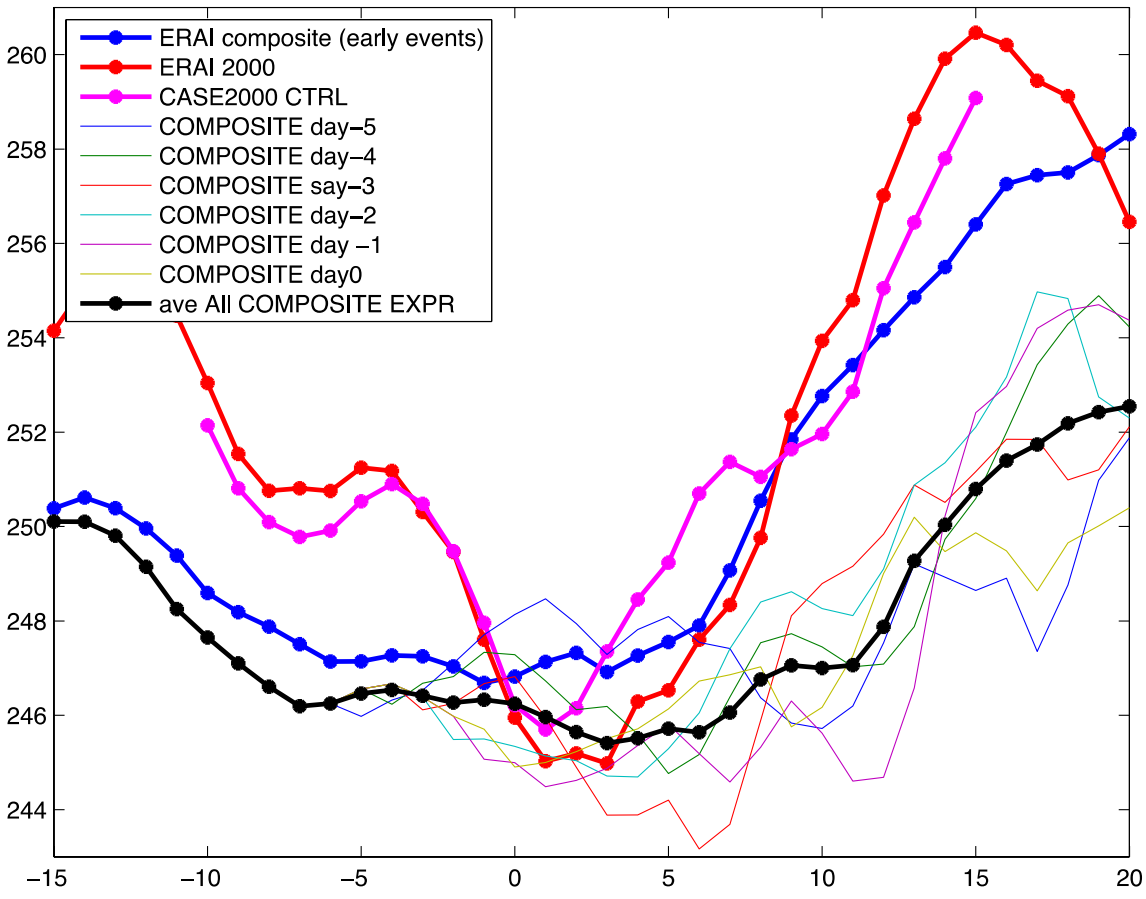

Figure 5.8: Time evolutions of daily T2m. Composite of early CR events from ERA-interim in blue line with stars; T2m in 2000 from ERA-interim in red line with stars; simulated T2m from CTRL run in magenta line with stars; ensemble mean of COMPOSITE simulations in black line with stars.

5.4 Summary

In this chapter, the 2000 CR event (CASE2000; onset date of February 25th) is used to pursue a detailed case study, including parallel model experiments. Although the CASE2000 T2m evolution exhibits a more rapid surface warming signal than found in the composite results (black lines in Fig. 5.3 and Fig. 4.8a), an analysis of ERA-interim data shows that CASE2000 event includes the primary characteristic signatures found in the earlier ASO composite analysis. A robust warming pattern is observed in the critical region in both surface (T2m) and 925 hPa (T925) air temperature. This dramatic increase in temperature is first initiated by nonlinear heat transport (due to synoptic eddy activity) and then continued by linear advection (associated with large-scale circulation anomalies). Enhanced baroclinic eddy activity is observed over the southwest CR region during early stages, which is related to the initially dominant nonlinear warming. A dipole anomaly in the SLP emerges during the middle stage to provide a pathway for coherent linear warm advection via the anomalous large-scale circulation pattern.

In order to examine the impact of the nonlinear term (transient eddy) in initiating the CASE2000 CR event, experiments with the Weather Research and Forecasting Model are performed over a domain encompassing the CR region and extending southward. A control (CTRL) run is first designed by directly using ERA-interim data for initial and boundary conditions from day -5 to day +15 of CASE2000 to simulate the time evolution of meteorological variables during CASE2000. Two sets of additional experiments are conducted to isolate the synoptic eddy activity contribution to the CTRL simulation. By filtering out synoptic-scale disturbances from the domain boundary, the strength of the T2m increase during the early stage of CASE2000 is effectively reduced by half. Using

composite meteorological fields to provide initial and boundary conditions, the onset date is delayed by roughly a week, the approximate amount of time required for synoptic eddy activity to be locally generated within the model circulation. The T2m increase within the following 2 weeks is also reduced by about 1/3 compared to the CTRL run. Our model experiment results largely affirm the critical role of nonlinear dynamical processes (due to synoptic eddies) in determining the timing and magnitude of the rapid ASO warming.

CHAPTER 6: CONCLUSTIONS AND IMPLICATIONS

6.1 Summary and Conclusions

In this dissertation, we explore rapid springtime seasonal transition in the Arctic atmospheric system, which includes the sudden break down of polar vortex at the upper tropospheric and stratospheric levels and a rapid temperature increase at the surface level. Existing studies have studied the transition in the upper atmosphere, that is, stratospheric final warming events (SFW). A set of comprehensive investigations revealed a dynamical linkage between SFW events and a) upward propagating stationary wave activity and b) large-scale modes of variability (e.g., Black and McDaniel 2007; Waugh and Rong 2002). However, our knowledge of the rapid springtime warming occurring at the surface is quite limited. Therefore, the primary goal of the current research is to investigate the phenomenological characteristics of, and physical mechanisms responsible for, the rapid surface temperature increase observed to occur during Arctic spring onset.

Three methods are tested to optimally isolate Arctic spring onset (ASO) events in terms of the surface air temperature evolution. A 2-phase linear regression model is first used to identify a transition from an approximately steady winter state to the warming spring state. The two other methods, the time derivative (d2T/dT) and radius of curvature (RoC) methods, identify periods of large T2m acceleration. Although all three methods are largely successful in isolating the state transition associated with ASO, the RoC method is most effective in capturing the most rapid temperature increases and is thus adopted in the study. Statistical analyses indicate a bimodal distribution of ASO timing, with strong interannual variability but no significant long-term trend. This bi-modal distribution of ASO timing is observed in the statistics of onset dates derived via all three methods, and

thus is not attributed to being an implicit byproduct of the methods themselves. A detailed study of ASO synoptic behavior of is performed separately for early and late event groups, but does not reveal any notable distinction between the two groups. As discussed in Chapter 2, the bi-modal distribution is related to a two-stage transition in the climatological annual cycle of T2m, which may be related to prior atmospheric conditions such as temporal variability in synoptic eddy activity. The composite time evolution of daily T2m averaged over the Arctic during ASO events exhibits a faster rate of increase than a) the parallel T2m increase observed in association with the climatological seasonal cycle and b) the rate of T2m decrease during the fall seasonal transition. The more gradually-decreasing transition of fall suggests a more focused fall onset timing with little interannual variability, thus leading to weak T2m anomalies during the events. Along with the above-noted interannual variability in ASO timing, this result suggests that ASO events are likely dynamically driven while the fall onset is more likely dominated by radiative forcing.

We next examine the spatial structure of the T2m increase during ASO and the associated synoptic conditions. Composite maps of T2m changes during ASO uncover a critical region over Northern Siberia as a common warming region for most ASO events. Several sub-categories of ASO events are identified, in which distinct warming signatures are also observed over the Greenland-North American sector, East Asia, and Alaska, respectively. Parallel composite analyses of sea level pressure reveal the typical synoptic structures, which provide favorable conditions for rapid regional advective and diabatic warming for ASO events.

To isolate various physical processes that contribute to T2m increase during ASO events, composite heat budgets of ASO events are performed. Using the RoC method,

regional ASO events are first identified within four high latitude sectors: The primary (critical) region over North Siberia (CR), Greenland-North America (G-NA), East Asia (EA), and Alaska (AL). To identify the primary forcing of the rapid temperature increases observed during the regional ASO events, for each event category contributions to the tendency of near-surface air temperature anomaly are assessed via application of the thermodynamic equation. For each region, anomalous eddy heat flux convergence is found to be the main contributor to regional warming prior to and during the early stage of ASO (through day +5). Thereafter, horizontal advection of climatological-mean temperature by the large-scale circulation anomaly emerges as the leading contributor to regional warming during the later stages of events. A parallel diagnosis of storm track strength using the envelope function reveals a systematic weakening of eddy activity within each region, leading to a reduction in the northward eddy heat flux out of the domain and an accumulation of heat within the region. For CR, G-NA, and EA events, a dipole anomaly of sea level pressure in the longitudinal direction, with lower (higher) pressure to the west (east), generates an anomalous southerly flow linked to late period linear warm advection. The heat budget results indicate that anomalous dynamical processes related to synoptic eddy activity and stationary wave patterns are the primary contributors to rapid temperature increase during ASO events, with minimal contributions from anomalous diabatic processes.

The fundamental characteristics and dynamical mechanisms of rapid temperature increase during ASO events were revealed from the composite analysis of many events. The CR event in 2000 (CASE2000) is next selected to performed a detailed case study both in terms of observational data and model simulations. During CASE2000, a robust T2m

increase is observed within the 2-week period after onset. A heat budget diagnosis shows dynamical evolution very similar to our earlier composite study: The rapid T2m increase is initiated by an anomalous eddy heat flux convergence due to enhanced synoptic eddy on the southern boundary and suppressed synoptic eddy within the majority of CR region. The warming process is then continued via a large-scale circulation anomaly pattern consisting of an SLP anomaly dipole and anomalous northeasterly flow with warm advection. Experiments with the Weather Research and Forecasting (WRF) Model are then performed over a region encompassing the CR and its southern vicinity. By filtering out synoptic eddy activity from the model domain via the use of a) boundary conditions based upon 10-day running mean and b) composite meteorological variables as input for initial and boundary conditions, the timing of CASE2000 is effectively delayed and the magnitude of the associated T2m increase during CASE2000 event is largely reduced. These experiments provide further support to our proposed mechanism for the rapid near-surface warming during ASO events. The role of synoptic eddy anomalies in initiating ASO events also provides insight into the potential prediction of ASO events, which may be limited by our ability to predict individual synoptic-scale disturbances. For future research, it will be of great interest to more commonly search for organized patterns of anomalous eddy activity such as those observed during the initial stages of ASO. It is also important to further investigate the dynamical mechanisms responsible for the observed sequence of anomalous synoptic eddy activity leading into the formation of large-scale SLP anomaly dipoles during the later stages.

6.2 Implications on Broader Scopes of Arctic Investigations

The Arctic is currently undergoing a prominent long-term warming in wintertime surface air temperature (e.g., Serreze et al. 2009) along with a dramatic decrease in the summertime sea ice (e.g., Deser et al. 2010 and Screen et al. 2013). Thus, the Arctic is getting warmer and wetter (Boisvert and Stroeve 2015). Investigations of the atmospheric response to sea ice variability have shown a mutual interaction between sea ice extent and Arctic cyclones (e.g., Parkinson and Comiso 2013; Simmonds and Rudeva 2012; Zhang et al. 2004). Studies of the interference between synoptic eddies and stationary waves (Goss et al. 2016) suggest that enhanced meridional flow by the amplified stationary and synoptic waves transports heat and moisture into the Arctic resulting in increased surface air temperature and reduced sea ice concentration in the Barents and Kara Seas. Seierstad and Bader (2009) analyzed the atmospheric response to sea ice loss and concluded that declining sea ice cover results in fewer winter storms during March. Screen et al. (2011) show that a reduction in cyclones tracking from northern Eurasia and surrounding seas to the Arctic during late spring results in a loss of perennial sea ice leading to thinner Arctic sea ice. The loss of sea ice can effectively change the baroclinicity over central Arctic latitudes (Simmonds and Rudeva 2012), consequently providing an increased energy source for localized cyclone systems over the Arctic (Simmonds and Keay 2009; Zhang et al. 2013). Although we did not find any direct relationship between spring onset timing or strength with sea ice extent, the nonlinear dynamical contribution to ASO observed for the early stages of spring onset events suggests a potential role for anomalous synoptic cyclone activity. The eddy heat flux convergence into the warming domain is consistent with enhanced synoptic eddy activity on the southern edge along with reduced eddy activity to

the north of the domain. This latter signature reduces the meridional eddy heat flux into the central Arctic, potentially pre-conditioning the sea ice extent during summer.

Although the current analysis of spring onset focuses on high-latitudes, there is also evidence of a broader hemispheric influence. By analyzing changes in the sea level pressure field before and after Arctic spring onset, a connection between regional spring onset and the seasonal evolution of semi-permanent pressure systems over mid- to high-latitudes, including a connection to stationary waves, is revealed. During high-latitude spring onset events, the springtime march of surface air temperature at mid-latitudes is slightly reduced. This latitudinal seesaw structure in the tendency of air temperature anomalies indicates that high-latitude spring onset is most likely accompanied by mid-latitude cold events. In studying the meridional circulation (the equatorward lower branch and poleward upper branch), Iwasaki et al. (2014) and Yu et al. (2015a; 2015b) found a connection between a stronger meridional circulation and mid-latitude cold air outbreak events. Such a strengthening is reflected at early stages in high-latitude spring onset when systematic northerly anomalies are observed over the CR and G-NA regions, where the two main streams of the meridional circulation occur. By analyzing the zonal mean E-P flux, Iwasaki and Mochizuki (2012) show that the meridional circulation is wave-induced and its variability is greatly influenced by ultra-long stationary waves. Given the current results on the physical sources of rapid temperature increase, it is of future interest to investigate in further detail the behavior and contribution of synoptic and stationary wave activity during high-latitude spring onset events.

Contents in Chapter 2 and Chapter 3 are published in Journal of Climate (He and Black 2015).

The heat budget analysis in Chapter 4 has been accepted to Journal of Geophysical Research: Atmosphere.

The case study in Chapter 5 is prepared for a manuscript for journal submission.

REFERENCES

Aasa, A., J. Jaagus, R. Ahas, and M. Sepp, 2004: The influence of atmospheric circulation on plant phenological phases in central and eastern Europe. *Int J Climatol*, **24,** 1551-1564.

Ambaum, M. H., B. J. Hoskins, and D. B. Stephenson, 2001: Arctic oscillation or North Atlantic oscillation? *J Climate*, **14,** 3495-3507.

Andrews, D. G., J. R. Holton, and C. B. Leovy, 1987: *Middle atmosphere dynamics.* Academic Press, xi, 489 p. pp.

Baldwin, M. P., and T. J. Dunkerton, 1999: Propagation of the Arctic Oscillation from the stratosphere to the troposphere. *Journal of Geophysical Research: Atmospheres*, **104,** 30937-30946.

Black, R. X., and B. A. Mcdaniel, 2007: The dynamics of northern hemisphere stratospheric final warming events. *J Atmos Sci*, **64,** 2932-2946.

Black, R. X., B. A. McDaniel, and W. A. Robinson, 2006: Stratosphere-troposphere coupling during spring onset. *J Climate*, **19,** 4891-4901.

Black, R. X., B. McDaniel, and Y.-Y. Lee, 2012: The structure, dynamics and tropospheric signature of the Polar Annular Mode. *Journal of Geophysical Research: Atmospheres*, **117,** n/a-n/a.

Bodurtha, F. T., 1952: An Investigation of Anticyclogenesis in Alaska. *J Meteorol*, **9,** 118-125.

Boisvert, L., and J. Stroeve, 2015: The Arctic is becoming warmer and wetter as revealed by the Atmospheric Infrared Sounder. *Geophys Res Lett*, **42,** 4439-4446.

Bromwich, D. H., K. M. Hines, and L. S. Bai, 2009: Development and testing of polar weather research and forecasting model: 2. Arctic Ocean. *Journal of Geophysical Research: Atmospheres*, **114**.

Cheng, X. H., and J. M. Wallace, 1993: Cluster-Analysis of the Northern-Hemisphere Wintertime 500-Hpa Height Field - Spatial Patterns. *J Atmos Sci*, **50,** 2674-2696.

Cook, B. I., and B. M. Buckley, 2009: Objective determination of monsoon season onset, withdrawal, and length. *J Geophys Res-Atmos*, **114**.

Corti, S., F. Molteni, and T. Palmer, 1999: Signature of recent climate change in frequencies of natural atmospheric circulation regimes. *Nature*, **398,** 799-802.

D'Odorico, P., J. Yoo, and S. Jaeger, 2002: Changing seasons: An effect of the North Atlantic Oscillation? *J Climate*, **15,** 435-445.

Davis, P. A., 1963: An analysis of the atmospheric heat budget. *J Atmos Sci*, **20,** 5-22.

Dee, D. P., and Coauthors, 2011: The ERA-Interim reanalysis: configuration and performance of the data assimilation system. *Q J Roy Meteor Soc*, **137,** 553-597.

Deser, C., and H. Teng, 2008: Evolution of Arctic sea ice concentration trends and the role of atmospheric circulation forcing, 1979–2007. *Geophys Res Lett*, **35**.

Deser, C., J. E. Walsh, and M. S. Timlin, 2000: Arctic sea ice variability in the context of recent atmospheric circulation trends. *J Climate*, **13,** 617-633.

Deser, C., R. A. Tomas, and S. Peng, 2007: The transient atmospheric circulation response to North Atlantic SST and sea ice anomalies. *J Climate*, **20,** 4751-4767.

Deser, C., R. Tomas, M. Alexander, and D. Lawrence, 2010: The seasonal atmospheric response to projected Arctic sea ice loss in the late twenty-first century. *J Climate*, **23,** 333-351.

Ding, Y., and T. N. Krishnamurti, 1987: Heat-Budget of the Siberian High and the Winter Monsoon. *Mon Weather Rev*, **115,** 2428-2449.

Ding, Y. H., 1990: Buildup, Air-Mass Transformation and Propagation of Siberian High and Its Relations to Cold Surge in East-Asia. *Meteorol Atmos Phys*, **44,** 281-292.

Dole, R. M., and R. X. Black, 1990: Life Cycles of Persistent Anomalies. Part II: The Development of Persistent Negative Height Anomalies over the North Pacific Ocean. *Mon Weather Rev*, **118,** 824-846.

Frey, K. E., and L. C. Smith, 2003: Recent temperature and precipitation increases in West Siberia and their association with the Arctic Oscillation. *Polar Research*, **22,** 287-300.

Gerdes, R., 2006: Atmospheric response to changes in Arctic sea ice thickness. *Geophys Res Lett*, **33**.

Gong, D. Y., and C. H. Ho, 2002: The Siberian High and climate change over middle to high latitude Asia. *Theor Appl Climatol*, **72,** 1-9.

Gong, D. Y., and C. H. Ho, 2003: Arctic oscillation signals in the East Asian summer monsoon. *Journal of Geophysical Research: Atmospheres*, **108**.

Gong, D. Y., and C. H. Ho, 2004: Intra-seasonal variability of wintertime temperature over East Asia. *Int J Climatol*, **24,** 131-144.

Gong, D. Y., S. W. Wang, and J. H. Zhu, 2001: East Asian winter monsoon and Arctic oscillation. *Geophys Res Lett*, **28,** 2073-2076.

Goss, M., S. B. Feldstein, and S. Lee, 2016: Stationary Wave Interference and Its Relation to Tropical Convection and Arctic Warming. *J Climate*, **29,** 1369-1389.

Handorf, D., R. Jaiser, K. Dethloff, A. Rinke, and J. Cohen, 2015: Impacts of Arctic sea ice and continental snow cover changes on atmospheric winter teleconnections. *Geophys Res Lett*, **42,** 2367-2377.

Hartmann, D. L., 1994: *Global physical climatology.* Academic Press, x, 411 p. pp.

He, J., and R. X. Black, 2015: Characterizing Arctic Spring Onset. *J Climate*, **28,** 4471-4489.

Helsel, D. R., and R. M. Hirsch, 1992: *Statistical methods in water resources.* Elsevier, xvi, 522 p. pp.

Hines, K. M., and D. H. Bromwich, 2008: Development and testing of polar weather research and forecasting (WRF) model. Part I: Greenland ice sheet meteorology*. *Mon Weather Rev*, **136,** 1971-1989.

Hines, K. M., D. H. Bromwich, L.-S. Bai, M. Barlage, and A. G. Slater, 2011: Development and testing of polar WRF. Part III: Arctic Land*. *J Climate*, **24,** 26-48.

Iwasaki, T., and Y. Mochizuki, 2012: Mass-weighted isentropic zonal mean equatorward flow in the Northern Hemispheric winter. *Sola*, **8,** 115-118.

Iwasaki, T., T. Shoji, Y. Kanno, M. Sawada, M. Ujiie, and K. Takaya, 2014: Isentropic analysis of polar cold airmass streams in the Northern Hemispheric winter. *J Atmos Sci*, **71,** 2230-2243.

Jakobson, E., T. Vihma, T. Palo, L. Jakobson, H. Keernik, and J. Jaagus, 2012: Validation of atmospheric reanalyses over the central Arctic Ocean. *Geophys Res Lett*, **39**.

Lau, N.-C., 1979: The observed structure of tropospheric stationary waves and the local balances of vorticity and heat. *J Atmos Sci*, **36,** 996-1016.

Lee, Y.-Y., and G.-H. Lim, 2012: Dependency of the North Pacific winter storm tracks on the zonal distribution of MJO convection. *Journal of Geophysical Research: Atmospheres*, **117,** n/a-n/a.

Lee, Y.-Y., and R. X. Black, 2015: The Structure and Dynamics of the Stratospheric Northern Annular Mode in CMIP5 Simulations. *J Climate*, **28,** 86-107.

Linderholm, H. W., 2006: Growing season changes in the last century. *Agr Forest Meteorol*, **137,** 1-14.

Liu, X. H., and R. Q. Ding, 2007: The relationship between the Spring Asian Atmospheric circulation and the previous winter Northern Hemisphere annular mode. *Theor Appl Climatol*, **88,** 71-81.

Lohmann, G., and K. H. Wiltshire, 2012: Winter atmospheric circulation signature for the timing of the spring bloom of diatoms in the North Sea. *Mar Biol*, **159,** 2573-2581.

Lund, R., and J. Reeves, 2002: Detection of undocumented changepoints: A revision of the two-phase regression model. *J Climate*, **15,** 2547-2554.

Martin, S., and E. A. Munoz, 1997: Properties of the arctic 2-meter air temperature field for 1979 to the present derived from a new gridded dataset. *J Climate*, **10,** 1428-1440.

Nakamura, H., and J. M. Wallace, 1990: Observed Changes in Baroclinic Wave Activity during the Life-Cycles of Low-Frequency Circulation Anomalies. *J Atmos Sci*, **47,** 1100-1116.

O'Reilly, C. H., and A. Czaja, 2015: The response of the Pacific storm track and atmospheric circulation to Kuroshio Extension variability. *Q J Roy Meteor Soc*, **141,** 52-66.

Overland, J. E., M. C. Spillane, D. B. Percival, M. Wang, and H. O. Mofjeld, 2004: Seasonal and regional variation of pan-arctic surface air temperature over the instrumental record*. *J Climate*, **17,** 3263-3282.

Palus, M., D. Novotna, and P. Tichavsky, 2005: Shifts of seasons at the European mid-latitudes: Natural fluctuations correlated with the North Atlantic Oscillation. *Geophys Res Lett*, **32**.

Parkinson, C. L., and J. C. Comiso, 2013: On the 2012 record low Arctic sea ice cover: Combined impact of preconditioning and an August storm. *Geophys Res Lett*, **40,** 1356-1361.

Qian, C., C. B. Fu, Z. H. Wu, and Z. W. Yan, 2009: On the secular change of spring onset at Stockholm. *Geophys Res Lett*, **36**.

Qian, C., Z. Wu, C. Fu, and D. Wang, 2011a: On changing El Niño: A view from time-varying annual cycle, interannual variability, and mean state. *J Climate*, **24,** 6486-6500.

Qian, C., C. B. Fu, Z. H. Wu, and Z. W. Yan, 2011b: The Role of Changes in the Annual Cycle in Earlier Onset of Climatic Spring in Northern China. *Adv Atmos Sci*, **28,** 284-296.

Rienecker, M. M., and Coauthors, 2011: MERRA: NASA's Modern-Era Retrospective Analysis for Research and Applications. *J Climate*, **24,** 3624-3648.

Rigor, I. G., R. L. Colony, and S. Martin, 2000: Variations in surface air temperature observations in the Arctic, 1979-97. *J Climate*, **13,** 896-914.

Rigor, I. G., J. M. Wallace, and R. L. Colony, 2002: Response of sea ice to the Arctic Oscillation. *J Climate*, **15,** 2648-2663.

Schwartz, M. D., and T. M. Crawford, 2001: Detecting energy-balance modifications at the onset of spring. *Physical Geography*, **22,** 394-409.

Schwartz, M. D., R. Ahas, and A. Aasa, 2006: Onset of spring starting earlier across the Northern Hemisphere. *Global Change Biol*, **12,** 343-351.

Screen, J. A., and I. Simmonds, 2010: The central role of diminishing sea ice in recent Arctic temperature amplification. *Nature*, **464,** 1334-1337.

Screen, J. A., I. Simmonds, and K. Keay, 2011: Dramatic interannual changes of perennial Arctic sea ice linked to abnormal summer storm activity. *Journal of Geophysical Research: Atmospheres*, **116,** n/a-n/a.

Screen, J. A., I. Simmonds, C. Deser, and R. Tomas, 2013: The atmospheric response to three decades of observed Arctic sea ice loss. *J Climate*, **26,** 1230-1248.

Seierstad, I. A., and J. Bader, 2009: Impact of a projected future Arctic sea ice reduction on extratropical storminess and the NAO. *Clim Dynam*, **33,** 937-943.

Serreze, M., A. Barrett, J. Stroeve, D. Kindig, and M. Holland, 2009: The emergence of surface-based Arctic amplification. *The Cryosphere*, **3,** 11-19.

Serreze, M., and Coauthors, 2003: A record minimum arctic sea ice extent and area in 2002. *Geophys Res Lett*, **30**.

Serreze, M. C., and J. A. Francis, 2006: The Arctic amplification debate. *Climatic change*, **76,** 241-264.

Serreze, M. C., and R. G. Barry, 2014: *The Arctic climate system.* Cambridge University Press.

Serreze, M. C., M. M. Holland, and J. Stroeve, 2007: Perspectives on the Arctic's shrinking sea-ice cover. *Science*, **315,** 1533-1536.

Simmonds, I., and K. Keay, 2009: Extraordinary September Arctic sea ice reductions and their relationships with storm behavior over 1979–2008. *Geophys Res Lett*, **36**.

Simmonds, I., and I. Rudeva, 2012: The great Arctic cyclone of August 2012. *Geophys Res Lett*, **39**.

Simmons, A. J., and P. Poli, 2015: Arctic warming in ERA‐Interim and other analyses. *Q J Roy Meteor Soc*, **141,** 1147-1162.

Singarayer, J. S., J. L. Bamber, and P. J. Valdes, 2006: Twenty-first-century climate impacts from a declining Arctic sea ice cover. *J Climate*, **19,** 1109-1125.

Sparks, T. H., and A. Menzel, 2002: Observed changes in seasons: An overview. *Int J Climatol*, **22,** 1715-1725.

Stine, A. R., and P. Huybers, 2012: Changes in the Seasonal Cycle of Temperature and Atmospheric Circulation. *J Climate*, **25,** 7362-7380.

Stroeve, J., M. M. Holland, W. Meier, T. Scambos, and M. Serreze, 2007: Arctic sea ice decline: Faster than forecast. *Geophys Res Lett*, **34**.

Takaya, K., and H. Nakamura, 2005: Mechanisms of intraseasonal amplification of the cold Siberian high. *J Atmos Sci*, **62,** 4423-4440.

Thompson, D. W., and J. M. Wallace, 1998: The Arctic Oscillation signature in the wintertime geopotential height and temperature fields. *Geophys Res Lett*, **25,** 1297-1300.

Thomson, D. J., 1995: The Seasons, Global Temperature, and Precession. *Science*, **268,** 59-68.

Trenberth, K. E., and J. M. Caron, 2001: Estimates of meridional atmosphere and ocean heat transports. *J Climate*, **14,** 3433-3443.

Wallace, J. M., 2000: North Atlantic oscillatiodannular mode: two paradigms—one phenomenon. *Q J Roy Meteor Soc*, **126,** 791-805.

Walther, A., and H. W. Linderholm, 2006: A comparison of growing season indices for the Greater Baltic Area. *International Journal of Biometeorology*, **51,** 107-118.

Wang, J., and Coauthors, 2009: Is the Dipole Anomaly a major driver to record lows in Arctic summer sea ice extent? *Geophys Res Lett*, **36**.

Ward, J. H., 1963: Hierarchical Grouping to Optimize an Objective Function. *J Am Stat Assoc*, **58,** 236-&.

Watanabe, E., J. Wang, A. Sumi, and H. Hasumi, 2006: Arctic dipole anomaly and its contribution to sea ice export from the Arctic Ocean in the 20th century. *Geophys Res Lett*, **33**.

Waugh, D. W., and P.-p. Rong, 2002: Interannual variability in the decay of lower stratospheric Arctic vortices. *気象集誌. 第2 輯*, **80,** 997-1012.

White, M. A., P. E. Thornton, and S. W. Running, 1997: A continental phenology model for monitoring vegetation responses to interannual climatic variability. *Global Biogeochem Cy*, **11,** 217-234.

Wilks, D. S., 2011: *Statistical methods in the atmospheric sciences.* 3rd ed. Elsevier/Academic Press, xix, 676 p. pp.

Wilson, A. B., D. H. Bromwich, and K. M. Hines, 2011: Evaluation of Polar WRF forecasts on the Arctic System Reanalysis domain: Surface and upper air analysis. *Journal of Geophysical Research: Atmospheres*, **116**.

Wiltshire, K. H., and B. F. J. Manly, 2004: The warming trend at Helgoland Roads, North Sea: Phytoplankton response. *Helgoland Mar Res*, **58,** 269-273.

Wiltshire, K. H., and Coauthors, 2008: Resilience of North Sea phytoplankton spring bloom dynamics: An analysis of long-term data at Helgoland Roads. *Limnol Oceanogr*, **53,** 1294-1302.

Wu, B., J. Wang, and J. E. Walsh, 2006: Dipole anomaly in the winter Arctic atmosphere and its association with sea ice motion. *J Climate*, **19,** 210-225.

Yu, Y., R. Ren, and M. Cai, 2015a: Dynamical Linkage between Cold Air Outbreaks and Intensity Variations of the Meridional Mass Circulation. *J Atmos Sci*.

Yu, Y., M. Cai, R. Ren, and H. M. Van Den Dool, 2015b: Relationship between warm airmass transport into the upper polar atmosphere and cold air outbreaks in winter. *J Atmos Sci*, **72,** 349-368.

Zhang, J., R. Lindsay, A. Schweiger, and M. Steele, 2013: The impact of an intense summer cyclone on 2012 Arctic sea ice retreat. *Geophys Res Lett*, **40,** 720-726.

Zhang, X., J. E. Walsh, J. Zhang, U. S. Bhatt, and M. Ikeda, 2004: Climatology and interannual variability of Arctic cyclone activity: 1948-2002. *J Climate*, **17,** 2300-2317.

Zhang, X., A. Sorteberg, J. Zhang, R. Gerdes, and J. C. Comiso, 2008: Recent radical shifts of atmospheric circulations and rapid changes in Arctic climate system. *Geophys Res Lett*, **35**.